الجمهورية الجزائرية الديموقراطية الشعبية

République Algérienne Démocratique et Populaire

وزارة التعليم العالي والبحث العلمي

Ministère de l'Enseignement Supérieur et de la Recherche Scientifique

Université des Frères MENTOURI CONSTANTINE 1

جامعــــــة الإخــوة منــــتــــوري قسنطينـــــــة 1

Faculté des Sciences de la Technologie

كليـــة علــــوم التـكنـولـوجيـا

Département d'Electronique

قسم الإلكتـــرونيـــك

Ordre N° : ....

Series : ......

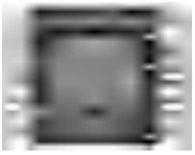

Thèse

Présentée en vue de l'obtention du
Diplôme de Doctorat 3^{éme} Cycle

Option **: Electronique**

Présentée par **: Faiza Bounaas**

Spécialité : **Micro- Nanoélectronique et photonique**

Thème

Contribution à la modélisation des microstructures à cristaux photoniques à base des matériaux semi-conducteurs et composites

Soutenu le : 20/12/2023

Devant le jury :

Président :	Fouad KERROUR	Prof. Université Frères Mentouri Constantine1.
Directeur de thèse :	Amel LABBANI	Prof. Université Frères Mentouri Constantine1.
Examinateurs :		
	Ramdane MAHAMDI	Prof .Université Mostefa Ben Boulaid Batna 2.
	Aziza ZERMANE	MCA. Université Mostefa Ben Boulaid Batna 2.
	Nour El Houda TOUIDJEN	MCA. Université Frères Mentouri Constantine1.
Invités :	Abdelmadjid BENGHALIA	Prof. Université Frères Mentouri Constantine1.
	Mohamed RAS LAIN	MCA. Université Frères Mentouri Constantine1.

Travail effectué au Laboratoire Hyper fréquence et semi-conducteur (LHS), Faculté des sciences de la technologie, Département d'Electronique, Université Frères Mentouri, Constantine, Algérie.

الجمهورية الجزائرية الديموقراطية الشعبية
People's Democratic Republic of Algeria
وزارة التعليم العالي والبحث العلمي
Ministry Of Higher Education and Scientific Research

Frères Mentouri Constantine 1 University 1
جامعــــة الإخـوة منـــتـــوري
قسنطينـــــة 1

Faculty of Technology Sciences
كليـــة علــــوم التـكنـولـوجيـا

Electronics department
قسم الإلكتــرونيـــك

Order N°: ….

Serial N°: ….

PhD Thesis

Presented to obtain the diploma of

Doctorate 3rd Cycle LMD

Option: **Electronic**

Specialty: **Micro- Nanoelectronic and photonic**

Presented By: **Faiza Bounaas**

Theme

Photonic crystals structures for sensing and biosensing applications

Date: 20/12/2023

In front of the Jury members:

Chairman :	Fouad KERROUR	Prof. Université Frères Mentouri Constantine1.
Advisor :	Amel LABBANI	Prof. Université Frères Mentouri Constantine1.
Examiners :		
	Ramdane MAHAMDI	Prof .Université Mostefa Ben Boulaid Batna 2.
	Aziza ZERMANE	Dr. Université Mostefa Ben Boulaid Batna 2.
	Nour El Houda TOUIDJEN	Dr. Université Frères Mentouri Constantine1.
Invited :	Abdelmadjid BENGHALIA	Prof. Université Frères Mentouri Constantine1.
	Mohamed RAS LAIN	Dr. Université Frères Mentouri Constantine1.

Acknowledgements

First and foremost, I want to express my gratitude to Allah for granting me the resilience, bravery, and endurance necessary to accomplish my doctoral dissertation.

This dissertation was carried out in the Hyper frequency and Semiconductors Laboratory (LHS) of the Electronics Department at Frères Mentouri Constantine 1 University.

Completing this dissertation would have been impossible without the generous assistance and guidance provided by individuals who offered valuable support and insights throughout my Ph.D. studies. I want to extend my profound appreciation to Professor ***Amel Labbani***, my academic mentor, whose instruction, inspiration, and unwavering support have been instrumental in my Ph.D. journey. Professor ***Labbani***'s expertise, analytical perspectives, and rigorous scientific approach enabled me to overcome numerous challenges encountered during my research works and ultimately complete this dissertation. I am profoundly grateful for her consistent patience and generous investment of time in supervising my research, for which I cannot express enough gratitude.

I would like to thank Mr. ***Fouad KERROUR***, a professor at Constantine 1 University, for the valuable attention he has given to my research by graciously accepting the role of presiding over the committee for my thesis.

I want to thank all jury members who kindly agreed to participate in this evaluation process with utmost humility and respect. I am particularly grateful to Doctor ***Aziza ZERMANE***, Doctor ***Nour El Houda TOUIDJEN,*** and Professor ***Ramdane MAHAMDI*** for their acceptance and genuine interest in my research, which fills me with great pride.

I sincerely appreciate Professor ***Abdelmadjid BENGHALIA*** and Doctor ***Mohamed RAS LAIN*** for graciously accepting the invitation to join my dissertation committee. I am truly honored by their participation, which has significantly enhanced the quality and impact of the research.

I want to express my sincere gratitude to ***Mr. Mehdi NAMOUNE*** for his invaluable help, dedicated efforts, and insightful advice throughout my dissertation journey. His support has been instrumental in shaping the development and success of this research endeavor.

I sincerely appreciate my fellow doctoral colleagues and friends at the LHS laboratory, who have provided me with varying degrees of support and camaraderie throughout my journey. Among them, I extend my gratitude to ***Bilal TEBBOUB, Imane CHERGUI***, and ***Imane MOUMENI***. As I conclude these words of appreciation, I would like to convey my best wishes for their future and the successful completion of their thesis.

Additionally, I would like to extend my appreciation to my friends for generously offering their time, guidance, and moral encouragement.

Lastly, I want to sincerely acknowledge my family, especially my beloved parents, sisters, and brothers, for their unwavering presence. Their encouragement and moral support have always been invaluable. I offer my heartfelt gratitude and assure them I will forever be deeply grateful for their unwavering support.

Content.

Content

List of Illustrations.

List of illustrations.

Chapter I

Chapter II

Chapter III

Chapter IV

List of tables.

List of tables.

List of abbreviation

List of abbreviations

PhC : Photonic crystal.
1D : One dimensional.
2D : Two dimensional.
3D : Three dimensional.
λ : wavelength peak.
Δλ : Wavelength difference.
a : Period of photonic crystal.
r : Radius of photonic crystal.
Ψ : Wave function.
ω : Pulsation.
$\boldsymbol{\varepsilon}$ **:** Dielectric permittivity.
PBG: Photonic band gap.
$\vec{k}$: Wave vector.
n : Refractive index.
TE : Transverse-electric.
TM : Transverse-magnetic.
SEM : Scanning Electron Microscope.
Ln : Linear cavity.
Hn : Hexagonal cavity.
PICs : Photonic integrated circuits.
W : Waveguide.
WDM : Wavelength Division Multiplexing.
DL : Detection limit.
S : Sensitivity.
SPR : Surface plasmon resonance.
RIU : Refractive index unit.
RI : Refractive index.
IV : Intensity variation.
FWHM : Full width at half maximum.
Q : Quality factor.
TMM : Transfer Matrix Method.
PWE : Plane Wave Expansion method.
FDTD : Finite-Difference Time-Domain method.
PML : Perfectly Matched Layer.
C\S : Core\Shell rods.
$\mathbf{n_0}$: Refractive index of Silicon pillars at 0°C.
α : Thermo-optic coefficient equal to 2.4×10-4/°C.
ΔT: Temperature difference.
VS : Vertical slot.
$\boldsymbol{f}$:Volume Fraction.
Ag NP : Silver nanoparticles.
$\boldsymbol{v^F}$= Fermi velocity.
$\boldsymbol{\omega_p}$: Plasma frequency.
$\boldsymbol{\theta}$: Incident angle.

Background and motivation.

Background and motivation

Meeting the growing industrial requirements in diverse sectors like telecommunications (covering filters, demultiplexers, and photonic crystal fibers), optoelectronics (encompassing lasers and photodetectors), and the emerging detection field presents a notable obstacle in advancing integrated photonic circuits. The key requirements for these circuits are compactness and cost-effectiveness. Consequently, innovative technological solutions have emerged, with photonics standing out as a highly promising research domain for advancing integrated optics devices.

The distinctive optical properties of photonic crystals (PhCs) have led to the creation of innovative photonic devices catering to various industries and advanced technologies. These crystals possess exceptional optical properties that enable precise manipulation of light on a nanoscale, thus revolutionizing the field of photonics and facilitating the creation of highly efficient optical devices. PhCs have gained significant attention within the integrated optics community since their discovery in 1987 [1], mainly due to their compatibility with current microelectronics manufacturing processes using silicon technology [2]. Their uses extend across diverse domains, encompassing the development of nanophotonic light-guiding circuits, all-optical filters, modulators, and a new era of photonic crystal sensors and biosensors.

Sensing and biosensing are exploitable research fields for developing biological, chemical, or physical transducers. They are based on using optical techniques to study and characterize biological and physical phenomena, such as the interaction between two molecules. This method eliminates the need for labeling target molecules and enables the real-time quantification of their presence in highly confined environments. However, the progress made on Photonic Crystals (PhCs), which enable better control of light at a nanometric resolution, offers the possibility of creating new, highly powerful detection platforms compatible with "lab-on-chip" technologies. The periodic nanostructuring of the material allows ultimate control of light in both spatial and temporal domains, making it highly sensitive to the presence of molecules and the targets to be detected.

The detection mechanisms rely on the high sensitivity of localized modes present in the transmission spectra of photonic crystals, responding to variations in the refractive index of the analyte. Photonic crystal-based sensors utilizing microcavities [3–7] have demonstrated their ability to detect biochemical elements, both theoretically and experimentally. Other authors have also proposed optical biosensors based on PhC waveguides [8,9]. Photonic crystal waveguide-based sensors coupled with resonant cavities [10-12] offer numerous advantages, including compactness, high sensitivity, and easy scalability to multichannel sensors, various material options, and the ability for parallel measurements. Recently, they have been proven theoretically and experimentally effective in detection, with the latter achieved by measuring the shift of the resonance wavelength as a function of the change in refractive index.

Rapid advances in PhCs realization and design technologies have significantly improved sensing performance, particularly in analyte-light interaction, device miniaturization, and microfluidic design and integration. The new generation of optical sensors should be reliable and portable, manufactured using current production techniques, to reduce the cost of multiparametric. This enables rapid real-time measurements of biological or physical parameters on a compact sensor chip. In this context, our thesis aims to exploit the properties of PhCs for developing and designing new optical devices for sensing and biosensing, thereby creating a monolithic platform based on one- and two-dimensional PhCs. The latter will be ideally suited for highly sensitive, label-free detection and biosensing, with detection units exhibiting a high-quality factor to capture low analyte concentrations.

The present dissertation is structured into four chapters, which are outlined as follows:

The initial chapter serves as a comprehensive review of fundamental photonic crystal concepts and their distinctive attributes, emphasizing the emergence of photonic band gaps. Following a brief exploration of their operational principles and characteristics, the narrative transitions into an in-depth examination of their guiding principles and the diverse array of photonic crystal cavities and guides. A particular focus is then directed towards scrutinizing the impact of geometric parameters on these structures, with a specific emphasis on the interaction between guides and cavities. Ultimately, the chapter concludes by underscoring the potential of these photonic structures in the design and implementation of various devices, such as filters, wavelength demultiplexers, and all-optical sensors.

In the second chapter, we focus on optical sensors. We begin this section by briefly explaining general notions and concepts related to optical transducers, explicitly focusing on optical biosensors. Subsequently, we present a comprehensive review of the current state of photonic crystal biosensors, focusing on refractive index biosensors. In the following step, we delve into a detailed explanation of the detection mechanism. Finally, we summarize the existing research in this area and provide a concise overview of the various structures.

Given the innovative nature of photonic crystal structures in integrated optics, their effective design requires a comprehensive grasp of modeling tools. Consequently, the third chapter serves as an introduction to various numerical methods, including the plane wave method (PWE), the finite difference time domain technique (FDTD), and the transfer matrix method (TMM). Furthermore, we introduce the use of RSOFT software (Fullwave and Bandsolve) for modeling photonic crystal structures within this study. Leveraging these modeling tools enables the generation of dispersion diagrams, exploration of the optical characteristics of photonic crystal structures, and visualization of electromagnetic field distributions.

The fourth chapter focuses on examining and developing refractive index sensors that utilize photonic crystals, which is divided into two primary sections. The initial section explores the examination of a device based on a two-dimensional photonic crystal, which can detect temperature changes using a ring resonator configuration. The resonator, positioned between two linear waveguides, consists of core/shell particles that offer high sensitivity and a high-quality factor. We employed one-dimensional photonic crystal-based sensors in the second section to identify cancerous cells. We opted for the 1D PhC due to its uncomplicated structure, compactness, and cost-effectiveness. In the first section, the detection mechanism relies on the shift in resonance wavelength caused by the thermos-optic effect applied to the silicon rods. However, in the second section, the sensing principle is based on the shift in the resonant peak, resulting from a variation in the analyte's refractive index (RI). The findings from each study are presented and analyzed, emphasizing the significance of carefully selecting both the material and geometric parameters to optimize the sensor's performance.

References

[1] E. Yablonovitch, Inhibited Spontaneous Emission in Solid-State Physics and Electronics, Phys. Rev. Lett. 58 (1987) 2059–2062. https://doi.org/10.1103/PhysRevLett.58.2059.

[2] S. Matsuo, A. Shinya, C.-H. Chen, K. Nozaki, T. Sato, Y. Kawaguchi, H. Taniyama, M. Notomi, 20-Gbit/s directly modulated photonic crystal nanocavity laser with ultra-low power consumption, Opt. Express, OE. 19 (2011) 2242–2250. https://doi.org/10.1364/OE.19.002242.

[3] E. Chow, A. Grot, L.W. Mirkarimi, M. Sigalas, G. Girolami, Ultracompact biochemical sensor built with two-dimensional photonic crystal microcavity, Optics Letters. 29 (2004) 1093–1095.

[4] L. Huang, H. Tian, D. Yang, J. Zhou, Q. Liu, P. Zhang, Y. Ji, Optimization of figure of merit in label-free biochemical sensors by designing a ring defect coupled resonator, Optics Communications. 332 (2014) 42–49.

[5] L. Huang, H. Tian, J. Zhou, Q. Liu, P. Zhang, Y. Ji, Label-free optical sensor by designing a high-Q photonic crystal ring–slot structure, Optics Communications. 335 (2015) 73–77.

[6] C. Qi, W. Shutao, L. Jiangtao, L. Na, P. Bo, Refractive index sensor based on photonic crystal nanocavity, Optics Communications. 464 (2020) 125393. https://doi.org/10.1016/j.optcom.2020.125393.

[7] Ankita, B. Suthar, A. Bhargava, Biosensor Application of One-Dimensional Photonic Crystal for Malaria Diagnosis, Plasmonics. 16 (2021) 59–63. https://doi.org/10.1007/s11468-020-01259-8.

[8] L. Kassa-Baghdouche, E. Cassan, Sensitivity analysis of ring-shaped slotted photonic crystal waveguides for mid-infrared refractive index sensing, Opt Quant Electron. 51 (2019) 328. https://doi.org/10.1007/s11082-019-2040-4.

[9] N. Skivesen, A. Têtu, M. Kristensen, J. Kjems, L.H. Frandsen, P.I. Borel, Photonic-crystal waveguide biosensor, Optics Express. 15 (2007) 3169–3176.

[10] T. Zouache, A. Hocini, X. Wang, Cavity-coupled photonic crystal waveguide as highly sensitive platform for pressure sensing, Optik. 172 (2018) 97–106.

https://doi.org/10.1016/j.ijleo.2018.06.120.

[11] F. Rahman-Zadeh, M. Danaie, H. Kaatuzian, Design of a highly sensitive photonic crystal refractive index sensor incorporating ring-shaped GaAs cavity, Opto-Electronics Review. 27 (2019) 369–377. https://doi.org/10.1016/j.opelre.2019.11.007.

[12] D. Benelarbi and T. Bouchemat, “Étude de cristaux photoniques en silicium pour l’application à la biodétection,” 2018. [Online]. https://bu.umc.edu.dz/md/index.php?lvl=author_see&id=39044.

Chapter I.

Photonic crystal from physic to application.

1. Introduction

Photonic crystals (PhCs), the electromagnetic analog of semiconductor crystals, have motivated the design of photonic integrated circuits. The integration of these structures at the nanoscale makes it possible to reduce the size of the component, reduce costs, and allow considerable optical complexity [1,2]. The propagation of optical waves in a periodic medium (Bragg mirror) was initially studied by Lord Rayleigh in 1887 [3]. However, a century later, when Eli Yablonovitch [4] and Sajeev John [5] combined the tools of conventional electromagnetism and solid-state physics, that the omnidirectional electromagnetic band gap was explored for PhCs in two and three dimensions, to control and localize the light in the defects of a periodic lattice of appropriate dimensions. In 1991, the first structure with a photonic bandgap was fabricated by piercing holes in a dielectric at three different angles [6]. In this context, we realize, as an application, several devices, such as Bragg mirrors or Fabry Perot dielectric filters, which have unique reflection and transmission characteristics.

This chapter introduces the theoretical basis of photonic crystals, relying on a non-exhaustive review of their different categories. We briefly present the optical features of these periodic structures. Then, we describe the principle and the different types of defects based on PhCs. Finally, we end with a general presentation of their applications.

2. What is Photonic Crystal ?

Photonic crystals (PhCs) are periodic dielectric materials specifically designed to inhibit, manipulate, or control light propagation in specific directions and at specific frequencies [7]. Due to this periodicity, their behavior is analogous to that of semiconductors in solid-state physics. The regular arrangement of atoms in a lattice and the periodicity of the electronic potential in semiconductors give rise to electronic bandgaps, which are prohibited energy bands for electrons. Similarly, photonic bandgaps, or prohibited energy bands for photons, are generated by the periodicity of the refractive index. Depending on the dimensionality of such periodicity, photonic crystals can be one-dimensional (1D), two-dimensional (2D), or three-dimensional (3D). Figure 1 illustrates the evolution of these periodic structures from one to three dimensions [8].

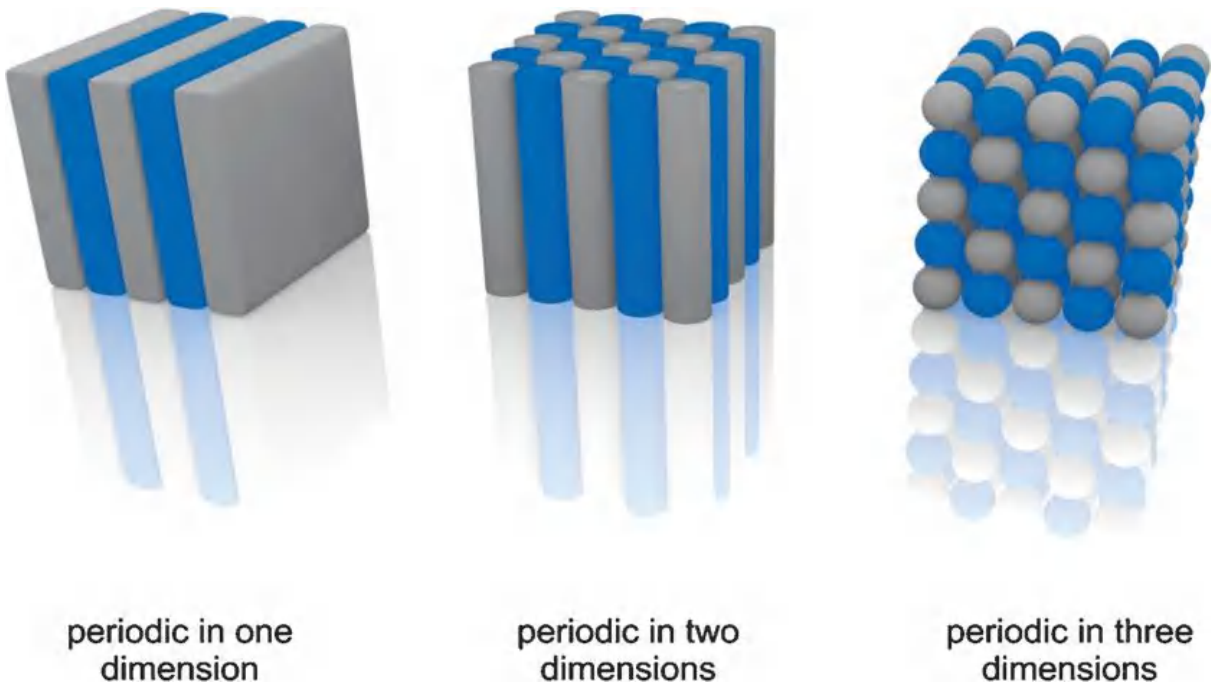

Figure I. 1. Schematic illustration of the different kinds of PhCs.

The definition of PhCs refers mainly to artificial structures. However, similar periodic structures are observed in nature. The beautiful colors of some animals, plants, and stones come from light interactions with periodic structures. A well-known example of a gemstone that exhibits an opalescence, or play of colors, that varies with the angle of incidence is the natural opal (Figure 2 (a, b)). In the mid-1970s, it was believed that this effect was caused by contaminants that were absorbed through the stone's internal fissures or by liquids that were trapped within. The opalescence occurs by Bragg diffraction from periodically stacked silica particles, of uniform size, within the stone. The particle generally have diameters between 200 and 600 nm [9]. The brilliant blue color of Morpho rhetenor butterflies whose scales are formed by multilayers of cuticle and air, serve as diffraction gratings for incident light (Figure 2(c, d)). Depending on the angle of incidence, the color changes from blue to dull brown when the wings are turned over [10]. Another example is the shiny appearance of the spines of the sea mouse (Aphrodite) in Figure 2 (e, f). The spine consists of hollow cylinders organized hexagonally in a chitin matrix resembling a PhC fibre [11]. The peacock feathers are no less fascinating, especially the eye-shaped patterns outlined in a white rectangle (Figure 2 (g, h)). Barbules of different colors form the patterns. A barbule consists of air cores (3 μm) covered by layers of cortex. The cortex contains a 2D periodic structure of melanin rods connected by keratin. Varying the spacing between rods causes the rods to exhibit different colors [12,13] .

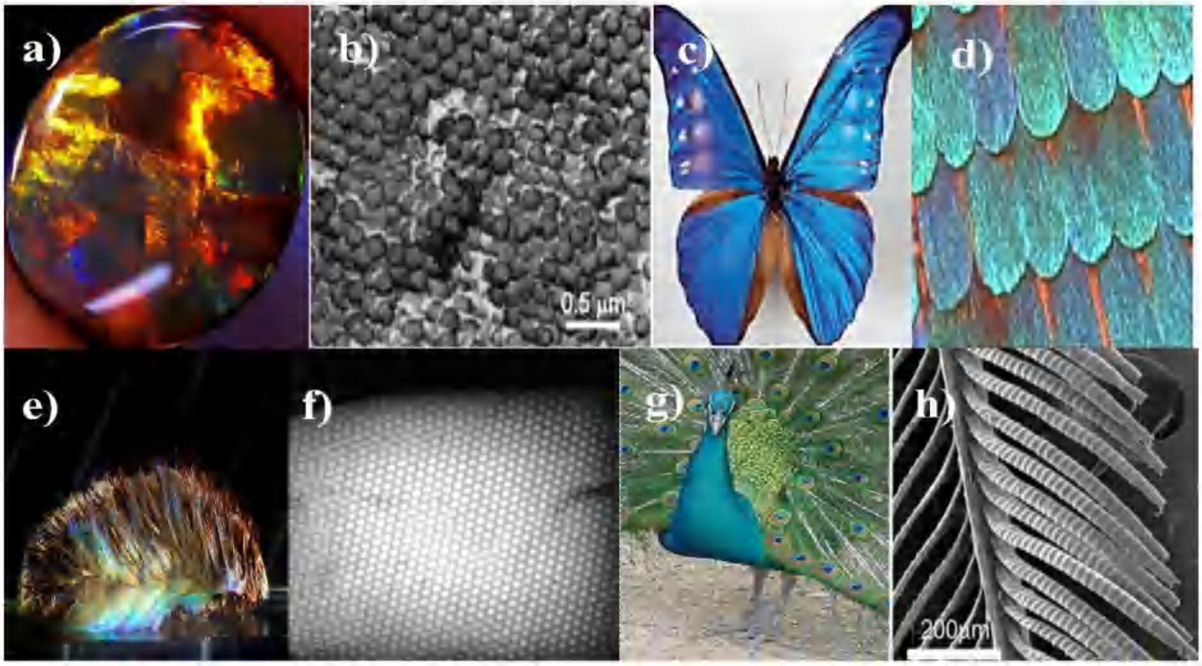

Figure I. 2. Examples of natural photonic crystals: (a) natural opal (b) SEM image of natural opal (c) Morpho rhetenor butterfly (d) details of its scales [14] (e) the sea mouse (f) EM of a section of the spine [11] (g) a peacock (h) SEM image of barbules [13].

3. Basic Concept

The electron-photon analogy results from the similarity between the Schrödinger equation governing the propagation of electrons in a material characterized by a periodic electrostatic potential and Maxwell's equations used to describe the propagation of an electromagnetic wave in a material characterized by its periodic dielectric constant.

The stationary Schrödinger equation for the wave function Ψ of an electron in a potential V is expressed as:

$$\nabla^2\Psi\,(r) = -\frac{2m}{\hbar}(E - V(r))\Psi(r) \tag{I.1}$$

where

E is the energy of the electron, *m* its mass

r: position vector, $\hbar$: Planck's constant.

The equation for a monochromatic electromagnetic wave's propagation in a medium is provided by :

$$\nabla\times[\nabla\times E(r)] = \frac{\omega^2}{c^2}\varepsilon_r(r)E(r) \tag{I.2}$$

where ω is the pulsation, ε_r is the relative permittivity, and *c* is the light velocity in a vacuum.

Equation (1) describes the possible values of the energy of an electron propagating freely in a potential and the associated wave functions. In contrast, equation (2) determines the possible values of the frequency of a wave propagating in a material without external excitation and the amplitudes of the associated fields.

Comparing the previous two equations (1) and (2) demonstrates that the relative dielectric permittivity $\varepsilon_r(r)$ displayed in Maxwell's equation is analogous to the potential *V(r)* in Schrödinger's equation. In Maxwell's equation, *E(r)* is the electromagnetic equivalent of the electronic wave function *Ψ(r).* The periodic variations of relative permittivity $\varepsilon_r(r)$ lead to the appearance of PBGs for photons within frequency ω , wherein the light cannot propagate through the given structure. Moreover, not being absorbed, this light will be reflected.

This formal analogy between electrons and photons will allow us to apply the tools and concepts developed in solid-state physics, such as the notions of the reciprocal lattice, Brillouin zone, and Bloch's theorem, for the resolution of the wave equation.

4. Different Structures of Photonic Crystals

4.1. One-dimensional Photonic Crystal (Bragg Mirrors)

Bragg mirrors are a common name for these structures (Figure 3). They are made up of a stack of periodic dielectric layers with different dielectric permittivity (ε_1, ε_2) and a thickness of λ/4, where λ is the wavelength at which the material should prevent light from propagating through it at normal incidence [15]. These structures provide dispersion diagrams but are sensitive to the wave's angle of incidence. The mirror will work as a Bragg-reflecting Interface (BRI) as we will explore further if the refractive index contrast, Δn, between the two materials that make it up, is sufficient.

This kind of structures is comparatively easy to implement compared to 2D and 3D PhCs [16]. The photonic crystal mirror exhibits a distinct advantage over the conventional Bragg mirror due to its ability to achieve a high reflectance nearly 100% of the incident light with fewer layers, consequently eliminating mechanical constraints. This achievement is related to a significant index contrast.

Bragg mirrors have proven their usefulness in numerous applications, including selective wavelength filters, multiplexers, mode converters for optical fibers, dispersion compensation, and lasers...

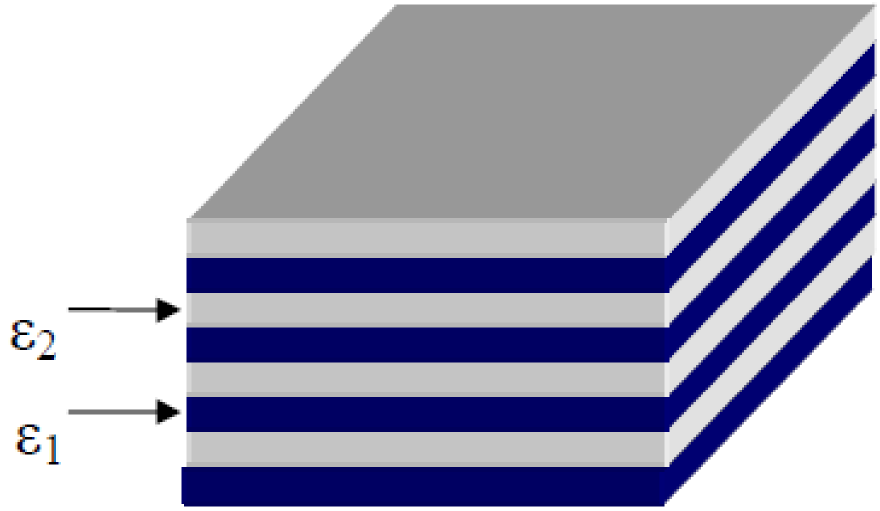

Figure I. 3. Schematic presentation of one-dimensional periodic structure 1D.

4.1.1. Notion of Photonic Band Gap

To illustrate the phenomenon of photonic band gap (PBG) and its characteristics, we will use the classical Bragg mirror as an example (as shown in Figure 4). When an electromagnetic wave with a wave vector $\vec{k}$ is incident normally on a crystal and the thickness of each layer is appropriately selected, the phase difference between two reflected waves for successive periods is given by $2ka$. If the value of $2ka$ is not equal to 2π, it results in the absence of constructive interference among the successively reflected waves. This occurs specifically at the edges of the Brillouin zone, for values of k ranging from $-\frac{\pi}{a}$ and $\frac{\pi}{a}$, where the successively reflected waves are in phase [17].

The incident wave with wave vector $\vec{k}$ gives rise to a reflected wave with wave vector -$\vec{k}$ due to the periodicity of the dielectric medium. These two waves, with the same pulsation ω_0, generate two eigenstates of energies ω_1 and ω_2, resulting in the lifting of degeneracy and the opening of a frequency band gap for propagation in the direction normal to the stack. When the optical thicknesses of the different layers are equal ($n_1a_1 = n_2a_2$), the width $\Delta\omega$ of this band gap depends solely on the index contrast [18].

$$\Delta\omega = \frac{4}{\pi}\omega_0 \sin^{-1}\left|\frac{n_1-n_2}{n_1+n_2}\right| \tag{I.3}$$

where n_1 and n_2 are the refractive indices of the two dielectric materials.

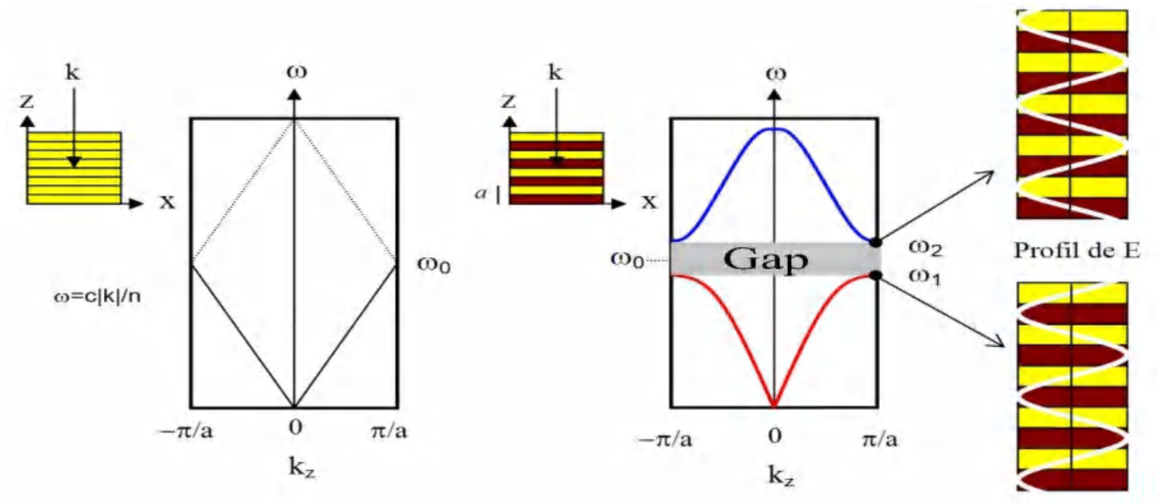

Figure I. 4. Schematic representation of the photonic band gap of a Bragg mirror consisting of multiple alternations of two different materials with different indices $n1$ and $n2$. A band gap appears at the edge of the Brillouin zone (between frequencies $\omega 1$ and $\omega 2$.

The alternation of dielectric layers of different indices forms a photonic band gap. The position and width of this Photonic band gap can therefore be controlled by adjusting the geometrical parameters and the index contrast between the different permittivities. When the contrast is low, the width of the PBG is narrow (see figure 4(b)), and when the contrast is high, it significantly increases (Figure 4(c)).

a) b) c)

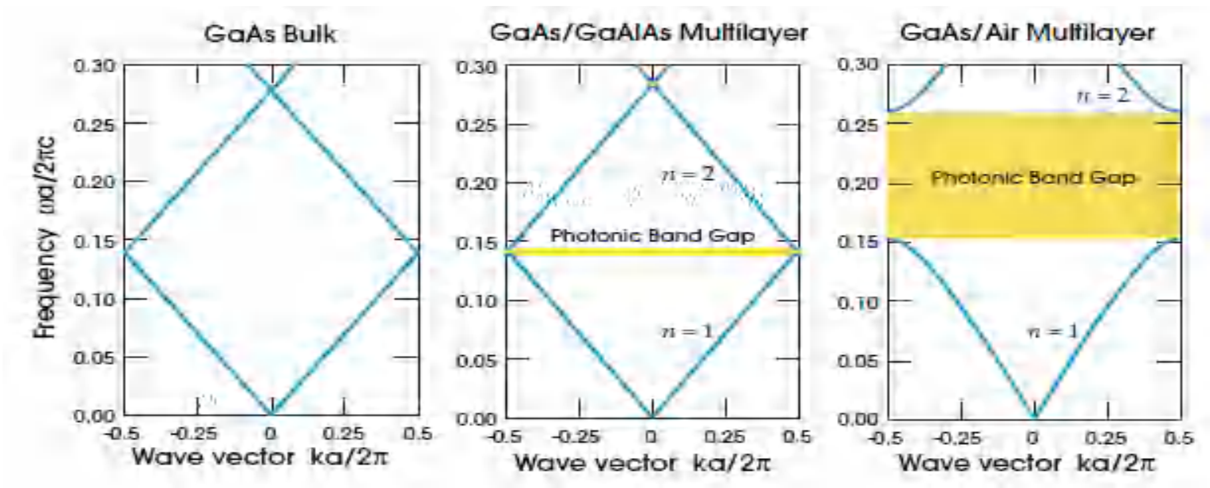

Figure I. 5. Diagram dispersion of 1D-PhC consisting of different materials with dielectric constant ε_1 and ε_2 and diameters d= 0.5a. (a) ε_1= ε_2=13 (GaAs) (b) ε_1= 13(GaAs) ε_2=12 (GaAlAs) (c) ε_1= 13(GaAs) ε_2=1 (Air).

4.2. Two-dimensional Photonic Crystal

Two-dimensional photonic crystals (2D) have been instrumental in developing micro-nano-photonics recently. This is due to the well-established manufacturing tools from microelectronics that enable the creation of submicrometer-sized structures. Moreover, they present a relative geometric simplicity that facilitates theoretical modeling and experimental studies.

A two-dimensional photonic crystal is characterized by a periodic modulation of the dielectric constant in two directions while remaining homogenous in the third. Dielectric rods can be positioned in the air or another dielectric medium to construct these structures. A wide 2D photonic bandgap requires a significant index contrast [19].

To study the behavior of an electromagnetic wave inciding on such a structure, two polarizations are possible: transverse-electric (TE) and transverse-magnetic (TM) as depicted in Figure 8. In these plans, the TE modes have their $\vec{H}$ vector perpendicular to the (x,y) plane, and their $\vec{E}$ vector lies within the (x,y) plane. The TM modes have opposite symmetries. As long as the structure remains perfectly symmetrically concerning these planes, the coupling between TE and TM modes is zero.

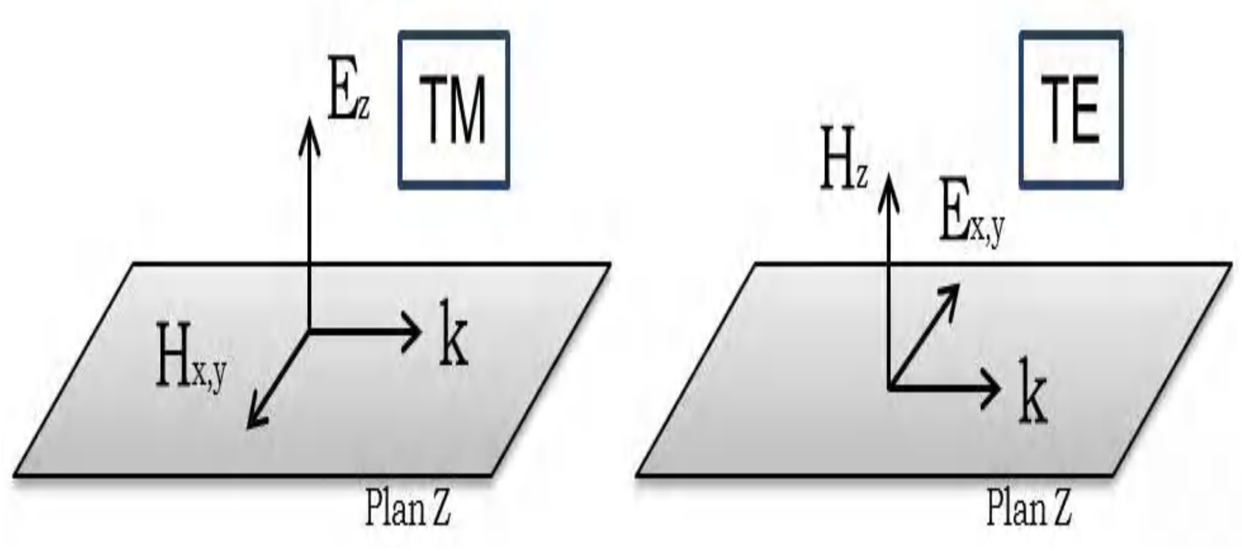

Figure I. 6. Illustration of TE and TM polarization of 2D photonic crystal.

4.2.1. The Reciprocal Lattice and The Brillouin Zone

Two-dimensional photonic crystal are mainly grouped into three categories, which are the square, triangular and hexagonal lattices (Figure 9) [20,21].

The photonic bandgap diagram is represented by wave vector components varying along the directions of high symmetry. These points are located in the first Brillouin zone, part of the reciprocal lattice. These two important concepts, namely the reciprocal lattice and the Brillouin zone, will be recalled later in this final paragraph.

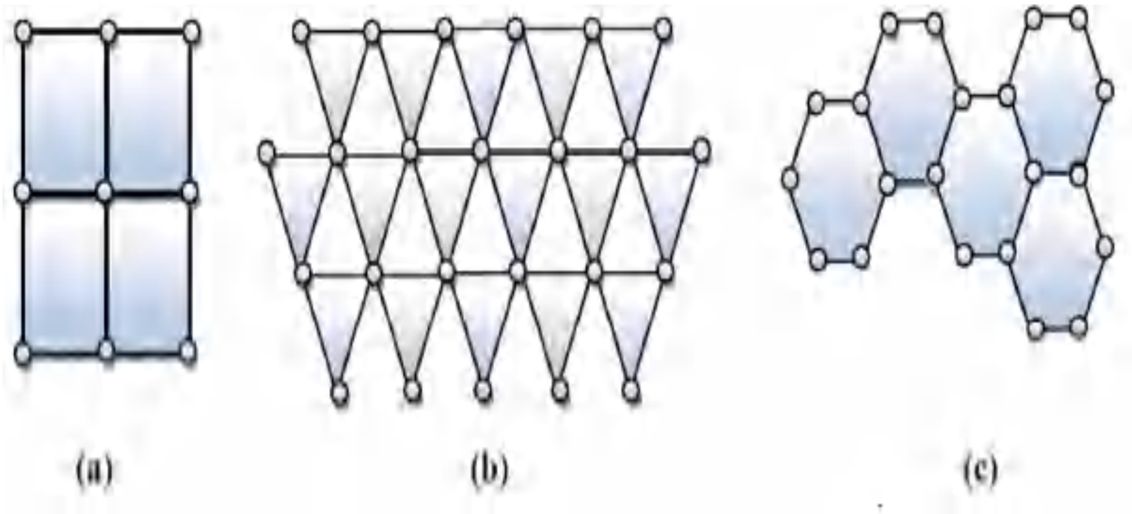

Figure I. 7. Two-dimensional structure (a) square lattice (b) triangle lattice (c) hexagonal lattice.

4.2.1.1. The Reciprocal Lattice

The reciprocal lattice of a 2D photonic crystal is defined from the original (or direct) lattice by a basis of eigenvectors $\vec{b}$ defined using the dot product:

$$\overrightarrow{a_\iota}.\overrightarrow{b_\iota} = 2\pi\overrightarrow{\delta_{\iota\jmath}} \tag{I.4}$$

where $\vec{a}$ and $\vec{b}$ are the vectors of the real and reciprocal lattices, and $\overrightarrow{\delta_{\iota\jmath}}$ is the Kronecker symbol. The reciprocal lattice of each structure can also be obtained by drawing lines connecting a given node of the direct lattice to all its neighbors, and then by drawing the medians of these segments.

4.2.1.2. The Brillouin Zone

The frequency of plane waves propagating in a two-dimensional structure forms a periodic function of the vector $\vec{a}$, which defines the propagation direction throughout the reciprocal space.

The smallest zone defined by these vectors $\vec{a}$ is a fundamental zone called the first Brillouin zone. The latter corresponds to the zone defined by the principal planes between each motif of the lattice representing the high symmetry points of the reciprocal lattice. Therefore, the irreducible Brillouin zone is the smallest zone intercepted by these principal planes; it contains all the wave vectors of the photon that allow a complete description of the band diagram (Figure 10).

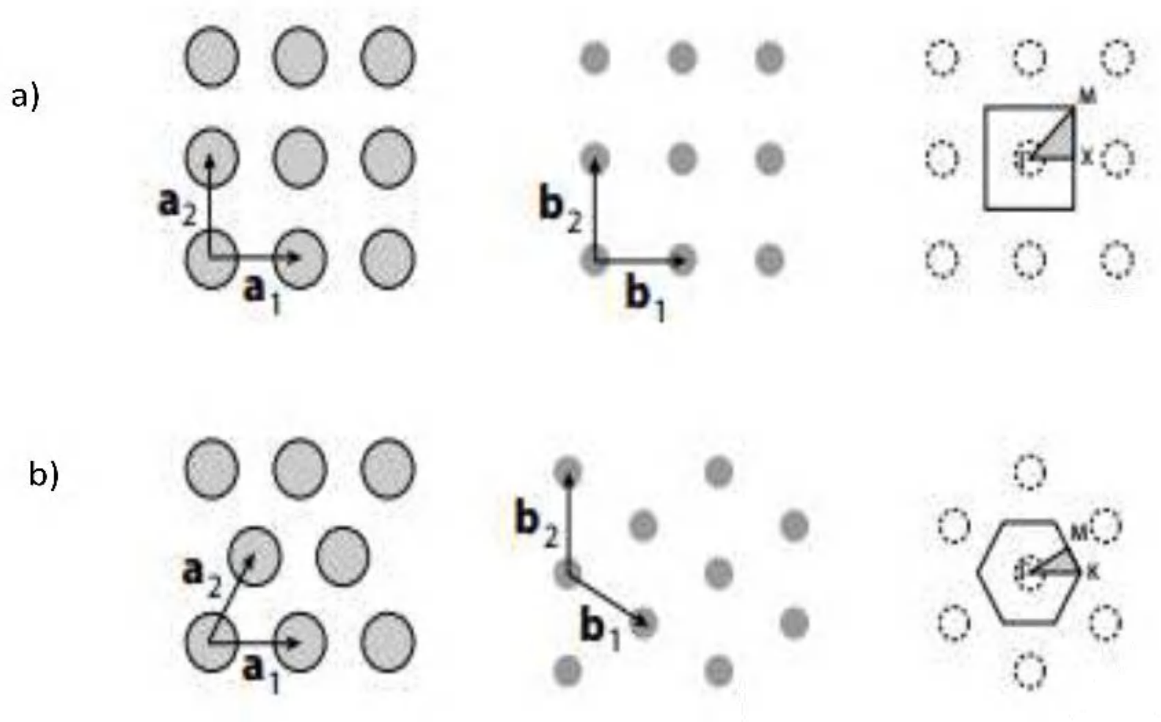

Figure I. 8. Direct lattice, reciprocal lattice, and Brillouin zone with the symmetry points of the two most used lattices: (a) square lattice, (b) triangular lattice.

4.2.2. The Band Diagram

The band diagram represents the variations of the allowed frequencies in a periodic lattice as a function of the wave vector along the high symmetry directions *ΓM*, *ΓK* and *KM*. In other words, it represents the possible modes as a function of wavelength and wave vector. Figure 11 shows an example of a structure consisting of a triangular array of air holes in a dielectric matrix (ε = 11.6) for a ratio r/a = 0.43, where r and a are the radius of the holes and the period of the array. The polarization of the light plays an essential role in the interpretation of the band diagram. Indeed, depending on whether we consider the polarization TE (Transverse electric) or TM (Transverse magnetic); the allowed or forbidden energy bands will be different. For this case, a large photonic band gap appears for TE polarization and a smaller band for the TM polarization, when the PBGs of these two polarizations overlap, we speak of a complete band gap (absolute gap). Moreover, the appearance of band gaps as well as their width and position depend in particular on the geometrical parameters of the structure.

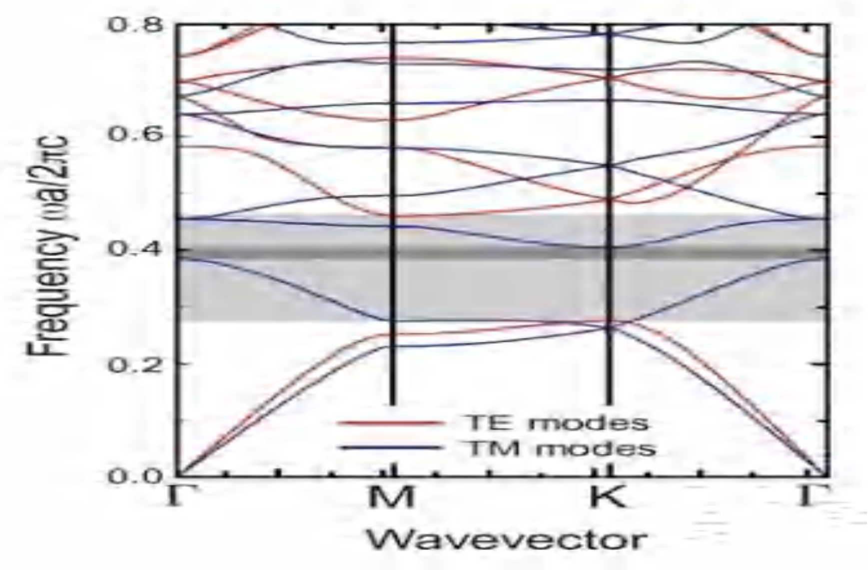

Figure I. 9. Band diagram of hexagonal lattice of air holes in silicon background (ε=11.6) for TE and TM polarization [22]

4.2.3. The Photonic Gap Maps

The band gap maps represent the photonic band gap edges and show their positions for a given lattice as a function of the filling factor *f*. In addition, they provide an overview of the possibilities of light confinement within the photonic crystal. Figure 12 shows the gap map of a 2D triangular lattice of air pores in a dielectric matrix (ε= 12.08) obtained for different air-hole radii [23]. The appearance of the absolute band gap is observed at a radius of 0.404*a*, where *a* represents the lattice constant. As the radius increases, the gap broadens and attains a maximum band gap value of 0.0794 *a*/λ at the mid-gap frequency of 0.4785 *a*/λ when the radius measures 0.48*a*.

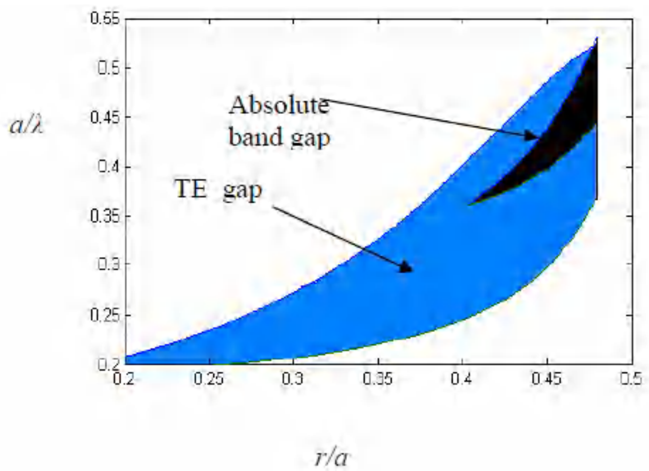

Figure I. 10. Band gap map of 2D- PhC triangular lattice structure consisting of air pores in silicon.

4.3. Three- dimensional Photonic Crystal

The three-dimensional structures are systems whose dielectric constant is periodically organized in the three directions of space, as their name indicates. After the Bragg mirrors, they were Yablonovitch's second realization. His objective was to prevent light from spontaneously emitted in all directions of space. Thus, the yablonovite shown in Figure 5 was the first 3D photonic crystal created by E. Yablonovitch [24]. Designed to operate at centimeter wavelengths (microwave domain), this structure is manufactured by mechanically drilling holes at well-selected angles in a Plexiglas block with a refraction index of 3.6 to regain the crystalline structure of the diamond, which is also that of silicon. Over the years, several research has focused on the different possible geometric structures and their manufacture while seeking to reduce the size of patterns to generate photonic crystals with a photonic band in near-infrared and visible [25]. Most three- Dimensional structure is inspired by the geometry of the diamond structure (face-centered-cubic).

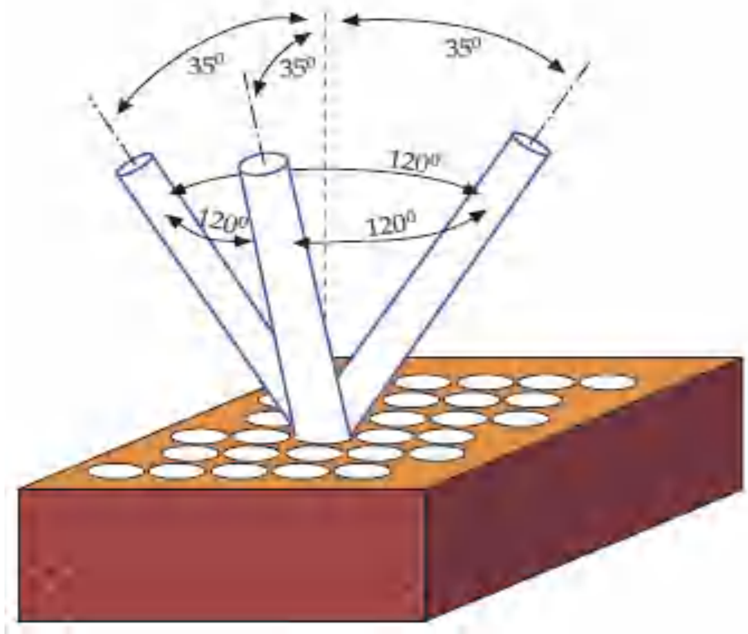

Figure I. 11. Schematic illustration of 3D structure 'the yablonovite'.

4.3.1. Woodpiles Structures

The first three-dimensional photonic crystal, with a complete bandgap for infrared light, was proposed by Ho et al. [26] and Sözüer and Dowling [27] and has been defined as a woodpile structure. This structure is formed by a stack of dielectric (usually rectangular) rods with altered orthogonal orientations. The main advantage of this structure lies in the fact that it can be manufactured in the form of a sequence of layers deposited and modeled by lithographic techniques developed for the semiconductor electronics industry.

In 1998, Lin et al. [25] fabricated a polycrystalline silicon ribbons within silica trenches structure; the forbidden band was measured around a wavelength of 12 µm (Figure .6). Subsequently, Lin and Fleming [28] reduced its size by almost an eight factor, resulting in a bandwidth around a wavelength of 1.6 µm. The band diagram of this structure, for a dielectric contrast of 13, is presented in Figure 6(b), which consists of an opening of a complete forbidden photonic band.

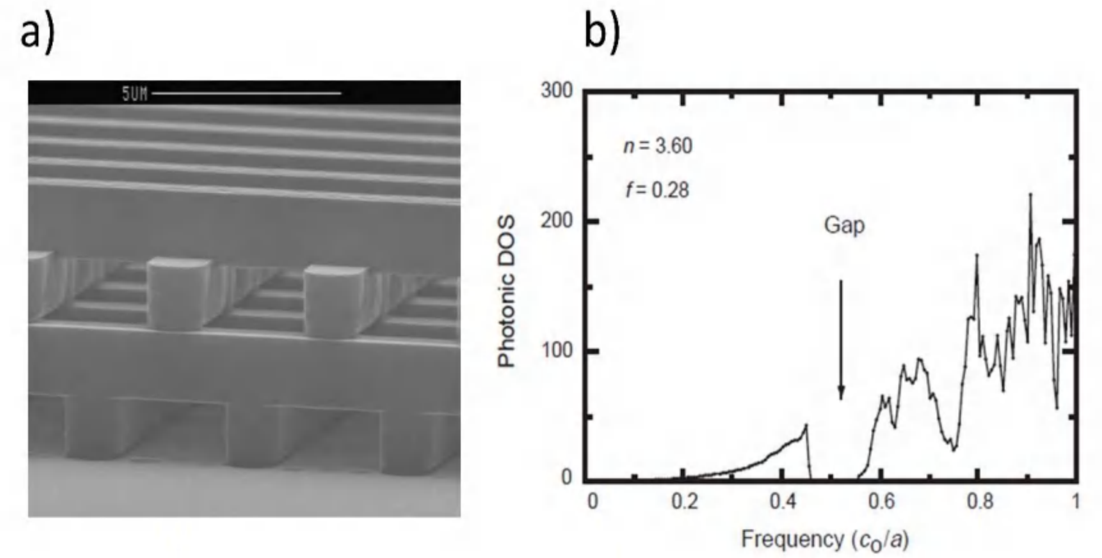

Figure I. 12. (a) Electron microscope image of silicon woodpile structure (b) the photonic bandgap of the same structure [25].

4.3.2. Opal Structures

Another category of structures has been extensively studied, mainly to control spontaneous emission based on the organization of spherical atoms; in this case, the reverse opal and opal structures are used Figure 7(a, b) [29]. The first opal was obtained by sedimentation of silica spheres in solution arranged according to face-centred-cubic. The significant number of defects in the first opals was greatly reduced thanks to self-organized development processes proposed by YA. Vlasov [29]. The reverse structure is made from the classic structure by high-index material infiltration between the spheres. These initial spheres are then dissolved to result in the final structure of air spheres in a high index matrix. Due to the low index contrast, most colloidal crystals do not have band gaps.

The development of such devices (3D structures) at scales sufficiently small for optics remains a significant difficulty, particularly in obtaining a bandgap in the range of near-infrared or visible wavelengths. The electronic lithography manufacturing technique allows engraving of a wide variety of patterns in these structures. Nevertheless, it still presents the disadvantage of being expensive and limited to dimensions of the order of a few microns. Hence the complexity and difficulty of creating defects (holes or guides) in such structures or their integration into existing optical devices. Therefore, most of the research work concerns one-dimensional and two-dimensional photonic crystals, which are easier to fabricate and more accessible to various methods of digital study and manufacturing on the scale of integrated optics.

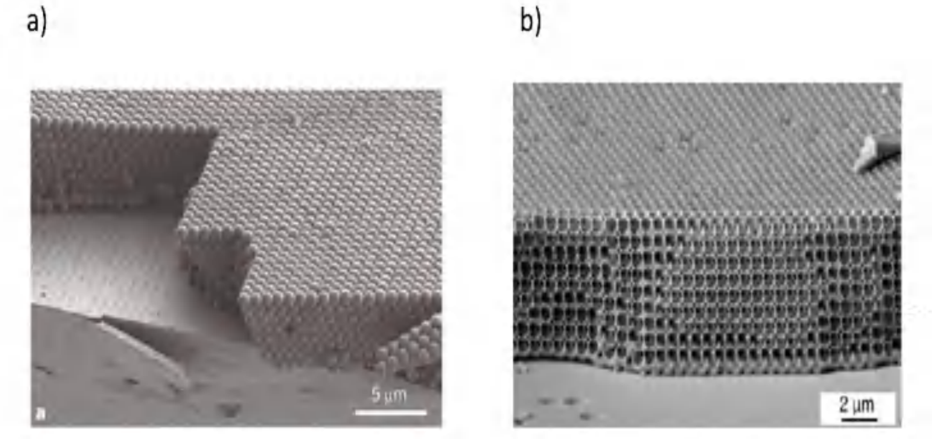

Figure I. 13. (a) SEM image of planar opal assembled directly on a Si substrate from 855 nm spheres. (b) SEM image of reverse opal structure [29].

5. Photonic Crystal Defects

The main property of PhCs is their ability to localize and confine light. This characteristic is achieved by introducing defects, which locally break the periodicity of the structure. Introducing defects in perfect PhCs can create resonant states in the photonic band gap. Therefore, the defect states in the PBG could be tuned in frequency according to the design interest. In addition to frequency tuning, these defects must be controlled concerning the symmetry of the localizing photon state. All of these features provide a new "dimension" in the ability to control or model the properties of light. The following section discusses the various types of defects that can be formed in the PhC and their properties.

5.1. One-dimensional Photonic Crystal Defect

Introducing a defect in a photonic crystal aims to have a propagation frequency allowed inside a photonic band gap. This defect is obtained by modifying the periodicity of the crystal, where a single layer can constitute this defect by changing its width. Such a structure is depicted in Figure 13. The multilayer structures on each side of the cavity behave like frequency-specific mirrors. The defects allow localized modes with frequencies in the photonic band gap. This characteristic realizes applications such as the Fabry-Perot filter, which operates as a bandpass filter. Dielectric materials exhibit low losses at visible-light frequencies, providing them with highly advantageous properties [30].

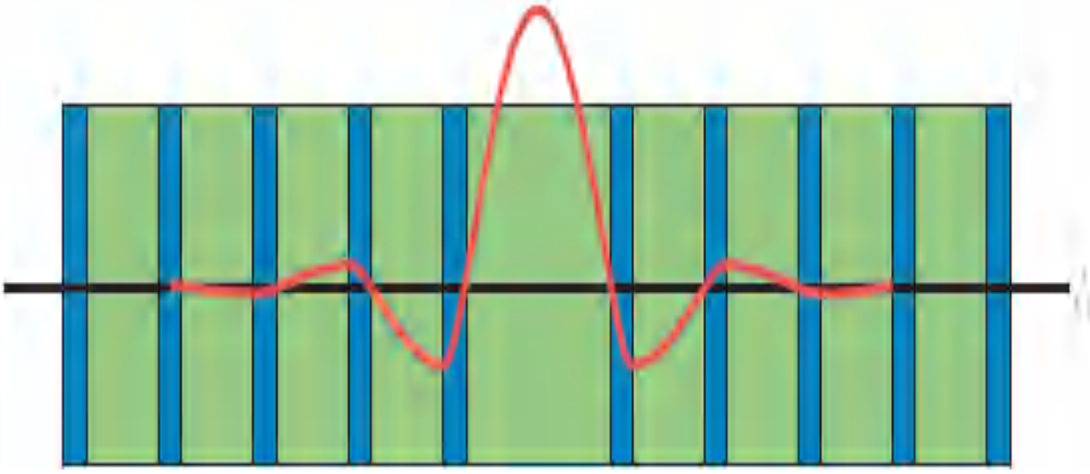

Figure I. 14. A defective multilayer structure results from doubling the thickness of a layer with low dielectric constant. The electric-field strength of the defect state associated with this structure is represented by the red curve.

5.2. 2D and 3D Photonic Crystals Defects

These defects are made of 1D guides oriented in different directions to carry the light on all optical paths inside the crystal. Several types of these defects allow specific applications such as high selectivity filters since only the electromagnetic wave whose frequency corresponds to the permitted mode will be transmitted.

5.2.1. Point Defects and Cavities

The creation of a cavity can be achieved through the introduction of one or multiple defects. This procedure can be accomplished through the addition or removal of one or multiple crystal patterns. The defect can be acquired through the local alteration of the patterns' shape, size, or dielectric constant, as depicted in figure 14. The manipulation of these parameters enables the adjustment of the number of modes that are supported by the cavity and their corresponding resonant frequencies. These point defects trap electromagnetic modes, leading to the formation of optical cavities. The efficiency of light trapping in an optical cavity can be described by the quality factor (Q), which determines the lifetime of a photon's existence within the cavity and allows for measuring the capacity of a defect to conserve energy [31].

The quality factor (Q-factor) of a cavity is a crucial parameter in the design of high-density wavelength filtering and multiplexing systems. The high-quality factor of microcavities is contingent upon the depth of the holes and the dielectric constant of the materials. PhC microcavities are particularly appealing for conducting experiments in cavity quantum electrodynamics due to their exceptional combination of high quality factor and extremely low mode volume. The defect microcavity's compact size and high spontaneous emission-coupling factor render it an attractive candidate for low-threshold light sources [32]. Several results have been reported through both theoretical and experimental means since that time. Developing simple and useful techniques to tune the resonance wavelength has been the subject of research because the majority of works demand a specified operating wavelength. Therefore, several studies have been made to apply easy and practical tuning of the resonant wavelength. This wavelength is significantly influenced by the dielectric constant and cavity size.

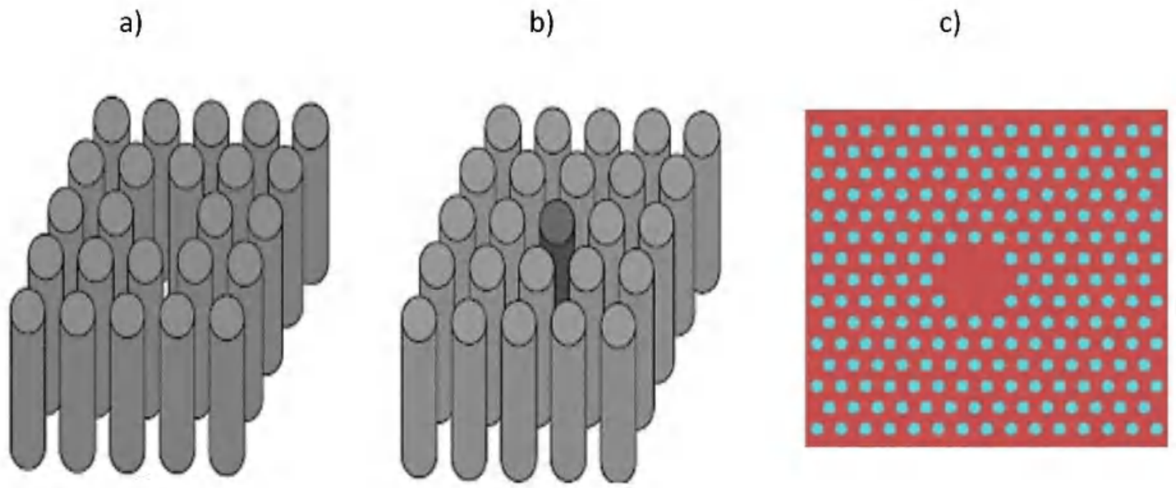

Figure I. 15. Photonic crystal cavities (a) removing a cylinder rod (b) changing the dielectric constant of the rod (c) removing 7 holes in the middle of the PhC [31].

As illustrated in Figure 15, Photonic crystal cavities are mainly divided into three main categories:

- The linear and hexagonal cavities, abbreviated as Ln and Hn, are created by removing one or more air holes in the ΓK direction of the photonic crystal. These cavities are commonly used in photonic applications. An image of an L3-type cavity example is illustrated in Figure 15(a), captured through a scanning electron microscope (SEM).
- Heterostructure cavities are based on a progressive modulation of the period of the photonic crystal (Figure 15(b)).
- The ring cavities correspond to the suppression of specific points of the lattice to form one or more rings and generate localized optical modes that resonate in these rings (Figure 15(c)).

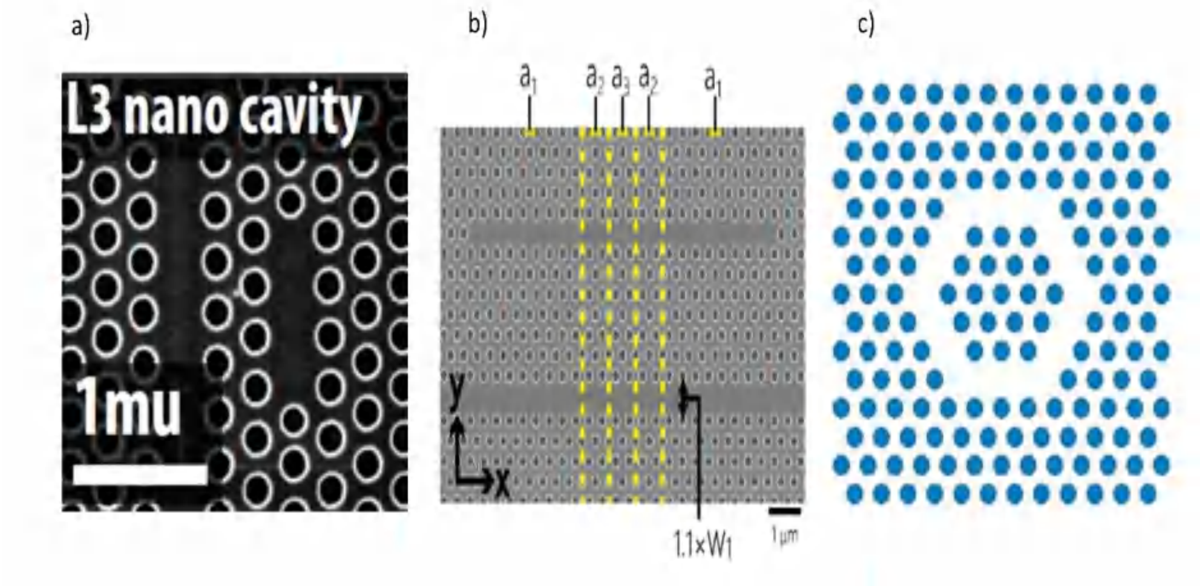

Figure I. 16. Different defect of photonic crystals cavities (a) L3 cavity [33] (b) SEM picture of heterostructure cavity [34] (c) ring resonator [35].

5.2.2. Linear Defects and Waveguides

Waveguides are essential in photonic integrated circuits (PICs), as they connect various functional elements, including multipliers, detectors, sources, and modulators. Their role is crucial in ensuring the effective operation of the circuits. Linear defects are obtained by creating a linear defect into a photonic crystal by omitting or modifying one or more unit cells of the lattice of the photonic crystal (Figure 16). The light, not being able to penetrate within the photonic crystal, is forced to propagate along the defect: a waveguide has thus been realized. The electromagnetic modes associated with this waveguide having a frequency within the photonic band gap of the PhC are confined modes and can propagate along this guide.

Waveguides consisting of missing row guides, oriented in the directions of the symmetry of the photonic crystal, are one of the main categories of photonic crystal guides. Photonic crystal waveguides are called Wn (W: abbreviation of Waveguide), where n is the number of missing array rows. A W_1 guide corresponds to a photonic crystal with one missing motif row. Figure 17 (a) illustrates a 2D photonic crystal with a hexagonal lattice of air pores in a silicon matrix. The pores have a relative radius of 0.43. By introducing a line defect (W_1) in the structure, Figure 17 (b) shows the presence of a band gap in the TE region, ranging from 0.275 to 0.460 frequency units, accompanied by multiple defect states.

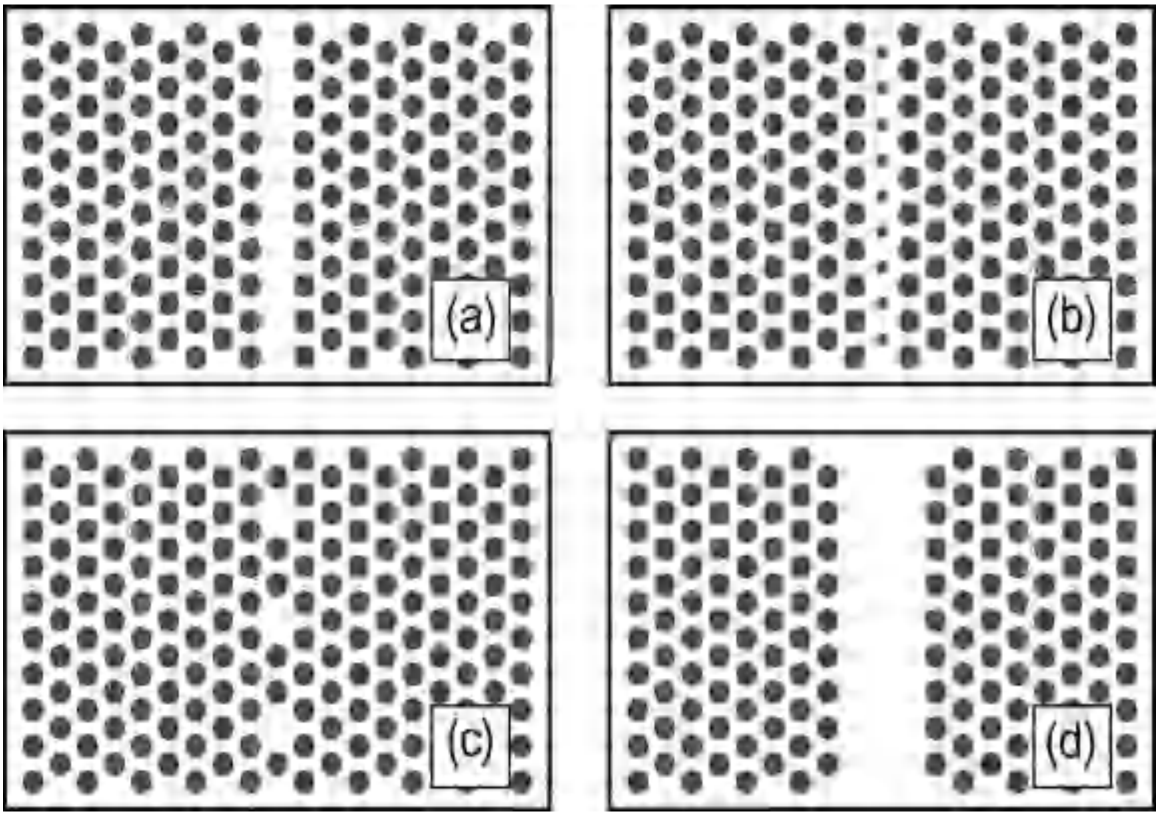

Figure I. 17. Photonic crystal linear defect with (a) absence of one row of holes in the middle of the structure (b) reducing a diameter of one row of holes (c) a series of interconnected cavities (d) removing three row of holes [36].

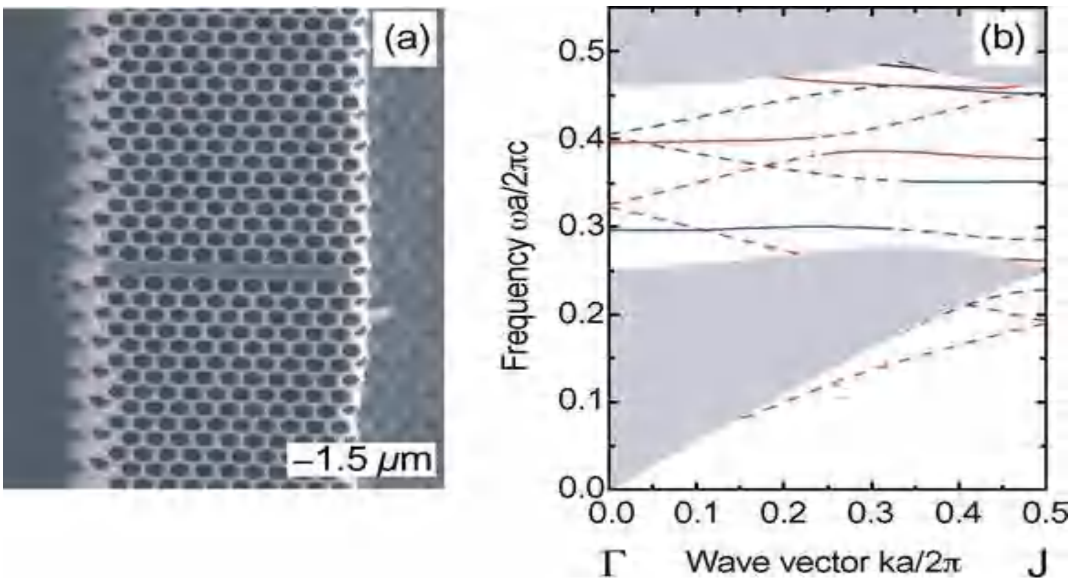

Figure I. 18. (a) SEM image of W1 waveguide in a 2D PhC of hexagonal lattice of air holes in silicon background (b) The TE bandgap is situated within the frequency range of 0.275 to 0.460, wherein multiple defect states are present [36].

A primary characteristic of photonic crystal waveguides is their strong lateral confinement. In the series of defects Wn, the number of modes will be minimal for n=1. Other defects allow reducing the number of modes in the band gap. However, they are based either on a local modification of the crystal topology or on a type of defect that plays on reducing the size of the air motifs [37]. Based on these properties, many functions can be envisaged: wavelength filtering, selective coupling, multiplexing, and Mach-Zehnder interferometers, all integrated into very small optical systems. Various research teams have proposed such components [38–41].

6. Photonic Crystal Applications

PhCs structures are very promising for the realization of integrated optical circuits. They benefit from significant technological advances made by the microelectronics industry, which make it possible to configure materials on nanometric scales, opening the way to integration in traditional CMOS circuits. Based on strong index contrasts, these structures allow confining light in volumes of the order of the wavelength. Thus, passive components such as couplers have been implemented in dielectric guides with reduced distances. Nevertheless, their property of strong confinement favoring the interactions light-matter interactions allows them to design and produce more and more efficient active components.

The application of resonant cavities and PhCs waveguides as building blocks for integrated photonic circuits has been the subject of significant research over the last decade. Based on these components, various devices have been proposed and demonstrated in several fields ranging from optics, optoelectronics, and telecommunications to biosensing. Owing to their properties of allowing the transmission of a very narrow band of frequencies, this effect offers numerous applications in optical communication systems such as resonators [42] and antennas [43]. Cavities with high-quality factors and low volume are of great interest, especially for controlling spontaneous light emission and realizing photon sources [44]. Moreover, their coupling with waveguides allows realizing a crucial function in integrated optics: Wavelength Division Multiplexing (WDM) [45]. On the other hand, their high optical confinement properties make them of great interest for sensing and biosensing applications, thus offering new perspectives for designing ultra-compact photonic sensors and biosensors [46,47]. Furthermore, several challenges remain unresolved, encompassing both performance and integration, before the commercial availability of this type of nanotechnology.

7. Conclusion

In this chapter, we have exhibited the basic notions and concepts associated with photonic crystals. Among these concepts, we have seen that the propagation of waves through these materials could lead to the creation of band gaps; the frequency ranges for which no wave will propagate in the photonic crystal. We have also demonstrated various defects that can occur in these artificial materials. Additionally, we have shown that depending on the geometrical parameters of these materials, it was possible to control the propagation of the optic waves within structures made of photonic crystals. Such effects make these structures very promising for the realization of compact and original optical components. It opens the way to integration in traditional CMOS circuits, particularly in the detection domain.

References

[1] I. Alvarado, Fabrication of two-dimensional photonic crystal single-defect cavities and their characterization by elastic scattering, University of California, Los Angeles, 2003.

[2] H. Altug, Physics and applications of photonic crystal nanocavities, PhD Thesis, Citeseer, 2007.

[3] Lord Rayleigh, XXVI. *On the remarkable phenomenon of crystalline reflexion described by* Prof. Stokes, The London, Edinburgh, and Dublin Philosophical Magazine and Journal of Science. 26 (1888) 256–265. https://doi.org/10.1080/14786448808628259.

[4] E. Yablonovitch, Inhibited Spontaneous Emission in Solid-State Physics and Electronics, Phys. Rev. Lett. 58 (1987) 2059–2062. https://doi.org/10.1103/PhysRevLett.58.2059.

[5] S. John, Strong localization of photons in certain disordered dielectric superlattices, Physical Review Letters. 58 (1987) 2486.

[6] E. Yablonovitch, T.J. Gmitter, K.-M. Leung, Photonic band structure: The face-centered-cubic case employing nonspherical atoms, Physical Review Letters. 67 (1991) 2295.

[7] K. Liu, L. Shen, S. He, One-way edge mode in a gyromagnetic photonic crystal slab, Optics Letters. 37 (2012) 4110–4112.

[8] C. Fenzl, T. Hirsch, O.S. Wolfbeis, Photonic Crystals for Chemical Sensing and Biosensing, Angew. Chem. Int. Ed. 53 (2014) 3318–3335. https://doi.org/10.1002/anie.201307828.

[9] A.W. Eckert, The World of Opals, John Wiley & Sons, 1997.

[10] S. Berthier, E. Charron, J. Boulenguez, Morphological structure and optical properties of the wings of Morphidae, Insect Science. 13 (2006) 145–158. https://doi.org/10.1111/j.1744-7917.2006.00077.x.

[11] A.R. Parker, R.C. McPhedran, D.R. McKenzie, L.C. Botten, N.-A.P. Nicorovici, Aphrodite's iridescence, Nature. 409 (2001) 36–37.

[12] J. Zi, X. Yu, Y. Li, X. Hu, C. Xu, X. Wang, X. Liu, R. Fu, Coloration strategies in peacock feathers, Proceedings of the National Academy of Sciences. 100 (2003) 12576–12578.

[13] S. Kinoshita, S. Yoshioka, J. Miyazaki, Physics of structural colors, Reports on Progress in Physics. 71 (2008) 076401.

[14] Unknown, Science Periodicals : Natural Opals, Science Periodicals. (2014). http://nanotechletter.blogspot.com/2014/04/natural-opals.html (accessed April 24, 2023).

[15] J.N. Winn, Y. Fink, S. Fan, J.D. Joannopoulos, Omnidirectional reflection from a one-dimensional photonic crystal, Opt. Lett., OL. 23 (1998) 1573–1575. https://doi.org/10.1364/OL.23.001573.

[16] H. Shen, Z. Wang, Y. Wu, B. Yang, One-dimensional photonic crystals: fabrication, responsiveness and emerging applications in 3D construction, RSC Adv. 6 (2016) 4505–4520. https://doi.org/10.1039/C5RA21373H.

[17] C. Blin, Développement de cristaux photoniques en diamant : modélisation, technologie et application à la biodétection, thesis, Paris 6, 2015. http://www.theses.fr/2015PA066020 (accessed April 25, 2023).

[18] J.D. Joannopoulos, Photonic Crystals: Molding the Flow of Light (Second Edition), Princeton University Press, 2008.

[19] B. Wild, ed., Étude expérimentale des propriétés optiques des cristaux photoniques bidimensionnels et de leur accordabillité, EPFL, Lausanne, 2006. https://doi.org/10.5075/epfl-thesis-3573.

[20] M. Plihal, A.A. Maradudin, Photonic band structure of two-dimensional systems: The triangular lattice, Phys. Rev. B. 44 (1991) 8565–8571. https://doi.org/10.1103/PhysRevB.44.8565.

[21] P.R. Villeneuve, M. Piche´, Photonic band gaps in two-dimensional square and hexagonal lattices, Phys. Rev. B. 46 (1992) 4969–4972. https://doi.org/10.1103/PhysRevB.46.4969.

[22] Y. Akahane, T. Asano, B.-S. Song, S. Noda, High-Q photonic nanocavity in a two-dimensional photonic crystal, Nature. 425 (2003) 944–947. https://doi.org/10.1038/nature02063.

[23] M. Thitsa, S. Albin, Band gap tuning of macro-porous si photonic crystals by thermally grown SiO2 interfacial layer, ECS Transactions. 11 (2008) 1.

[24] E. Yablonovitch, T.J. Gmitter, K.M. Leung, Photonic band structure: The face-centered-cubic case employing nonspherical atoms, Phys. Rev. Lett. 67 (1991) 2295–2298. https://doi.org/10.1103/PhysRevLett.67.2295.

[25] S.Y. Lin, J.G. Fleming, D.L. Hetherington, B.K. Smith, R. Biswas, K.M. Ho, M.M. Sigalas, W. Zubrzycki, S.R. Kurtz, J. Bur, A three-dimensional photonic crystal operating at infrared wavelengths, Nature. 394 (1998) 251–253. https://doi.org/10.1038/28343.

[26] K.M. Ho, C.T. Chan, C.M. Soukoulis, R. Biswas, M. Sigalas, Photonic band gaps in three dimensions: New layer-by-layer periodic structures, Solid State Communications. 89 (1994) 413–416. https://doi.org/10.1016/0038-1098(94)90202-X.

[27] H.S. Sözüer, J.P. Dowling, Photonic Band Calculations for Woodpile Structures, Journal of Modern Optics. 41 (1994) 231–239. https://doi.org/10.1080/09500349414550291.

[28] S.-Y. Lin, J.G. Fleming, A Three-Dimensional Optical Photonic Crystal, J. Lightwave Technol., JLT. 17 (1999) 1944.

[29] Y.A. Vlasov, X.-Z. Bo, J.C. Sturm, D.J. Norris, On-chip natural assembly of silicon photonic bandgap crystals, Nature. 414 (2001) 289–293.

[30] J.D. Joannopoulos, S.G. Johnson, J.N. Winn, R.D. Meade, Photonic Crystals: Molding the Flow of Light, 2nd ed., Princeton University Press, 2007. http://gen.lib.rus.ec/book/index.php?md5=B4E6BC3E593D9694F4C9C9313D988956 (accessed April 29, 2023).

[31] R. Dey, Optical Power Splitting Techniques Using Photonic Crystal Line Defect Waveguides, Electronic Thesis and Dissertation Repository. (2011). https://ir.lib.uwo.ca/etd/192.

[32] O. Painter, R.K. Lee, A. Scherer, A. Yariv, J.D. O'brien, P.D. Dapkus, I. Kim, Two-dimensional photonic band-gap defect mode laser, Science. 284 (1999) 1819–1821.

[33] D.F. Dorfner, T. Hürlimann, T. Zabel, L.H. Frandsen, G. Abstreiter, J.J. Finley, Silicon photonic crystal nanostructures for refractive index sensing, Applied Physics Letters. 93 (2008) 181103. https://doi.org/10.1063/1.3009203.

[34] K. Ashida, M. Okano, M. Ohtsuka, M. Seki, N. Yokoyama, K. Koshino, M. Mori, T. Asano, S. Noda, Y. Takahashi, Ultrahigh-Q photonic crystal nanocavities fabricated by CMOS process technologies, Opt. Express, OE. 25 (2017) 18165–18174. https://doi.org/10.1364/OE.25.018165.

[35] S. Robinson, R. Nakkeeran, Photonic crystal ring resonator-based add drop filters: a review, OE. 52 (2013) 060901. https://doi.org/10.1117/1.OE.52.6.060901.

[36] C. Jamois, R.B. Wehrspohn, L.C. Andreani, C. Hermann, O. Hess, U. Gösele, Silicon-based two-dimensional photonic crystal waveguides, Photonics and Nanostructures - Fundamentals and Applications. 1 (2003) 1–13. https://doi.org/10.1016/j.photonics.2003.10.001.

[37] Y. Desières, Conception et études optiques de composants micro-photoniques sur matériaux III-V à base de structures à bande interdite de photon, PhD Thesis, Lyon, INSA, 2001.

[38] K. Heydarian, A. Nosratpour, M. Razaghi, Design and analysis of an all-optical NAND logic gate using a photonic crystal semiconductor optical amplifier based on the Mach–Zehnder interferometer structure, Photonics and Nanostructures - Fundamentals and Applications. 49 (2022) 100992. https://doi.org/10.1016/j.photonics.2022.100992.

[39] F. Parandin, A. Sheykhian, Design and simulation of a 2 × 1 All-Optical multiplexer based on photonic crystals, Optics & Laser Technology. 151 (2022) 108021. https://doi.org/10.1016/j.optlastec.2022.108021.

[40] M.J. Maleki, M. Soroosh, An ultra-fast all-optical 2-to-1 digital multiplexer based on photonic crystal ring resonators, Opt Quant Electron. 54 (2022) 397. https://doi.org/10.1007/s11082-022-03781-x.

[41] M. Hosseinzadeh Sani, A. Ghanbari, H. Saghaei, An ultra-narrowband all-optical filter based on the resonant cavities in rod-based photonic crystal microstructure, Opt Quant Electron. 52 (2020) 295. https://doi.org/10.1007/s11082-020-02418-1.

[42] U. Biswas, J.K. Rakshit, G.K. Bharti, Design of photonic crystal microring resonator based all-optical refractive-index sensor for analyzing different milk constituents, Opt Quant Electron. 52 (2019) 19. https://doi.org/10.1007/s11082-019-2140-1.

[43] R.K. Kushwaha, P. Karuppanan, L.D. Malviya, Design and analysis of novel microstrip patch antenna on photonic crystal in THz, Physica B: Condensed Matter. 545 (2018) 107–112. https://doi.org/10.1016/j.physb.2018.05.045.

[44] M. Meier, A. Mekis, A. Dodabalapur, A. Timko, R.E. Slusher, J.D. Joannopoulos, O. Nalamasu, Laser action from two-dimensional distributed feedback in photonic crystals, Applied Physics Letters. 74 (1999) 7–9.

[45] An integrated device for electro-optic modulation and dense wavelength division multiplexing based on photonic crystals - ScienceDirect, (n.d.). https://www.sciencedirect.com/science/article/abs/pii/S0030402623001626 (accessed May 5, 2023).

[46] M. Al-Dossari, S.K. Awasthi, A.M. Mohamed, N.S. Abd El-Gawaad, W. Sabra, A.H. Aly, Bio-Alcohol Sensor Based on One-Dimensional Photonic Crystals for Detection of Organic Materials in Wastewater, Materials. 15 (2022) 4012. https://doi.org/10.3390/ma15114012.

[47] S.A. Taya, D.N. Alhamss, I. Colak, S.K. Patel, Sensitivity enhancement of an optical sensor based on a binary photonic crystal for the detection of Escherichia coli by controlling the central wavelength and the angle of incidence, Opt Quant Electron. 54 (2022) 127. https://doi.org/10.1007/s11082-022-03511-3.

Chapter II.

Photonic crystal for sensing applications.

1. Introduction

Lately, there has been a significant emphasis on examining optical sensors, partly due to their diverse applications in areas such as biomedical research, healthcare, environmental monitoring, and security. Optical sensing systems provide numerous advantages, including resistance to electromagnetic interference and the ability to perform remote sensing on a single chip. The utilization of CMOS-compatible silicon-on-insulator (SOI) and photonic crystal structures has substantially enhanced the sensing capabilities by advancing photonics, optics, and microfluidics technologies.

Nowadays, many studies have been conducted on photonic sensors to detect various physical, biological and chemical substances. Their detecting skills have been greatly improved by advances in photonics, including a better knowledge of physical phenomena and improvements in manufacturing techniques. Specifically, photonics has improved the ability to interact with light-analyte, miniaturize devices, and fluidic integration. High sensitivities have thus been achieved, for rapid response, with more uncomplicated handling and lower measurement costs.

For the goal of achieving the future commercialization of photonic sensors using lab-on-chip technology, the next-generation sensors must meet particular requirements. The devices must exhibit reliability, mobility, and compatibility with existing manufacturing methods. The utilization of lab-on-chip technology has great potential in creating integrated optical sensors on a chip. This enables simultaneous detection across flexible spectral ranges from visible to infrared. To further cut down manufacturing costs and enable swift, real-time measurements on a single detection chip, various structures based on integrated optics have been suggested. Notably, the use of photonic crystals in detection applications emerges as a promising solution due to their robust optical confinement properties in a compact volume. Their evolution has facilitated the design and development of highly efficient new photonic devices capable of detecting physical, chemical, and biological entities at a nanoscale level.

This chapter presents the main application related to this thesis work, which is optical sensing. We begin with some general notions about sensors, based on a non-exhaustive review of some examples of optical detection systems. Secondly, we present photonic crystal sensors, particularly PhCs sensors based on refractive index (RI) changes, as well as the conditions for using photonic crystals for detection applications.

2. Sensors : an overview

A *sensor* is a device that enables the measurement, characterization and quantification of physical quantities and converts them into easily interpretable signals, typically electrical, optical or acoustic.

A sensor is a transducer that delivers an exploitable physical signal in response to a physical quantity that is being measured (as depicted in Figure 1)[1]. External factors, or influencing quantities, can cause disturbances on the sensor, depending on their nature and magnitude. Some examples of these influencing quantities include temperature, pressure, humidity, chemical concentration, etc.
The sensor can capture and select a particular abstract quantity, known as information, from a set of possible events. This information is carried by a physical carrier, referred to as a signal, and it requires processing to be useful. Typically, a sensor comprises three main components: a sensing element, a transducer, and a control interface that bridges the signal and the user.

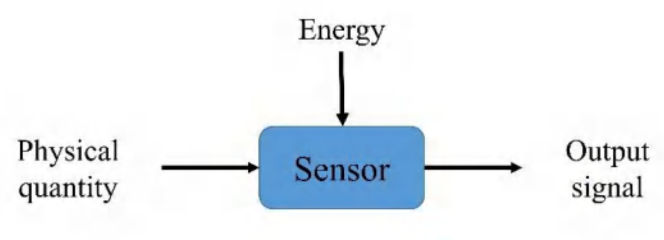

Figure II. 1. Schematic diagram of a sensor.

2.1. Biosensors

A biosensor is a sophisticated instrument designed to combine a biological element (such as enzymes, antibodies, or living cells) with a physicochemical transducer to selectively and sensitively detect, identify, and measure biological analytes [2]. This device generally comprises sensing components and a biosensitive or chemosensitive layer that explicitly detects the targeted biological entity in the sample. While the sensitive layer is responsible for identifying the specific analytes, the sensor must also be capable of converting this recognition into a physical, measurable signal. This conversion is achieved through a transducer; the various transduction methods employed allow biosensors to be classified based on the physical property utilized for molecular recognition. For example, biosensors can operate on changes in optical, electrical, magnetic or thermal properties. As part of this thesis work, optical transduction is our object of study.

2.2. Optical Biosensors

Optical biosensors represent a novel technology leveraging optical methods for the detection of chemicals and biological species. These sensors utilize light as the transducing element to gauge and analyze diverse parameters, relying on the interaction between the substances and light.

The community has shown much interest in the technology developed in numerous laboratories worldwide to improve detection performance further. A transduction method must not only enable the recognition of the molecule but also provide information on its quality and quantity in the analyte. The main advantage of optical detection compared to other techniques is that the optical field is non-invasive and does not harm the target molecules located on the surface of the sensor. Additionally, optical biosensors, which utilize light absorption, fluorescence and refractive index, are robust alternatives to conventional analytical techniques (Figure. 2). These devices offer rapid, ultra-sensitive, real-time, high-frequency monitoring capabilities, such as sample concentration or pre-treatment, without time-consuming steps.

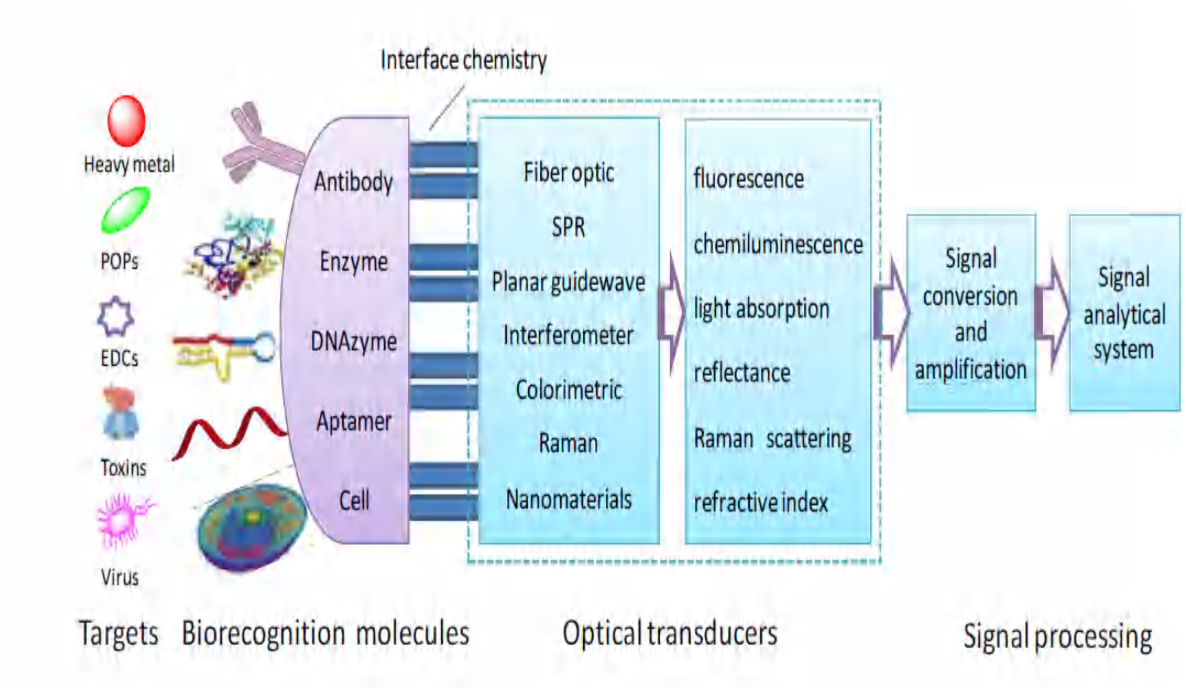

Figure II. 2. Block diagram of an optical biosensor [3].

2.3. Optical Biosensor Characteristics

When selecting a biosensor to sense the desired physical or chemical parameters, several factors must be considered [4,5]. The following functional parameters are typically used to evaluate a biosensor's performance: sensitivity, resolution, detection limit and selectivity.

2.3.1. Sensitivity

This corresponds to the variation of the measured signal in response to a change in the physical quantity induced at the surface of the sensor. The refractive index sensitivity (S) can be calculated numerically using the following formula:

$$S = \Delta\lambda / \Delta n \qquad \text{(II.1)}$$

It is expressed in units of nanometers per refractive index (nm/RIU).

2.3.2. Resolution

The minimum variation of the value of a physical quantity that a sensor can detect is known as its resolution, which corresponds to the slightest spectral shift that the sensor can reliably measure. This parameter is crucial for achieving the highest accuracy level in detecting very small quantities.

2.3.3. Detection Limit

The detection limit (DL) of the device is the combination of the sensitivity (S) and sensor resolution (R), which the following equation provides.

$$DL = \frac{R}{S} \tag{II.2}$$

The DL indicates the lowest sample refractive index change that can be precisely measured for refractive index sensing [6].

2.3.4. Selectivity

The last parameter corresponds to the sensor's ability to measure only one substance in which it is used. It depends on the sensing medium of the sensor.

2.4. Types of Biodetection Processes For Optical Biosensors

A large group of optical biosensors can be distinguished using the transduction method. These various optical biosensors are categorized based on two detection protocols: label-based sensing and label-free sensing [7].

2.4.1. Label-based Sensing

This technique relies on indirect detection to identify the presence of the target molecule being analyzed. A label is usually attached to an antibody or molecule specifically targeting the molecule of interest. When the labeled molecule binds to the target, it generates a detectable signal, such as light or radiation, that can be measured, as shown in figure 3 (a). For example, in fluorescence detection, the fluorescent molecule can immediately emit a fluorescent signal after absorbing light energy (excitation light). The target molecules can be quantified owing to this fluorescence.

Fluorescence biosensors are highly sensitive, with low detection limits, and some sensing processes have already been commercialized [8]. This process makes it possible to consider multiparametric detection from a single analytical sample on the same platform. Nevertheless, they require additional steps to attach the label and can be more expensive. Furthermore, these devices are unsuitable for sensing applications that require rapid and real-time measurements.

2.4.2. Label-free Sensing

In recent years, label-free optical detection technologies have grown significantly due to their ability to analyze molecular interactions in their natural state directly [9] (Figure 3 (b)). A label-free process generally involves a transducer capable of directly measuring some physical characteristics of the chemical compound, molecule, virus or cell. This further simplifies the preparation protocols and allows a real-time study of the molecular interactions kinetics.

The detection principle relies on the change of a specific property of light as it interacts with the element of interest (molecule, virus or cell). Therefore, there are several detection methods available for this purpose, such as those that rely on changes in refractive index, absorbance properties, or nonlinearity effects. In this context, we will only concentrate on detection based on changes in refractive index.

Label-free sensors are simpler to use and more cost-effective. Thus, it is evident that transduction methods in label-free sensing are universal and applicable in a wide range of applications. Therefore, we will only focus on label-free optical sensors forward on.

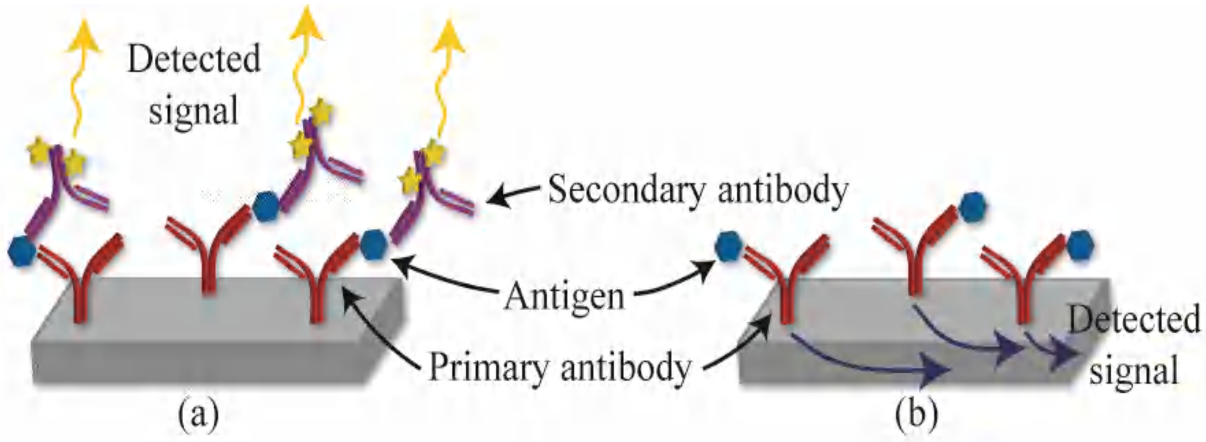

Figure II. 3. (a) Labeled (b) label-free biosensing processes [7].

3. An Overview: Optical Label-free Biosensors

The development of miniaturized, biocompatible optical sensors with real-time response and easy-to-use interfaces has recently become a significant commercial and technological challenge. This part provides an overview of various optical techniques utilized to design optical biosensors.

In this context, surface plasmon resonance (SPR), interferometric, and optical ring resonator sensors are some of the most popular optical techniques employed.

3.1. Surface Plasmon Resonance (SPR) Sensors

Surface plasmon resonance (SPR) technology is the most commonly utilized label-free sensing structure. The surface plasmon wave is a charge density oscillation at the interface between two materials with different dielectric constants, such as a metal (usually gold or silver) and a dielectric. In this case, the light is reflected at the interface of the prism and the metal, generating an evanescent wave in the metal layer, as illustrated in figure 4. Several configurations of SPR biosensors differ only in the method of exciting the surface plasmon wave, such as using prisms [10] or fiber optics [11].

The SPR technique is a highly effective method for monitoring changes in the refractive index (RI) in the immediate proximity of a metal surface. When molecules adsorb onto the metal surface and cause a change in the RI, the resonance spectral response of the SPR will also change, resulting in a shift in the angular or spectral position of the SPR dip. This shift can be used to gain insight into the properties of the system and obtain information about the kinetics of the adsorbed molecules on the surface.

SPR sensors exhibit high sensitivity, with refractive index unit (RIU) sensitivity as large as 10^3 nm/RIU, according to [12]. However, due to strong absorption in the metal film, the SPR resonance mode is broad, resulting in a low quality (Q) factor. This lowers their detection limit (DL) and makes them unsuitable for applications that require the detection of very small molecules.

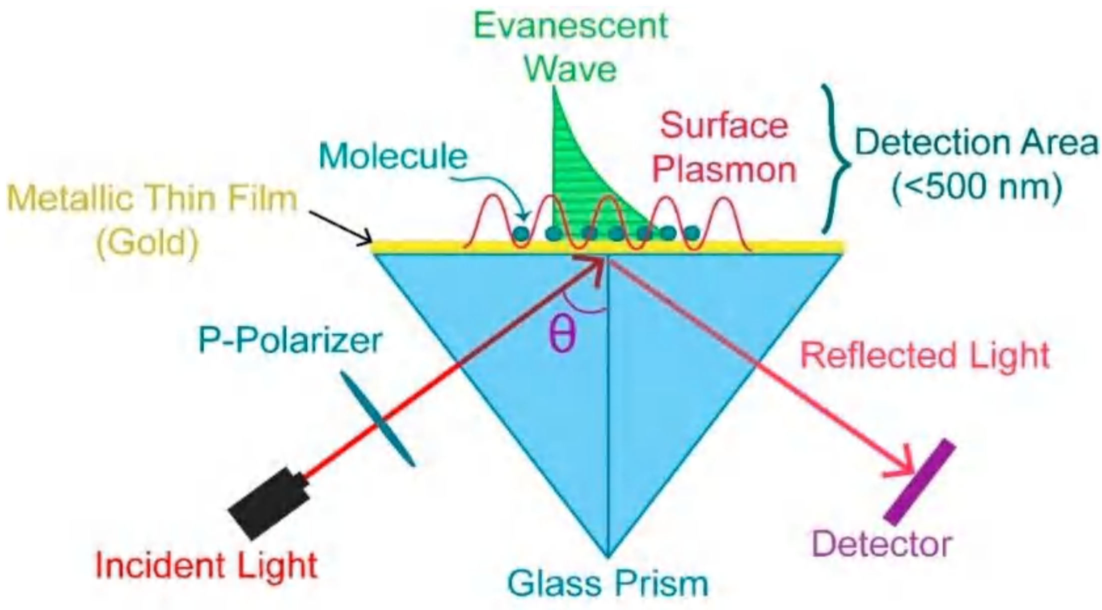

Figure II. 4. Surface plasmon resonance technique [13].

3.2. Interferometric Sensors

Interferometer sensors are used to measure changes in optical path length that result from variations in the local refractive index. Mach-Zehnder (MZ) and Young's (Y) interferometers are two common types of configurations, as shown in Figure 4 [14,15].

These sensors usually contain a reference arm and a sensing arm. A laser source produces coherent light with a single frequency and polarization that is split equally at the Y-junction, and then directed into the input waveguide. The sensing arm has a window that allows the evanescent field of that branch to interact with the analyte, while the reference arm is kept isolated from the sample. For IMZ, the light from both arms recombines and produces interference at the output waveguide. A photodetector is used to measure the intensity of the light. As the analyte binds to the sensing arm, it modifies the local refractive index (RI) and changes the optical path length within that branch. This alteration in path length causes a shift in the interference pattern, thereby changing the amount of light intensity detected by the photodetector.

In the case of Young's interferometer, the signals from both arms are projected onto a CCD camera to form interference fringes, as shown in figure 4 (b), whose displacement can be linked to the phase delay.

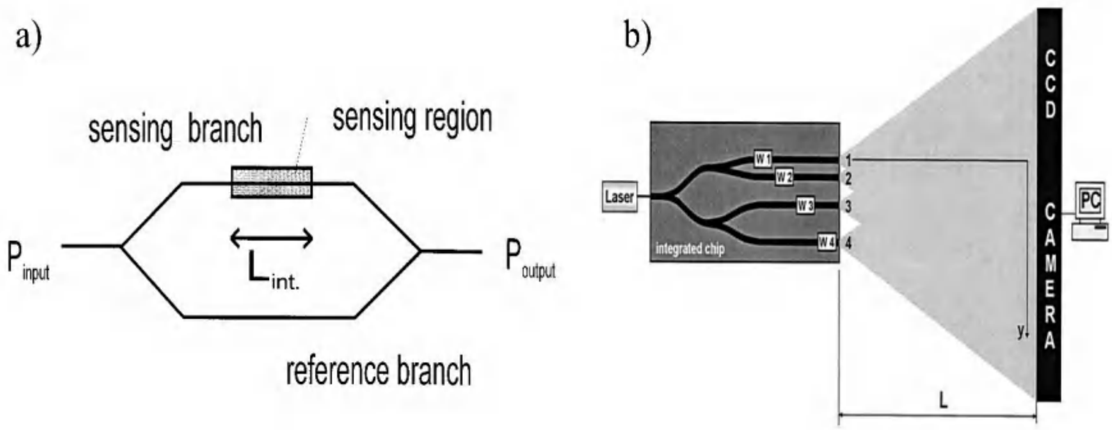

Figure II. 5. Schematic representation (a) Mach-Zehnder interferometer sensor [15] (b) Young interferometer sensor [14].

Over the past few years, several configurations of the Young interferometer have been designed [16], and it has been shown that it is possible to obtain a detection limit of 10^{-7} RIU [14]. This value is of the same order of magnitude as the best performances obtained with IMZ sensors [17], which is expected due to their similar architecture. However, the major disadvantage of this type of sensor remains its response type. Having a sinusoidal response (phase measurement) and being non-linear like other optical sensors, the variation of the latter is much weaker at the maxima of the curve, which automatically leads to a decrease in the sensor's sensitivity.

3.3. Ring Resonator Sensor

Their operating principle is based on confining light through a series of total internal reflections within the cavity (Figure 6) [18]. In this case, detection is due to the interaction between the electromagnetic field propagating in this cavity and the molecules present on the surface.
The circular configuration allows the propagation of modes known as "whispering gallery mode". Unlike previous cases, in this type of device, the length of the interaction between light and molecules is no longer directly related to the total physical length of the sensor, but to the number of light revolutions in the resonator. Therefore, the effective interaction of light with target analytes will be related to the quality factor (Q) of the cavity. Hence, high-Q resonators are desired. High-Q factors imply higher interaction times with molecules in the detection region. Therefore, these strong quality factor (Q) properties and the geometry used allow low limits of detection to be achieved.
Due to their low index contrast, ring resonators have significantly lower sensitivity than plasmonic detectors. Theoretically, these devices, made of dielectric materials, should have very low optical losses. It has been demonstrated to be accurate in the case of scattering-related losses. Nonetheless, losses resulting from emissions caused by the curved shape of the resonators have been observed and remain significantly high.

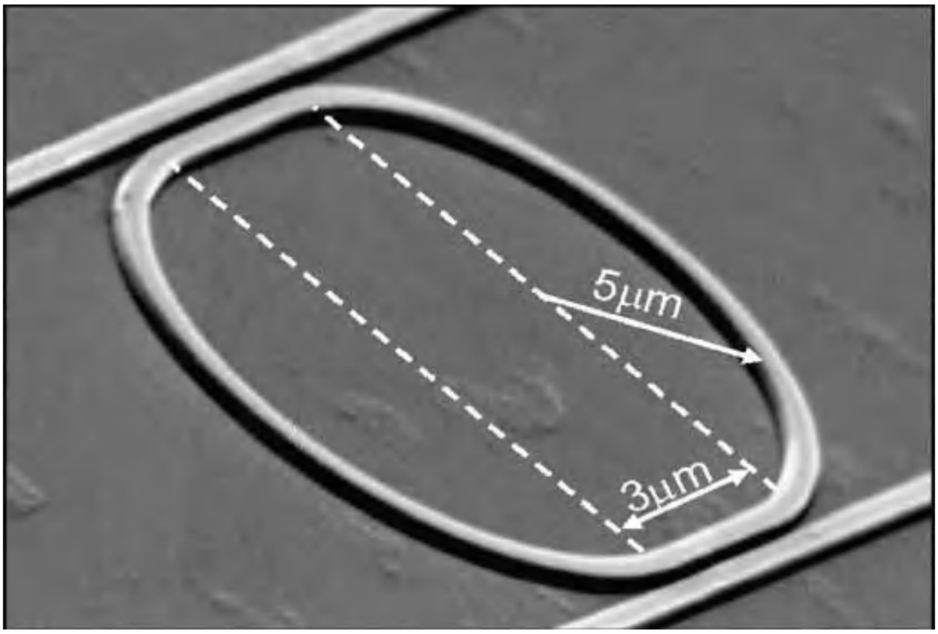

Figure II. 6. Silicon ring resonator [18].

4. Sensors Based Photonic Crystal

Photonic crystals are composed of periodic dielectric structures. The main characteristic of this periodicity is the creation of a range of frequencies that cannot propagate through the structure, termed the photonic bandgap (PBG). The size and position of the PBG in the spectrum can be adjusted by varying the refractive index contrast of the dielectric materials and/or the periodicity of the structure. These properties make photonic crystals extremely useful in various applications.

In particular, due to their ability to trap photons and create optical resonances that are highly sensitive to the presence of biological analytes, the use of photonic crystals as biosensors has generated significant interest. Photonic crystals have a wide detection range, making them applicable in a broad range of measurements extending from air to highly viscous biological fluids.

Integrated biosensors based on photonic crystals are one of the most exciting and interesting optical sensors currently being made. Advances in developing photonic crystal transducers, both in understanding physical phenomena and mastering fabrication processes, have significantly improved their detection capabilities, particularly in light-matter interactions, interface miniaturization and integration with microfluidic systems. This has led to better sensitivities and detection limits, shorter detection times, more uncomplicated handling and lower per-measurement costs.

4.1. Photonic Crystal Sensor Domain

The use of PhC sensing technology is causing a revolution in the world of nanochip sensors. These sensors are known as transducers, as they convert signals from one energy domain to another domain of interest [1,19]. These domains include electrical (Voltage, current, and electric field), mechanical (Force, pressure, stress, strain, and speed), chemical (Glucose, protein, pH, DNA, and blood sample), radiation (Radiation, absorption, and transmission), magnetic (Magnetic field) and thermal (Temperature) domains. PhC-based sensors are capable of accurately detecting all six domains. Figure 7 illustrates the different PhC sensing domains [20]. In general, a light signal passes through a sensing sample, and the resulting output is observed by detecting the center peak wavelength shifted towards a higher wavelength.

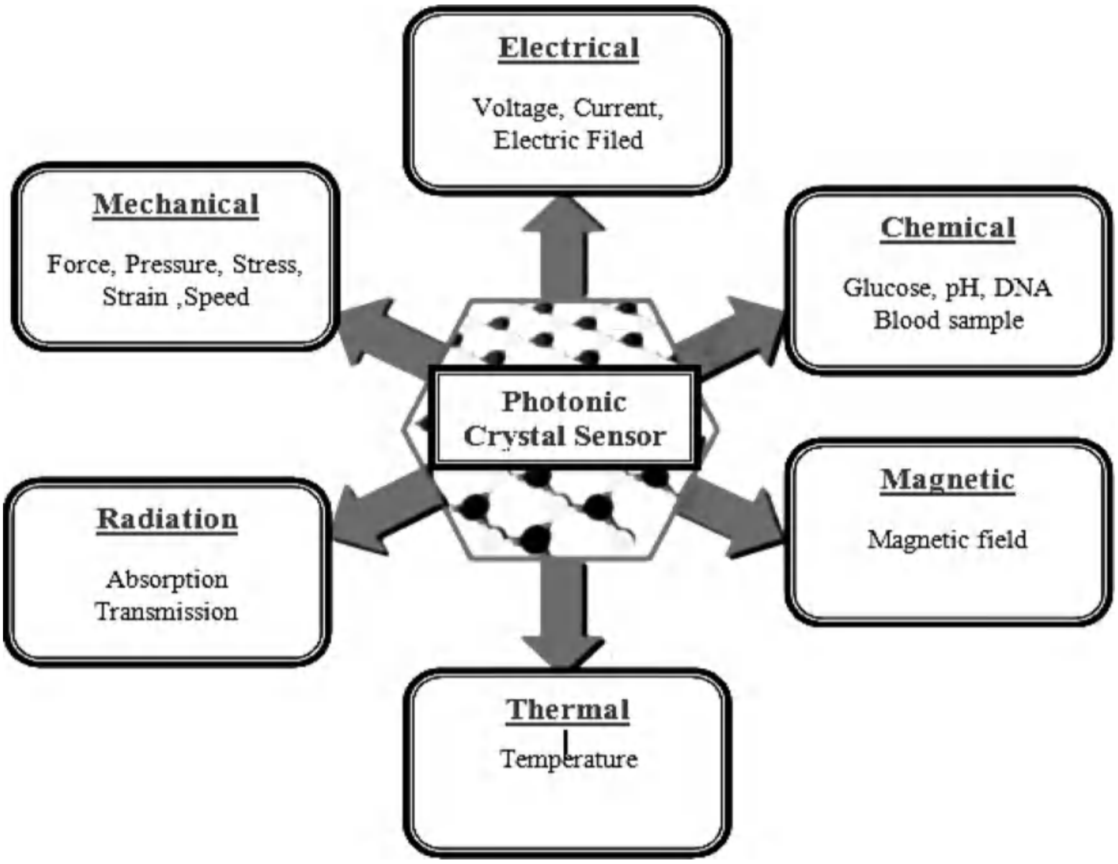

Figure II. 7. Different domains of PhCs sensing [20].

4.2. PhC Sensors Based On Refractive Index (RI) Variation

Refractive index change is utilized for detection in several advanced designs (including integrated waveguides and microcavities). The most widespread class of sensors is photonic crystal sensors, which are based on changes in refractive index. This sensor category has various advantages, such as label-free fluorescence detection, real-time detection, and high sensitivity.

The mechanism of such detection consists of measuring the refractive index variation of a sensing element as a function of the presence of an analyte (a substance to be detected). Detection is performed by a sensitive area that reacts with the analyte. The detection zone comprises a photonic structure operating with a sensitive zone. The latter reacts with the analyte, which induces a refractive index variation, the thickness of the sensitive layer, and its absorption. The structure must be highly sensitive to the refractive index variation.

4.3. Types of Detecting Mechanisms in Photonic Crystal

Resonant wavelength shift and intensity variation are the two basic detection methods that can be used for sensor calibration.

4.3.1. Resonant Wavelength Shift Mechanism

The resonant wavelength shift method is utilized to detect the presence of a sample by measuring the change in resonant mode defect, as shown in Figure 8 (a). The refractive index (RI) of the sample undergoes a change, which causes a shift in the resonant wavelength of the optical sensor. Although higher quality factors can improve the accuracy of wavelength shift-based sensors, detecting even the smallest change in cavity, RI requires an exceptionally sensitive sensor.

4.3.2. Intensity Variation Mechanism

The second detection method involves identifying biological substances by monitoring the resonant frequency's intensity change. The intensity variation (IV) technique is used for this, as shown in Figure 8 (b).

A limited range of wavelength shifts can be determined, and a wider full width at half maximum (FWHM) is preferred for accurate measurements.

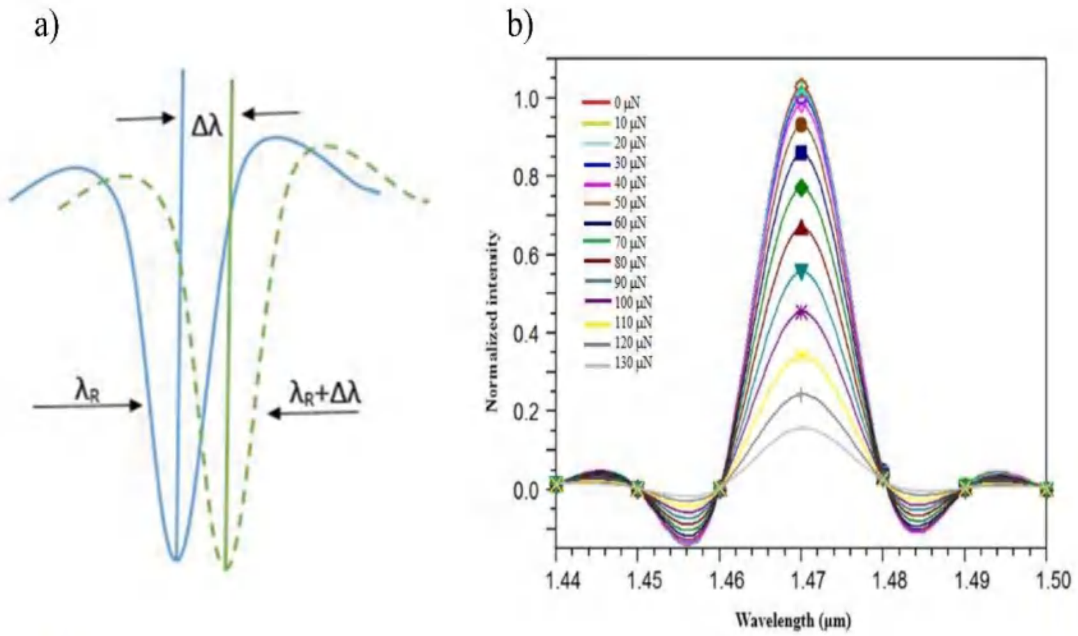

Figure II. 8. (a) Resonant wavelength shift scheme [21] (b) intensity variation scheme [22].

5. Photonic Crystal-based Sensor Design Platforms

Sensors can be designed using various photonic crystal platforms, such as photonic crystal-based waveguides, fibers, and ring resonators. The following section will present some examples of sensor-based photonic crystals.

5.1. Photonic Crystal Waveguide-based Sensing

The structures of photonic crystal waveguides (PhCW) are of great interest. In several PhC-based sensors that rely on refractive index changes, the PhC waveguide directly acts as the sensing element without needing an integrated microcavity. This type of sensor can detect small amounts of analyte and low-concentration samples, which can be an advantage compared to conventional approaches. The main key to the ability of optical biosensors to detect biological analytes is that biological molecules such as proteins, cells, and DNA all have a dielectric permittivity higher than that of air and water.

In 2015, Kumar *et al*. presented a novel gas and fluid detection design using a photonic crystal biperiodic waveguide based on the refractive index (RI) variation of supercavities [23]. The design was created by introducing a triangular array of air holes in a silicon (Si) substrate, as depicted in Figure 9. This structure consists of supercavities that selectively permit the resonant frequency to pass through the PhC waveguide while reflecting all other frequencies. As shown in Figure 10, the sensing principle relies on the displacement of the resonance mode of the supercavities when they are filled with a gas or fluid.

The designed device can function as a gas or fluid sensor by selectively filling the holes of the supercavities. The sensor exhibited a sensitivity of 610 nm/RIU for gas sensing. Furthermore, when used as a fluid sensor, the sensor had a sensitivity of 300 nm/RIU when the RI ranged from 1.0 to 1.5.

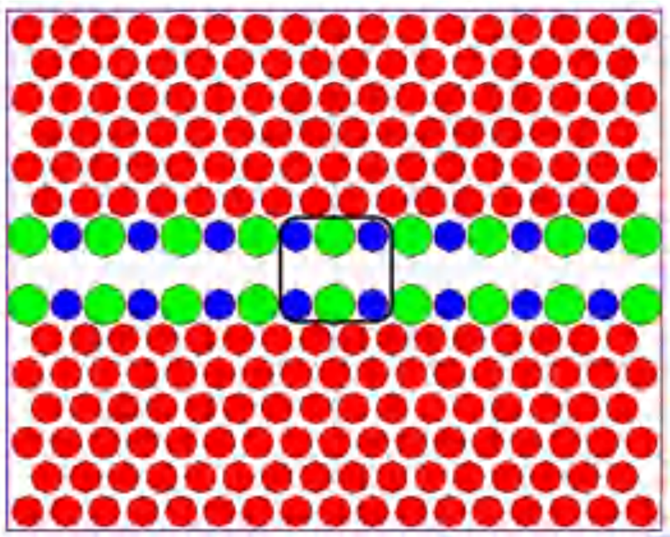

Figure II. 9. The layout of the 2D-PhC waveguide for RI and gas sensing containing supercavities [23].

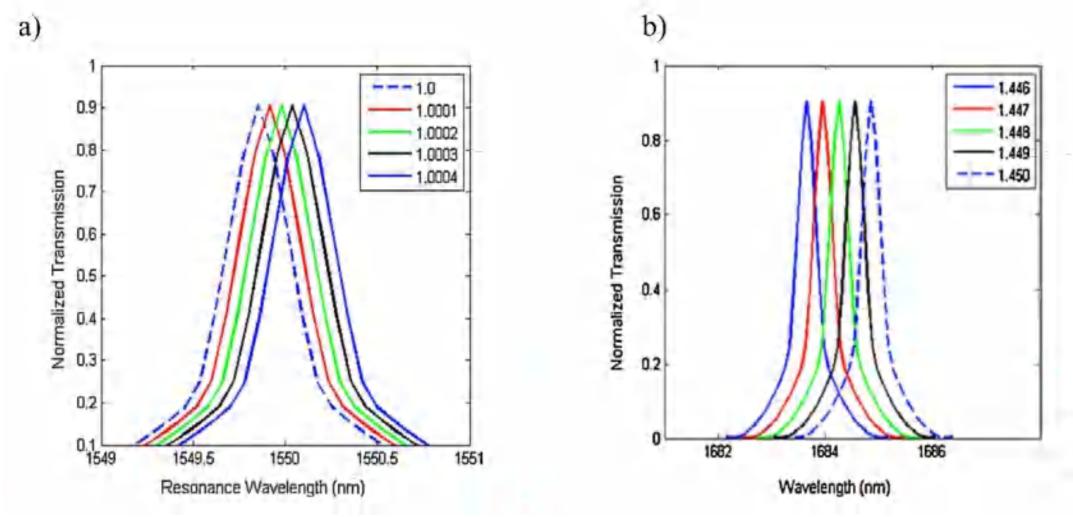

Figure II. 10. (a) Normalized transmission spectrum of the gas sensor with five various RI of supercavities. (b) Normalized transmission spectrum of the fluid sensor with five different RIs varying from n = 1.446 to n = 1.450.

Skivesen *et al.* suggested another optical waveguide-based biosensor utilizing a photonic crystal (PhC) to sense protein concentrations in 2007 (Figure 11 (a)) [24]. With an excellent signal-to-noise ratio, bovine serum albumin protein (BSA) in solution was detected at a concentration of 0.15 µMolar. These structures can be used for larger sample volumes due to their larger detection surfaces. The sensor detection method is based on changes to a waveguide's bandwidth caused by modifications in the refractive index (Figure 11 (b)) [24].

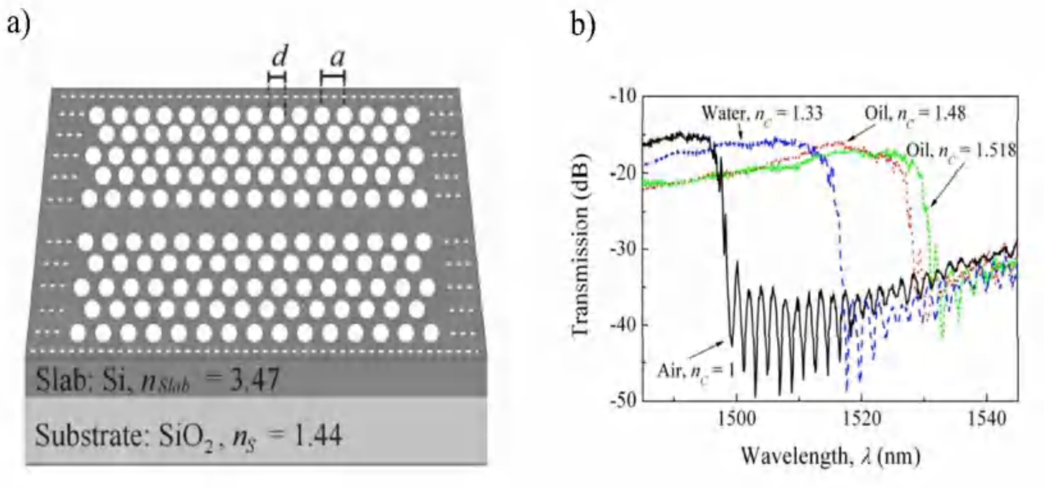

Figure II. 11. (a) Photonic crystal waveguide configuration on a SiO wafer; (b) Transmission spectrum from the fabricated waveguide based PhC for four different types of solutions.

5.2. Photonic Crystal Cavity-Based Sensing

The typical characteristics of PhC cavities, such as strong spatial and temporal confinement of light and a long photon lifetime [25], significantly increase the strength of the interaction between the optical field and the defect region material. The quality factor and resonance frequency of PhC cavities can be adjusted accurately, which offers a wide range of potential applications.

For sensing applications, the strong light-matter interaction effect produces an optical mode with a resonance wavelength that is extremely sensitive to local changes in the surroundings. Hence, PhCs cavities are a suitable building block for developing sensitive optical sensors among the extensive range of proposed designs [26].The ability to integrate them into "lab-on-chip" systems for immediate on-site detection is also provided by their effective detection area, which is approximately micrometers or nanometers in specific designs.

The slight variation in the refractive index change within the cavity causes a small shift in the frequency of the mode of interest, allowing the use of this property as a transduction mechanism and supporting the use of photonic crystals as optical sensors. The reference is the spectral position λ_0 of the cavity resonance. Thus, measuring the variation in spectral position $\Delta\lambda$ is equivalent to measuring the variation in refractive index change Δn associated with analyte recognition on the surface of the cavity. This principle is illustrated in Figure 12.

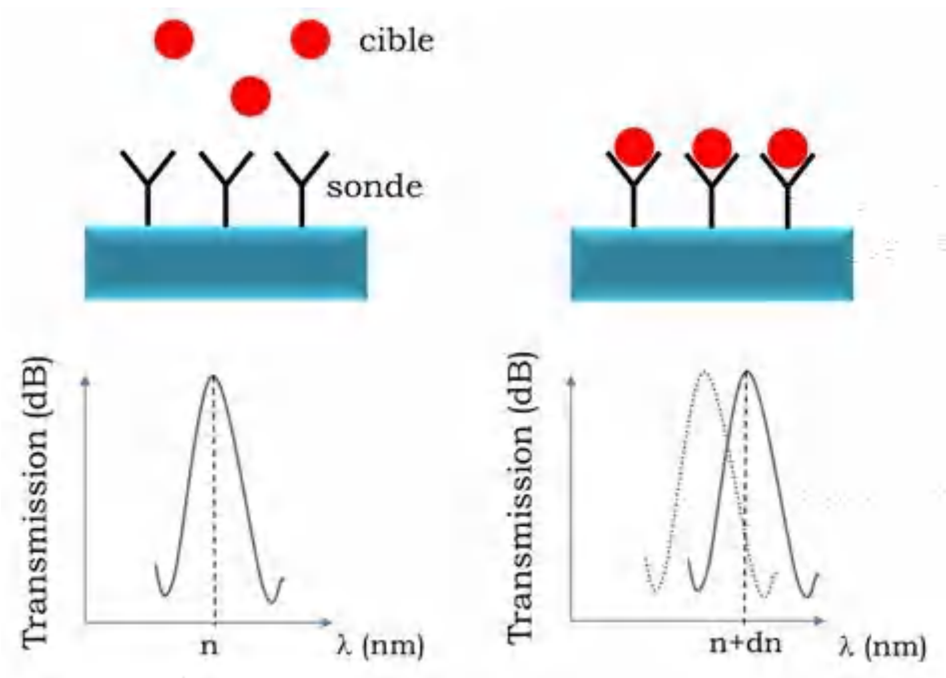

Figure II. 12. Mechanism of optical transduction measurement of a PhC cavity [27].

The desired detection should be highly selective and sensitive enough to sense very low analyte concentrations. Several designs and configurations based on PhCs cavities are continually created and improved to enhance detection performance further. Good biosensing designs are an essential effort that must be carefully handled to achieve the necessary detection properties. As a result, diverse sensor designs and configurations have been proposed and implemented employing various 1D-PhCs and 2D-PhCs cavity types, including linear cavities L_n [28], ring cavities [29], hexagonal cavities [30], and waveguide-coupled cavities [31].

In all of the examples, the simpler and more precise fabrication process, lower costs, better integration, and smaller footprint of 1D PhCs make them attractive for sensing applications [32].

Furthermore, coupled systems (waveguide-cavity) are preferred due to the difficulties in coupling and transferring light to single cavities or resonator systems. Coupled cavities integrated with PhCs waveguides provide a variety of advantages in terms of performance and compactness, and they are effortless to integrate into parallel and multiple detection systems.

Examples of such systems include those from Nagat A. Elmahdy *et al*. [33], who presented a theoretical study of a one-dimensional photonic crystal thermal sensor. The system consists of two mini PhCs $(air/Si)^3$ and $(Si/air)^3$ and a nematic liquid crystal material embedded between them as a defect layer, as depicted in figure 13. The suggested thermal sensor exhibits a high sensitivity of 0.328 nm/°C.

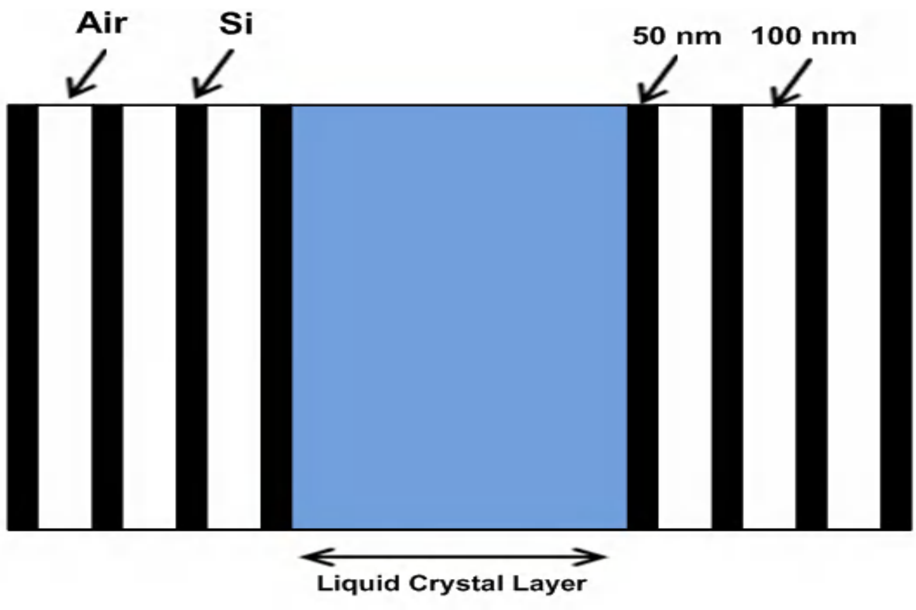

Figure II. 13. 1D photonic crystal containing a nematic liquid crystal defect.

In addition, Dorfner *et al*. presented a theoretical and experimental study of an SOI-based PhCs filter for detecting refractive index changes in fluids. The light is transmitted evanescently between two nanocavities (L3 and H1-r) inserted between two input and output waveguides (W1) (Figure .14). In terms of performance, the results obtained show that the (H1-r) nanocavity is the best, with a factor of 3000 and a sensitivity of 155 nm/RIU.

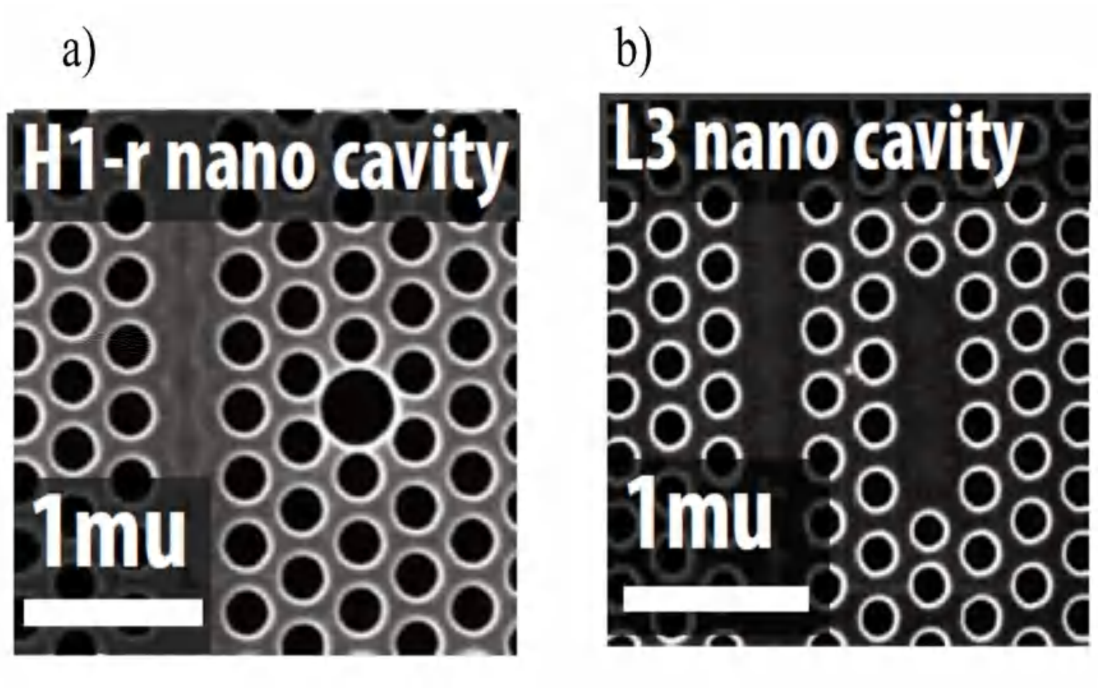

Figure II. 14. SEM images of cavities (a) H1-r (b) L3 near the photonic crystal waveguide.

6. Conclusion

This chapter discussed optical sensors and presented an overview of the main detecting methods. We were particularly interested in photonic crystal sensors because of their many optical characteristics, such as strong light confinement in small volumes. We also demonstrated the significant potential of waveguides and photonic crystal cavities. Photonic crystal cavities, particularly for lab-on-chip applications, are a promising platform for developing future small detection systems since they have the necessary size and confinement features. Instantaneous detection is now possible thanks to the enormous advancements made in this field over the past ten years. The challenge of the manufacturing and characterization of these materials still exists for the development of these applications. Systematic experimental research is time- and money-consuming due to this challenge. Hence, effective and quick theoretical and numerical modeling was required to save time and reduce the expense of tests. The fundamental description of the numerical methods employed in this thesis work, such as the transfer matrix method, the plane wave method, and the finite difference time domain method, will therefore be the only focus of the following chapter.

References

[1] G. Asch, Les capteurs en instrumentation industrielle, Dunod, 2010.

[2] B.R. Eggins, Biosensors: an Introduction, Wiley-Teubner, 1996.

[3] F. Long, A. Zhu, H. Shi, Recent advances in optical biosensors for environmental monitoring and early warning, Sensors. 13 (2013) 13928–13948.

[4] A. D'Amico, C. Di Natale, A contribution on some basic definitions of sensors properties, IEEE Sensors Journal. 1 (2001) 183–190.

[5] B.T. Cunningham, Label-free optical biosensors: An introduction, Label-Free Biosensors: Techniques and Applications. 1 (2009).

[6] I.M. White, X. Fan, On the performance quantification of resonant refractive index sensors, Optics Express. 16 (2008) 1020–1028.

[7] S. Mehrabani, A.J. Maker, A.M. Armani, Hybrid integrated label-free chemical and biological sensors, Sensors. 14 (2014) 5890–5928.

[8] S. Ray, P.J. Reddy, S. Choudhary, D. Raghu, S. Srivastava, Emerging nanoproteomics approaches for disease biomarker detection: A current perspective, Journal of Proteomics. 74 (2011) 2660–2681.

[9] H.K. Hunt, A.M. Armani, Label-free biological and chemical sensors, Nanoscale. 2 (2010) 1544–1559.

[10] A.P. Vinogradov, A.V. Dorofeenko, A.A. Pukhov, A.A. Lisyansky, Exciting surface plasmon polaritons in the Kretschmann configuration by a light beam, Phys. Rev. B. 97 (2018) 235407. https://doi.org/10.1103/PhysRevB.97.235407.

[11] A.K. Sharma, R. Jha, B.D. Gupta, Fiber-optic sensors based on surface plasmon resonance: a comprehensive review, IEEE Sensors Journal. 7 (2007) 1118–1129.

[12] P. Pfeifer, U. Aldinger, G. Schwotzer, S. Diekmann, P. Steinrücke, Real time sensing of specific molecular binding using surface plasmon resonance spectroscopy, Sensors and Actuators B: Chemical. 54 (1999) 166–175.

[13] F.B. Kamal Eddin, Y.W. Fen, The principle of nanomaterials based surface plasmon resonance biosensors and its potential for dopamine detection, Molecules. 25 (2020) 2769.

[14] A. Ymeti, J.S. Kanger, J. Greve, P.V. Lambeck, R. Wijn, R.G. Heideman, Realization of a multichannel integrated Young interferometer chemical sensor, Applied Optics. 42 (2003) 5649–5660.

[15] R.G. Heideman, P.V. Lambeck, Remote opto-chemical sensing with extreme sensitivity: design, fabrication and performance of a pigtailed integrated optical phase-modulated Mach–Zehnder interferometer system, Sensors and Actuators B: Chemical. 61 (1999) 100–127.

[16] T. Nagel, E. Ehrentreich-Förster, M. Singh, K. Schmitt, A. Brandenburg, A. Berka, F.F. Bier, Direct detection of tuberculosis infection in blood serum using three optical label-free approaches, Sensors and Actuators B: Chemical. 129 (2008) 934–940. https://doi.org/10.1016/j.snb.2007.10.009.

[17] R. Bernini, G. Testa, L. Zeni, P.M. Sarro, Integrated optofluidic Mach–Zehnder interferometer based on liquid core waveguides, Appl. Phys. Lett. 93 (2008) 011106. https://doi.org/10.1063/1.2957031.

[18] K. De Vos, I. Bartolozzi, E. Schacht, P. Bienstman, R. Baets, Silicon-on-Insulator microring resonator for sensitive and label-free biosensing, Optics Express. 15 (2007) 7610–7615.

[19] Read “Expanding the Vision of Sensor Materials” at NAP.edu, n.d. https://doi.org/10.17226/4782.

[20] N. Kumar, B. Suthar, Advances in Photonic Crystals and Devices, CRC Press LLC, 2019.

[21] S. Olyaee, H. Mohsenirad, A. Mohebzadeh-Bahabady, W. Wang, Photonic crystal chemical/biochemical sensors, Progresses in Chemical Sensor. (2016) 3.

[22] T. Suganya, S. Robinson, Design of 2D photonic crystal based force sensor using paralleloid ring resonator, Journal on Microelectronics. 3 (2017).

[23] A. Kumar, T.S. Saini, R.K. Sinha, Design and analysis of photonic crystal biperiodic waveguide structure based optofluidic-gas sensor, Optik. 126 (2015) 5172–5175. https://doi.org/10.1016/j.ijleo.2015.09.157.

[24] N. Skivesen, A. Têtu, M. Kristensen, J. Kjems, L.H. Frandsen, P.I. Borel, Photonic-crystal waveguide biosensor, Optics Express. 15 (2007) 3169–3176.

[25] P. Lalanne, C. Sauvan, J.P. Hugonin, Photon confinement in photonic crystal nanocavities, Laser & Photon. Rev. 2 (2008) 514–526. https://doi.org/10.1002/lpor.200810018.

[26] S. Chakravarty, A. Hosseini, X. Xu, L. Zhu, Y. Zou, R.T. Chen, Analysis of ultra-high sensitivity configuration in chip-integrated photonic crystal microcavity bio-sensors, Appl. Phys. Lett. 104 (2014) 191109. https://doi.org/10.1063/1.4875903.

[27] C. Blin, Développement de cristaux photoniques en diamant: modélisation, technologie et application à la biodétection, PhD Thesis, Paris 6, 2015.

[28] Y. Liu, H.W.M. Salemink, Photonic crystal-based all-optical on-chip sensor, Optics Express. 20 (2012) 19912–19920.

[29] S. Olyaee, A. Mohebzadeh-Bahabady, Designing a novel photonic crystal nano-ring resonator for biosensor application, Opt Quant Electron. 47 (2015) 1881–1888. https://doi.org/10.1007/s11082-014-0053-6.

[30] E. Chow, A. Grot, L.W. Mirkarimi, M. Sigalas, G. Girolami, Ultracompact biochemical sensor built with two-dimensional photonic crystal microcavity, Optics Letters. 29 (2004) 1093–1095.

[31] X. Wang, Q. Tan, C. Yang, N. Lu, G. Jin, Photonic crystal refractive index sensing based on sandwich structure, Optik. 123 (2012) 2113–2115. https://doi.org/10.1016/j.ijleo.2011.10.008.

[32] M.G. Abdul Rahman, 1D photonic crystal nanocavities for optical sensing, PhD, University of Glasgow, 2017. https://eleanor.lib.gla.ac.uk/record=b3273870 (accessed April 11, 2023).

[33] N.A. Elmahdy, M.S. Esmail, M.M. El-Okr, Characterization of a thermal sensor based on one-dimensional photonic crystal with central liquid crystal defect, Optik. 170 (2018) 444–451. https://doi.org/10.1016/j.ijleo.2018.05.117.

Chapter III.

Methods and tools for numerical simulations.

1. Introduction

The need for numerical computations is crucial, especially considering the significant costs involved in producing structured objects at the nanoscale. Therefore, when designing a component, it is essential to rely on numerical computations instead of the expensive production of numerous samples. However, numerical analysis is highly complex, involving computations for the diffraction and propagation of electromagnetic fields in intricate geometric structures. These structures are composed of materials with substantial differences in refractive indices, and the analysis must also account for elements both significantly larger and smaller than the wavelength. The algorithm for numerical computing must have the capability to accurately and swiftly represent all these intricate structures.

During the last decades, numerous methods have been developed to model the phenomena of electromagnetic wave propagation and diffraction. However, their limitations became apparent as they required additional processing resources, creating more opportunities for analytical investigations. In recent times, academics have shown a growing interest in computational approaches due to advancements in computer technology and the expanded capabilities of calculators. Numerical methods have evolved, and new ones have been devised, enabling the handling of problems with intricate geometries.

Using these tools to characterize photonic crystals, the effects of imperfections and manufacturing defects can be accurately predicted. Based on the resolution of the Maxwell equations, these methods are numerous, varied and classified according to the domain in which they operate, frequency or temporal. For the frequency-methods, they operate in Fourier space and allow us to obtain the band structures and the state of the modes simultaneously; in this category, we can cite the plane wave expansion method (PWE) [1,2], the guided mode expansion method (GME) [3] and the Fourier modal method (FMM) [4]. On the other hand, the temporal methods concern those which operate in the direct space. They are adapted the most to realize to carry out simulations which imply an evolution of the fields, such as calculations of transmission and relaxation time at resonance. Among these methods, we distinguish the method of finite element method (FEM) [4] and the finite difference time domain method (FDTD) [5].

It is important to acknowledge that certain methods might be extremely complementary. A reliable method for predicting the transmission of fields in guiding structures entails examining the photonic bandgaps in a crystal without defects, employing a technique from the first category. The initial study can provide information for subsequent propagation calculations using approaches from the second category.

Numerous free and commercial software programs (i.e. BandSOLVE, FullWAVE) have been developed and widely utilized for the numerical analysis and resolution of electromagnetic problems related to PhCs. The efficiency of these technologies relies on accurately modeling wave-object interactions, encompassing reflection, transmission, and dispersion diagrams. Their broad applicability consistently aligns with experimental findings.

In this context, our focus centers on specific methods well-suited for studying photonic crystals. The initial section of this chapter will provide a concise overview of the theory of electromagnetic wave propagation in photonic crystals. To achieve this goal, we will revisit Maxwell's equations and the wave equation. The subsequent section will delve into the numerical simulation methods employed in our thesis work, namely PWE, transfer matrix TM, and FDTD methods. We will conclude this chapter by offering a brief presentation of the numerical modeling and simulation tools utilized in this research endeavor.

2. Maxwell's Equations

Modeling an electromagnetic problem is first done by writing Maxwell's equations. Their resolution allows us to characterize and define the propagation of electromagnetic waves within a photonic crystal.

$$\vec{\nabla}\vec{H}\,(\vec{r},t) = 0 \tag{III.1}$$

$$\vec{\nabla}\left(\varepsilon_r(\vec{r})\vec{E}(\vec{r},t)\right) = 0 \tag{III.2}$$

$$\vec{\nabla}\times\vec{E}(\vec{r},t) = -\mu_0\frac{\partial\vec{H}\,(\vec{r},t)}{\partial t} \tag{III.3}$$

$$\vec{\nabla}\times\vec{H}(\vec{r},t) = \varepsilon_0\varepsilon_r(\vec{r})\frac{\partial\vec{E}\,(\vec{r},t)}{\partial t} \tag{III.4}$$

where $\vec{E}(\vec{r},t)$ and $\vec{H}(\vec{r},t)$ denote the electric and magnetic fields respectively, ε_0 and μ_0 represent the electric permittivity and magnetic permeability of a vacuum, ε_r also illustrates the relative permittivity, which is a function of the coordinates of the point in space where $\vec{r}$ and t symbolize the spatial and temporal dependencies.

At the direction of propagation, the fields $\vec{E}(\vec{r},t)$ and $\vec{H}(\vec{r},t)$ are transverse and verify the following wave equations:

$$\vec{\nabla}\times\left(\frac{1}{\varepsilon_r(\vec{r})}\vec{\nabla}\times\vec{H}(\vec{r},t)\right) = -\mu_0\varepsilon_0\frac{\partial^2\vec{H}\,(\vec{r},t)}{\partial t^2} \tag{III.5}$$

$$\frac{1}{\varepsilon_r(\vec{r})}\vec{\nabla}\times\left(\vec{\nabla}\times\vec{E}(\vec{r},t)\right) = -\mu_0\varepsilon_0\frac{\partial^2\vec{E}\,(\vec{r},t)}{\partial t^2} \quad \text{(III.6)}$$

The development in plane waves allows to obtain solutions in the form :

$$\vec{E}(\vec{r},t) = \vec{E}(\vec{r})e^{-j\omega t} \quad \text{(III.7)}$$

$$\vec{H}(\vec{r},t) = \vec{H}(\vec{r})e^{-j\omega t} \quad \text{(III.8)}$$

where the fields $\vec{E}(\vec{r},t)$and $\vec{H}(\vec{r},t)$ can each be seen as a superposition of harmonic modes, λ is the wavelength in vacuum: $\lambda = \frac{2\pi c}{\omega}$ and c is the velocity of light in the vaccum. Additionally, we define the wave vector $\vec{k}$ in a trihedron $(\vec{E},\vec{H},\vec{K})$ where $k = \frac{n^2c^2}{\omega^2}$ (n is expressed as $n^2 = \varepsilon_r(\vec{r})$).

By Fourier analysis, it will now be possible to solve the problem from a linear combination of elements of this basis of harmonic solutions.

The physical field is now represented by the real parts of the complex quantities of the $\vec{E}(\vec{r},t)$ and $\vec{H}(\vec{r},t)$ fields. However, the resolution of the problem is reduced to the following two equations:

$$\vec{\nabla}\times\left(\frac{1}{\varepsilon(\vec{r})}\vec{\nabla}\times\vec{H}(\overrightarrow{r})\right) = \left(\frac{\omega}{c}\right)^2\vec{H}(\vec{r}) \quad \text{(III.9)}$$

$$\vec{\nabla}\times\left(\vec{\nabla}\times\vec{E}(\overrightarrow{r})\right) = \left(\frac{\omega}{c}\right)^2\varepsilon(\vec{r})\vec{E}(\vec{r}) \quad \text{(III.10)}$$

3. Plane Wave Expansion Method (PWE)

Plane-wave decomposition, commonly known as PWE (Plane Wave Expansion), is undoubtedly the method the scientific community uses in photonics, for which the systems studied are generally periodic. It has become a preferred tool for modeling photonic crystals [6,7]. It is among the first formalisms to have been used to demonstrate the existence of photonic band gaps theoretically. The PWE is a vector method that treats the macroscopic electromagnetic problem by applying a periodicity to the boundary conditions.

Bloch's theorem allows decomposing the magnetic or electric field on a plane wave basis and transforming the solution of Maxwell's equations into a classical matrix diagonalization problem (calculation of eigenvalues and eigenvectors). This method is mainly used to analyze the dispersive properties of photonic bandgap materials. Moreover, it provides the frequency, polarization, symmetry and field distribution for the modes of a photonic crystal structure.

Taking into account the periodicity of the dielectric permittivity in a photonic crystal and according to Bloch's theorem, the magnetic field $\vec{H}$, as well as the electric field $\vec{E}$, can be expanded into plane waves as follows:

$$\vec{E}(\vec{r}) = u_{\vec{k}}(\vec{r})e^{i\,\vec{k}\vec{r}} \tag{III.11}$$

$$\vec{H}(\vec{r}) = v_{\vec{k}}(\vec{r})e^{i\,\vec{k}\vec{r}} \tag{III.12}$$

where the functions $u_{\vec{k}}(\vec{r})$ and $v_{\vec{k}}(\vec{r})$ possess all the periodicity of the medium. Then, it is possible to expand $\varepsilon(\vec{r})$, $u_{\vec{k}}(\vec{r})$ and $v_{\vec{k}}(\vec{r})$ into the Fourier series:

$$\varepsilon_r(\vec{r}) = \sum_{\vec{G}} \varepsilon_r(\vec{G})e^{i\,\vec{G}\vec{r}} \tag{III.13}$$

$$\vec{E}(\vec{r}) = u_{\vec{k}}(\vec{r})e^{i\,\vec{k}\vec{r}} = \left[\sum_{\vec{G}} u_{\vec{k}}(\vec{G})e^{i\,\vec{G}\vec{r}}\right]e^{i\,\vec{k}\vec{r}} = \sum_{\vec{G}} u_{\vec{k}}(\vec{G})e^{i\,(\vec{G}+\vec{k})\vec{r}} \tag{III.14}$$

$$\vec{H}(\vec{r}) = v_{\vec{k}}(\vec{r})e^{i\,\vec{k}\vec{r}} = \left[\sum_{\vec{G}} v_{\vec{k}}(\vec{G})e^{i\,\vec{G}\vec{r}}\right]e^{i\,\vec{k}\vec{r}} = \sum_{\vec{G}} v_{\vec{k}}(\vec{G})e^{i\,(\vec{G}+\vec{k})\vec{r}} \tag{III.15}$$

Where $\vec{G}$ is a vector of the reciprocal lattice and $\varepsilon_r(\vec{r})$, $u_{\vec{k}}(\vec{r})$ and $v_{\vec{k}}(\vec{r})$ are the components in reciprocal space. Thus, for example, for the electric field, the equation becomes:

$$-(\vec{G}+\vec{k})\times\{(\vec{G}+\vec{k})\times u_{\vec{k}}(\vec{G})\} = \frac{\omega^2}{c^2}\sum_{\vec{G}} \varepsilon_r\left(\vec{G}-\vec{G'}\right) u_{\vec{k}}\left(\vec{G'}\right) \tag{III.16}$$

The equation above represents an infinite-dimensional linear system due to the presence of an infinite number of variable $\vec{G}$ vectors within the reciprocal array.

The diagonalization process, essential for each value of k, must be executed, then determines the eigenvalues $\omega_n(\vec{k})$ (n being used to number the eigenvalues). The $\vec{k}$ values are restricted to certain symmetry directions of the first Brillouin zone. The dispersion curves of the photonic crystal are then obtained. They represent the band diagrams of the crystal.

Generally, when the K-vectors describe the first Brillouin zone, the $\omega_n(\vec{k})$ frequencies continuously cover the energy spectrum. However, in some cases, there are energy domains in which no $\omega_n(\vec{k})$ modes are accessible. These are photonic band gaps.

The method of decomposing plane waves proves highly efficient for calculating band diagrams in perfectly periodic photonic crystals. However, its applicability encounters constraints when attempting to directly compute dispersion diagrams for non-periodic structures, which may include defects such as waveguides or cavities. To address this challenge, the reintroduction of periodicity disrupted by defects becomes essential. Hence, the super-cell method, pioneered by [5], was introduced. This approach involves placing the defect in the center of a basic cell consisting of multiple rows of patterns and replicating it infinitely in the directions corresponding to the original lattice. This procedure results in the creation of a new, flawlessly periodic lattice (see Figure 1).

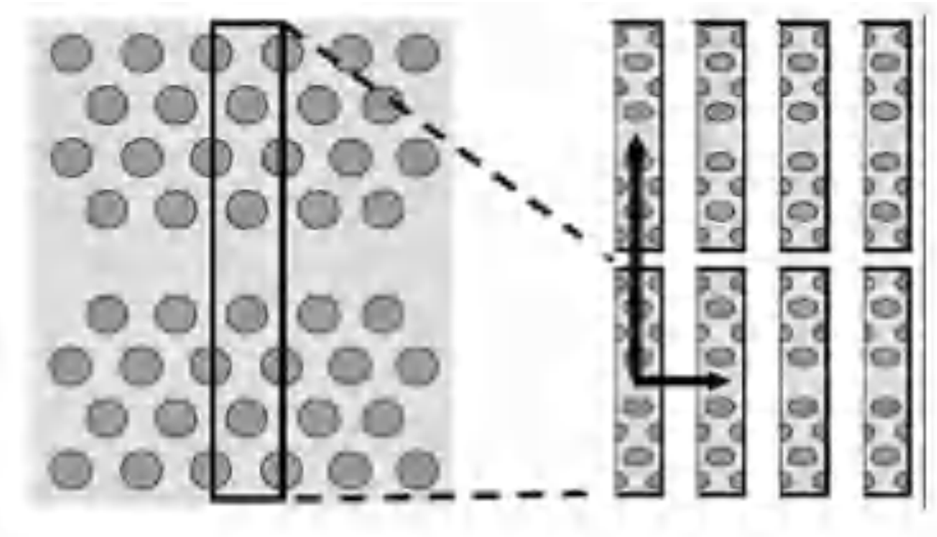

Figure III. 1. Example of a super-cell configuration in the case of a linear defect [6].

The simulated domain corresponds to infinite defects separated by PhC zones. Due to the artificial periodicity introduced by the PWE calculation, these defects will act on each other and may couple. As a result, the size of the super-cell is crucial; a super-cell that is too small would therefore allow the defect modes to interfere with each other, creating artefact modes. On the other hand, a large cell allows the modes to be well isolated. However, it requires more computation time.
Typically, for a crystal made of a dielectric material with a relative permittivity close to 10, the super-cell method is perfectly applicable, provided that the distance between defects is greater than or equal to 4 periods of the original crystal [7].

4. FDTD Method

K.S. Yee introduced the FDTD method in 1966, as documented in reference [8]. This method stands as a potent solution for addressing Maxwell's equations. Executed in the temporal domain, it facilitates a visual comprehension of how an electromagnetic wave propagates within a structured medium, particularly in the context of a photonic crystal.

Based on the algorithm presented by Yee, this method consists of finely meshing the entire structure and a part of the adjacent vacuum. Then, Maxwell's equations are discretized in time and space at each mesh point to obtain the electromagnetic field's temporal evolution in response to a given excitation. Therefore, no matrix inversion or eigenvalue search is involved, as in the case of PWE.

The precise calculation of the electromagnetic field components throughout the entire computational domain and at all times yields a wealth of information, even in highly-indexed contrast-structured media such as photonic crystals. The Fourier transform is particularly useful in this regard. From the propagation of a single temporal pulse, one can obtain frequency spectra at various points of the structure and harmonic field maps, which leads the user to perform real numerical experiments to understand and schematize the propagation processes within the photonic crystal.

The evolution of computing resources has made this method one of the most appreciated for the study of propagation in photonic crystals. Like many numerical methods: the direct calculation of all the field components at any point of the structure requires necessary computing resources, thus limiting the calculation of 3D structures to a few crystal periods, even for the most powerful computers. Therefore, we will often be confronted with 2D calculations in this thesis. Nowadays, the computation time is constantly decreasing. A personal computer allows the 2D modeling of a photonic crystal structure of about 20x50µm in a few minutes.

4.1. Scheme of Yee

Yee's algorithm calculates the time-domain components of the electromagnetic field in an arrangement. This method defines and discretizes a computational domain with a spatial mesh of steps (Δx, Δy, Δz). The temporal space is discretized with a step size Δt. Yee's algorithm uses a spatial mesh where 4 H-field components surround each E-field component and vice versa (Figure 2) [9].

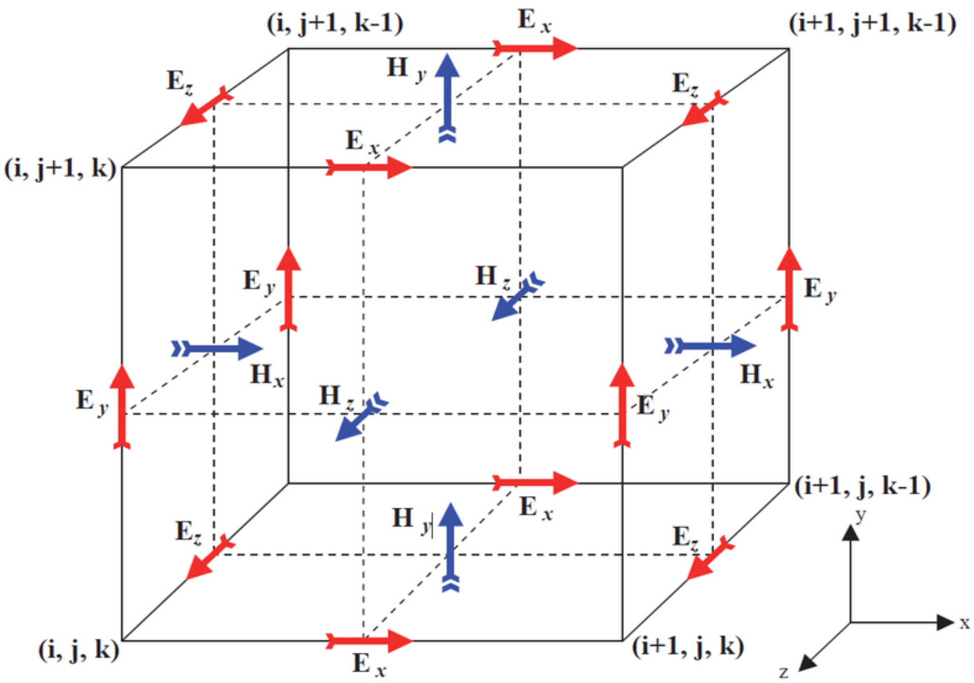

Figure III. 2. 3-dimensional Yee cells [9].

The calculation of the components of the electric field and the components of the magnetic field is done in an alternating manner. The electric fields, E, are calculated with a time shift of half a temporal iteration compared to the moments when the magnetic fields, H, are calculated. This means that H is calculated at time (t+n.Δt), and E is calculated at a time (t+1/2+n.Δt) (Figure 3). Thus, the principle of centered derivatives is preserved [10].

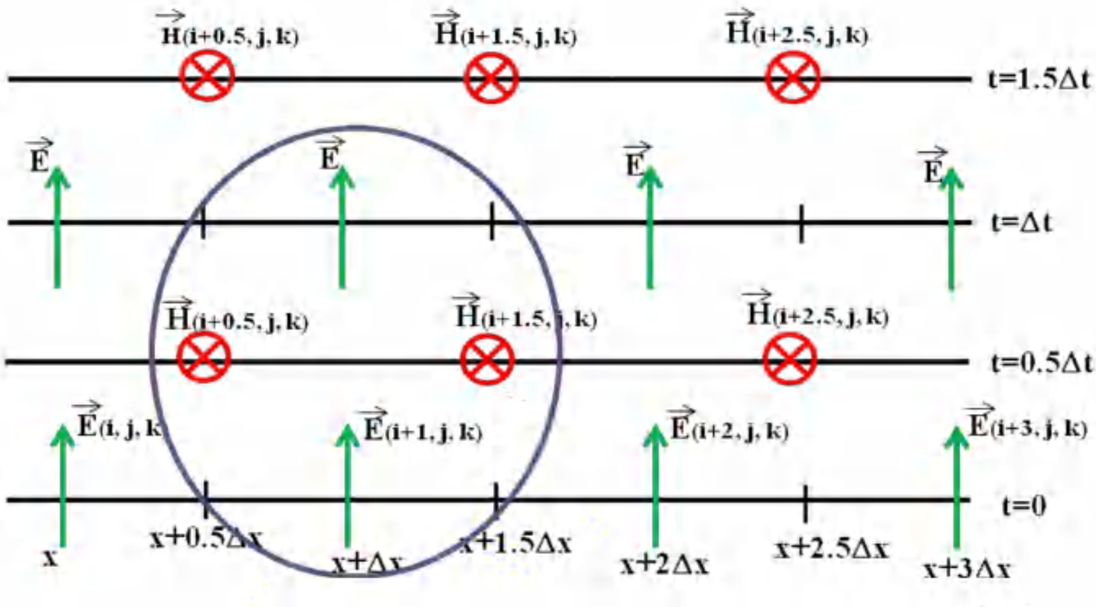

Figure III. 3. Alternative calculation of E- and H-fields.

This arrangement has two significant advantages:

- It ensures a fully explicit iterative process; thus, it has good computational efficiency and no matrix inversion.
- It allows a natural centering of the finite temporal differences.

Figure 4 (a, b) represents the two-dimensional Yee cell for the TM and TE modes, respectively.

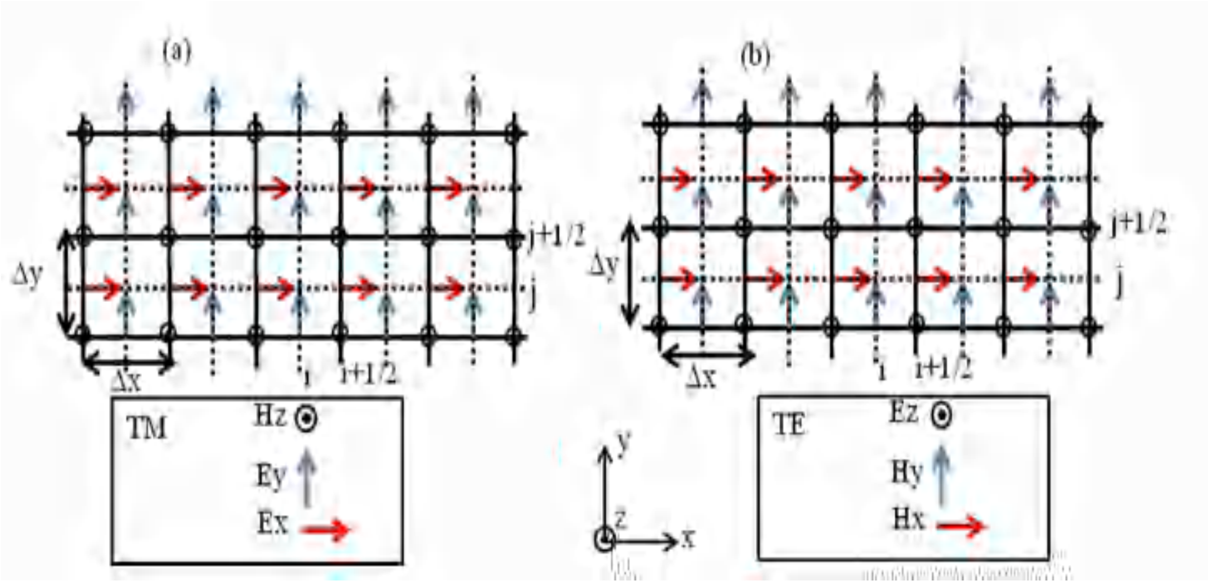

Figure III. 4. The two-dimensional Yee cell: (a) TM mode (b) TE mode [11].

4.2. Stability Conditions and Convergence

To ensure numerical stability, it is necessary that within one temporal iteration, any point of a wave should not be able to cross more than one FDTD cell. In other words, the algorithm can only propagate the wave from one node to an adjacent node. Therefore, the temporal sampling interval should be chosen small enough to avoid this error.

$$c\Delta t < \frac{1}{\sqrt{\frac{1}{\Delta x^2}+\frac{1}{\Delta y^2}+\frac{1}{\Delta z^2}}} \qquad \text{(III.17)}$$

Δx, Δy, Δz: the discretization steps in space.

c: the propagation speed of a plane wave in the medium.

Δt: the time sampling step.

In the special case where Δx=Δy=Δz, then this condition becomes:

$$\Delta t < \frac{\Delta}{c\sqrt{3}} \qquad \text{(III.18)}$$

4.3. Boundary Conditions

To limit the computational volume and, consequently, the time, and the storage capacity used, it is essential to restrict the open domain of the solution of Maxwell's equations to a bounded domain. This domain should be large enough to encompass the entire structure. Subsequently, the field components must be fixed at a zero value at the edges of the domain. Unphysical reflections appear on these edges and strongly disturb the behavior of the structure. For this purpose, absorbing boundary conditions are most commonly used. These conditions eliminate any energy propagating outward and encroaching upon the domain boundaries. Therefore, it is necessary to create an algorithm to illustrate these boundary components aimed at reducing reflections. Two families of solutions exist: the Mur condition [12] and the Perfectly Matched Layers (PML) [13].

4.3.1. The Mur Condition

The Mur condition [12] is based on the technique proposed by Engquist and Madja [14], which is applicable exclusively in the context of a Cartesian FDTD mesh. This principle is based on the factorization of the partial derivative operators in the wave equation. In the 2D case, the wave equation is as follows:

$$\frac{\partial^2 u}{\partial x^2} + \frac{\partial^2 u}{\partial y^2} + \frac{1}{c^2}\frac{\partial^2 u}{\partial t^2} = 0 \qquad \text{(III.19)}$$

where u : scalar component of one of the E and H fields.

The equation is in the formula of the product of an operator, named L, by the function u such that Lu =0 and where:

$$L = \frac{\partial^2}{\partial x^2} + \frac{\partial^2}{\partial y^2} - \frac{1}{c^2}\frac{\partial^2}{\partial t^2} \qquad \text{(III.20)}$$

The operator L can be written as a product of operators $L = L^{+}L^{-}$, with :

$$L^{\pm} = \frac{\partial}{\partial x} \pm \frac{1}{c}\frac{\partial}{\partial t}\sqrt{1 - \left(\frac{\frac{\partial}{\partial y}}{(\frac{1}{c})(\frac{\partial}{\partial t})}\right)^2} \qquad \text{(III.21)}$$

Whatever the angle of incidence, the application of L± allowed an absorption of the part of the wave that should be reflected at the interface between the two media (for x = 0 or x = d). A similar factorization is possible for y=0 and y=d.

A second-order approximation of the differential equation should be applied to the tangential components of the field at x = 0 to eliminate the reflected wave:

$$\frac{\partial^2 \mu}{\partial x^2} - \frac{1}{c}\frac{\partial^2 \mu}{\partial t^2} + \frac{c}{2}\frac{\partial^2 \mu}{\partial y^2} = 0 \quad \text{(III.22)}$$

This equation, discretized using the finite difference method, represents the second-order MUR conditions. However, these conditions are not practically feasible for the corners of the computational domain unless they are reduced to first order. Consequently, the differential equation for x=0 simplifies to:

$$\frac{\partial^2 \mu}{\partial x \partial t} - \frac{1}{c}\frac{\partial^2 \mu}{\partial t^2} = 0 \quad \text{(III.23)}$$

These boundary conditions are equivalent for both the E and H field components and are specifically applicable when waves approach the domain's boundary at normal incidence. However, a parasitic reflection will occur for incidents that deviate from normal incidence.

4.3.2. PML Condition

PML-type (Perfectly Matched Layers) boundary conditions are today's most efficient absorbing conditions. They allow for performing calculations on structures of finite lateral sizes and achieving amplitude reflections as low as 10^{-5} (field amplitude) over a wide range of incidences and frequencies. This technique can be applied to all types of structures and geometries, including photonic crystals. These conditions are based on the impedance matching condition between two waves at the interface of two media with the same index, where one of the media is absorbing (with an electrical conductivity σ and magnetic conductivity σ*). The precision of the computation relies on the discretization intervals used for both spatial and temporal aspects. These intervals can be modified following the specific data we aim to gather and the desired level of precision. In simulations of this nature, the excitation source can be either a dipole or a Gaussian source. This source can emit continuously at a specific wavelength or be time-limited with a wide range of wavelengths [15].
In a vacuum, this condition is expressed as:

$$\frac{\sigma}{\varepsilon_0} = \frac{\sigma^*}{\mu_0} \quad \text{(III.24)}$$

Where ε_0 denotes the permittivity of the vacuum and μ_0 its magnetic permeability.
In this case, the wave is not reflected at the interface between the two media and attenuates in the absorbing part. The thickness of the absorbing part can be significant in limiting reflection at the domain boundary. However, this impedance matching is only possible under normal incidence, and reflection at the interface between the two media reappears as soon as one deviates from it. The technique introduced by Berenger in the eighties consists of making the medium absorbent artificially

biaxial. The absorption is then chosen to be non-zero only along the axis normal to the interface between the two media.
At the interface, the incident plane wave is fictitiously decomposed into two waves:

- A normal incident wave that is not reflected at the interface between the non-absorbing medium and the absorbing medium.
- A grazing incident wave for which no absorption occurs. As a result, this wave undergoes no reflection.

Therefore, PML layers allow for the absorption of an incident wave without any reflections, regardless of its incidence angle. This means that a metal wall condition can be imposed at the PML boundary without causing energy reflections in the computational domain.

5. Transfer Matrix Method (TMM)

It was in the 1990s that Pendry and Mackinnon proposed a method for calculating the reflection and transmission properties of finite planar multilayer structures. In this method, the electromagnetic field is calculated step by step during the wave propagation through the structure. For this purpose, a transfer matrix is defined, which relates the field values between two successive points in the layers that make up the structure. This approach is often used to determine one-dimensional stacks' reflection and transmission coefficients, but Pendry has adapted it to the two-dimensional case [16].
To calculate the reflection and transmission coefficients for a two-layer structure, where an electromagnetic wave is incident at the interface between medium 1 and medium 2, the incident wave gives rise to both a reflected and transmitted wave.

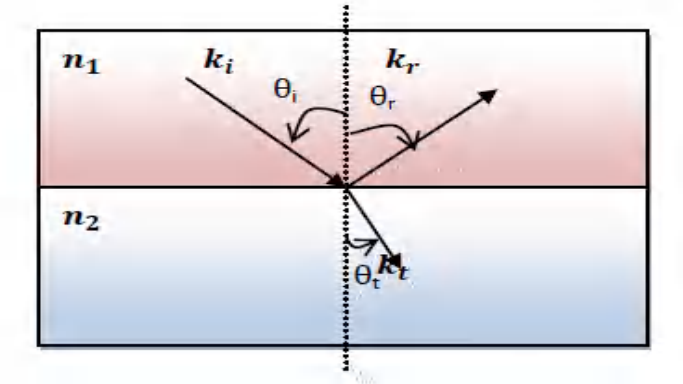

Figure III. 5. A two-layer structure.

The relationship between the refractive indices n_1 and n_2 of each medium, and the angles θ_i and θ_t must satisfy the following condition: $n_1 \sin(\theta_i) = n_2 \sin(\theta_t)$

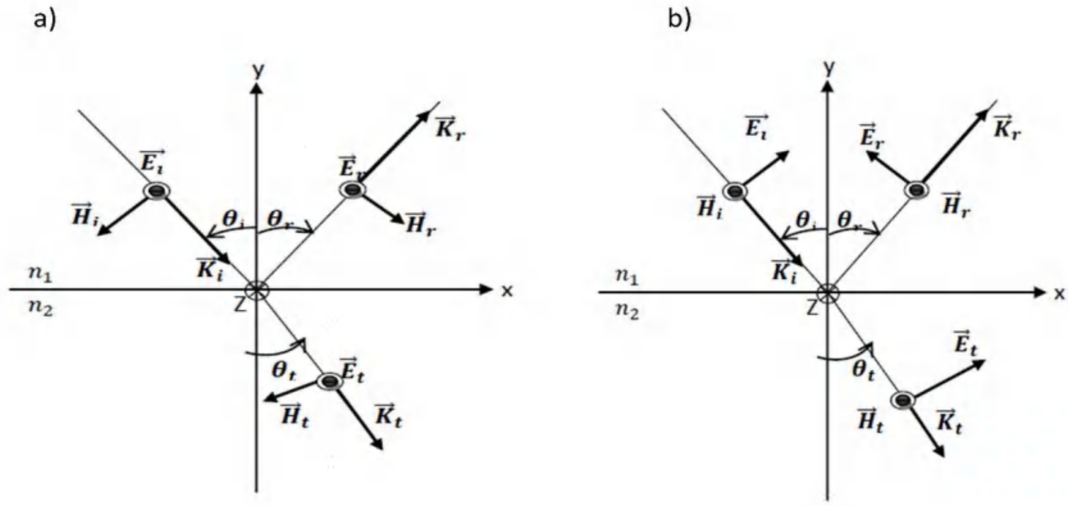

Figure III. 6. (a) Electric field is polarized parallel to the plane of incidence (b) Magnetic field is polarized parallel to the plane of incidence.

- TE polarization

The incident electric field is polarized perpendicular to the plane of incidence, the magnetic field is contained in the plane of incidence (Figure 6(a)).

As a consequence of the continuity of the tangential components of E and H, we have :

$$E_{Ti} + E_{Tr} = E_{Tt} \tag{III.25}$$

$$H_{Ti}\cos\theta_i - H_{Tr}\cos\theta_r = H_{Tt}\cos\theta_t \tag{III.26}$$

- TM polarization

For the case where the incident magnetic field is polarized perpendicular to the plane of incidence and the electric field is contained in the plane of incidence, the tangential components of the electric fields are given by cos(θ) (Figure (b)).

$$H_{Ti} + H_{Tr} = H_{Tt} \tag{III.27}$$

$$E_{Ti}\cos\theta_i - E_{Tr}\cos\theta_r = E_{Tt}\cos\theta_t \tag{III.28}$$

The transfer matrix method is a valuable tool for the numerical study of finite-size structures such as photonic crystals. The structure is divided into successions of periodicity (V) layers, and the transfer matrix links the fields of one layer to another. The expression for a single layer can be formulated according to the second-order theory of the TMM

$$\mathcal{Q}_i = \begin{bmatrix} \cos d_i\varrho_i & (-\frac{i}{\mathrm{P}_i})\sin d_i\varrho_i \\ -i\mathrm{P}_i\sin d_i\varrho_i & \cos d_i\varrho_i \end{bmatrix} \tag{III.29}$$

$$\varrho_i = \frac{\omega}{c} n_i \cos\theta_i \tag{III.30}$$

The variable "d_i" represents the thickness of the layer.

The complete transfer matrix of the one-dimensional photonic crystal (PhC) is expressed as the multiplication of transfer matrices for each individual layer.

The Transfer Matrix Method (TMM) offers several advantages. It is an effective algorithm for computing reflectivity and transmission in multilayer structures. It accommodates both real and complex values for the refractive index. Additionally, the TMM is capable of handling multilayer structures with any number of layers, regardless of their arrangement or periodicity. Even when the layers are periodic, the unit cell can have more than two layers. Moreover, there are no limitations on each layer's thickness or refractive index, allowing for independent definitions. This makes the TMM particularly suitable for modeling structures comprised of diverse periodic multilayers and those exhibiting significant refractive index contrast between layers.

The TMM calculates the field within the structure by propagating it from one layer to another using matrix relations. However, the Transfer Matrix Method does have some limitations. It assumes an infinite plane perpendicular to the propagation direction, which is not realistic as each layer in a multilayer structure is finite in extent. Another drawback is its inability to handle pulse propagation, which is limited to continuous waves. To model pulses, the TMM must be combined with the Fourier transform. Alternative methods, such as the finite difference time domain method, are more suitable for pulse modeling.

6. Modeling and simulation tools

Creating and designing photonic crystal components demands specialized simulation tools. These computational instruments play a crucial role in furnishing essential insights into the functionality of these devices. In alignment with the outlined numerical techniques, we will briefly introduce the methods employed in the present thesis.

6.1. RSoft Photonics Suite software: an overview

The foundational software in the RSoft Photonics Suite, illustrated in Figure 7, is RSoft CAD. This program is dedicated to the design of photonic devices and optical communication systems. Within its framework, there exist various simulation modules such as BeamPROP, FemSIM, Fullwave, BandSOLVE, GratingMOD, DiffractMOD, and ModePROP. These modules play a crucial role in conceptualizing and examining optical devices and nano-scale optical structures. RSoft CAD specifically outlines the material characteristics and structural geometry of photonic devices. Initially, users need to establish a system through the interface. Subsequently, they can employ one or more simulation modules to depict diverse aspects of the device's performance. This modular approach to the design and simulation of photonic devices is one of the advantages of the software. In "RSoft's Photonic Suite", every program operates within a unified environment, facilitating seamless data distribution among the various modules.

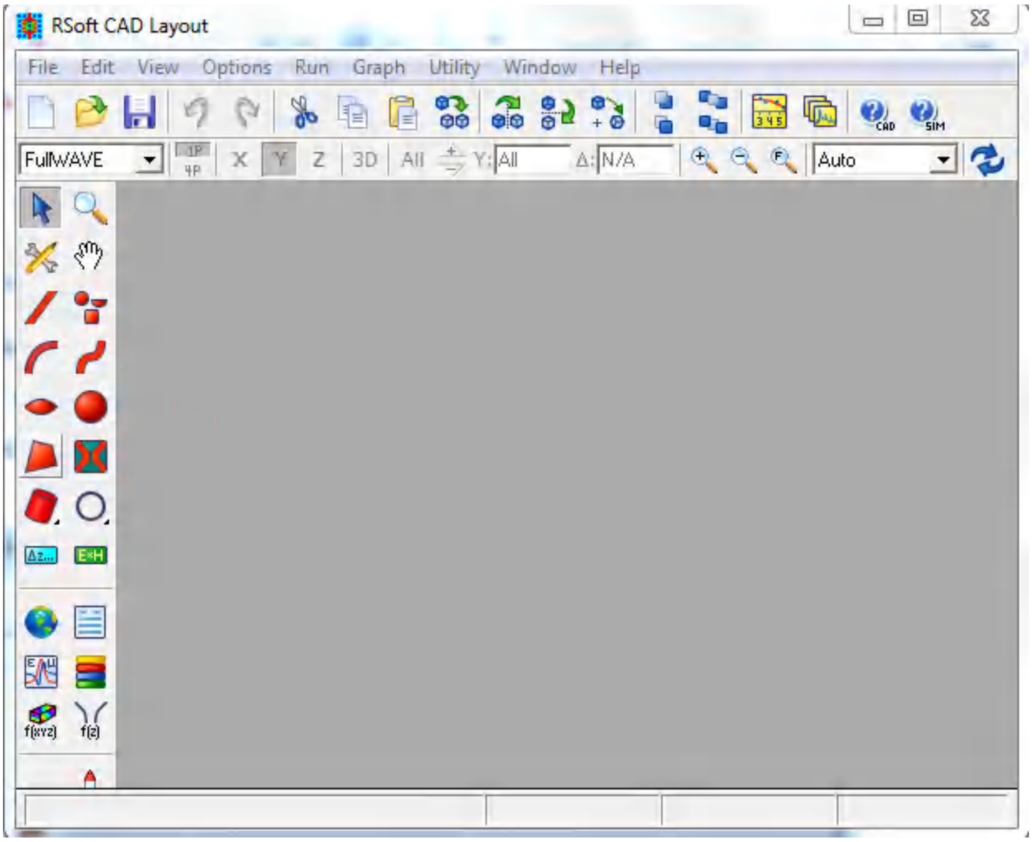

Figure III. 7. The interface of RSoft software showing the menu bar at the top, toolbars at the top and left, and the status bar at the bottom.

6.2. BandSOLVE

The manuscript's depiction of photonic band structures relies on simulation results supported by "BandSOLVE," a commercial software developed by RSoft. This simulation module utilizes the plane-wave method to generate and analyze photonic band gap structures. Specifically designed for conventional photonic bandgap periodic structures, such as 2D and 3D photonic crystals with or without defects, BandSOLVE is an ideal tool for producing detailed band diagrams.

BandSOLVE primarily serves the purpose of optimizing the properties of photonic crystal structures. Following this optimization, the structures are then simulated using the FDTD method within the FullWAVE module. This approach allows for the examination of time-dependent properties, including losses, and enables the calculation of field distributions in finite-dimensional structures.

Furthermore, BandSOLVE extends its applicability to fiber structures like photonic crystal fibers, presenting a unique advantage in studying these structures that can be challenging with other simulation techniques.

The simulation dialogue box for BandSOLVE is outlined as follows **(Figure 8**).

It is necessary to consider two different propagation directions in two dimensions: TE (with the E field perpendicular to the hole axis) and TM (where E is parallel to the hole axis). These two polarizations are decoupled and give rise to two independent band diagrams. There may not be a band gap in both cases.

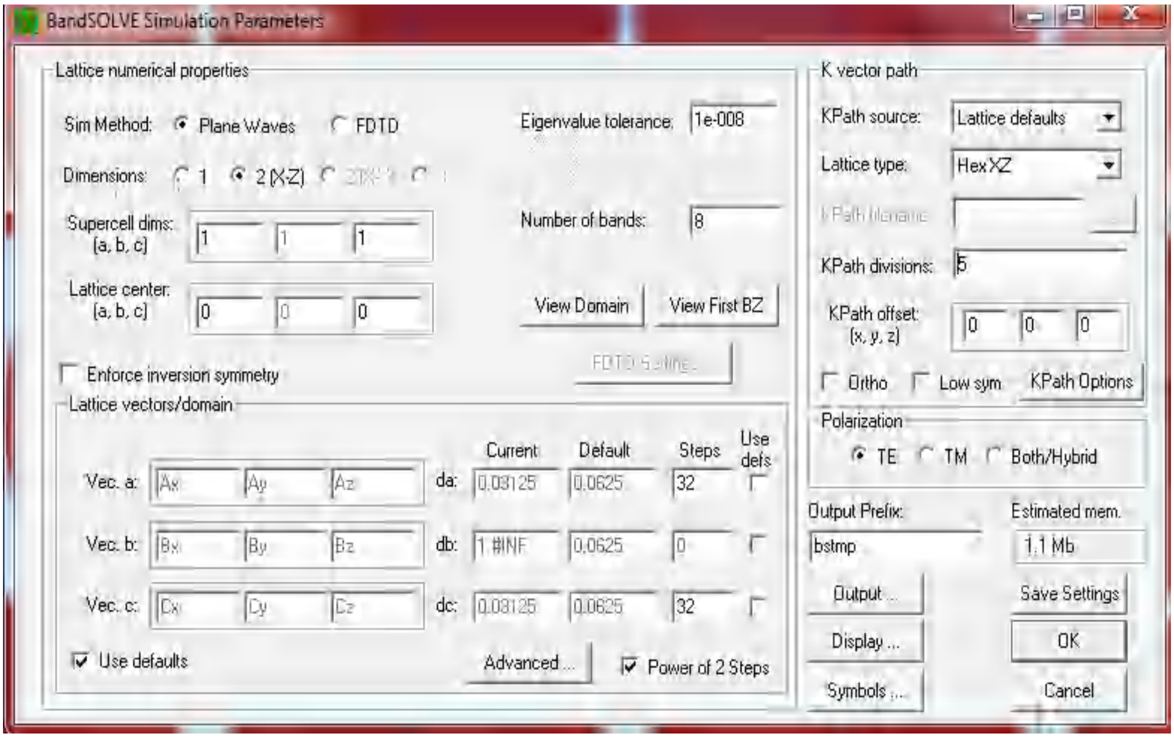

Figure III. 8. The BandSOLVE dialogue box.

6.3. FullWAVE

Similar to Bandsolve, the Fullwave simulator is an extra software module created by RSoft. Utilizing the widely recognized Finite Difference Time Domain (FDTD) approach [17], it is fully incorporated into the RSoft CAD environment. This integration enables users to specify material properties and the structural geometry of a photonic device. Fullwave excels in accurately simulating structures comprising diverse materials, including dielectric, magnetic, or metallic substances, along with anisotropic, dispersive, and nonlinear materials. Its adaptability makes it ideal for our simulations, as it facilitates the examination of the temporal evolution of the electromagnetic field at any location within the structure. Consequently, we can generate detailed maps of the electromagnetic field at various points and time intervals. The knowledge of the field's evolution as a function of time also leads to obtaining information on the spectral response of the photonic crystal structure.

To guarantee the effective operation of the software and the convergence of results, it's crucial to establish the structure's environment and, consequently, define the boundary conditions. The imposition of absorbing conditions at the calculation domain's edges becomes essential. This measure helps prevent parasitic reflections generated at the boundaries of the FDTD calculation window, effectively simulating an open domain. In our investigation, we have employed the absorbing layer model of the PML type (Perfectly Matched Layer), as outlined and explained earlier. This model is particularly well-suited for the accurate representation of photonic crystals [13,18].

7. Conclusion

In this chapter, we've highlighted the current availability of various techniques for modeling and solving problems related to photonic crystals and periodic structures. These methods serve as complements, predicting field propagation and the emergence of photonic band gaps in crystal structures. Each numerical approach, with its distinct formulation, comes with its own set of advantages and drawbacks, varying in suitability for studying different systems. Therefore, the selection of a computational method is crucial, primarily guided by factors such as complexity, appropriateness for the system in focus, the anticipated physical behavior, the specific problems to be addressed, and the available computational resources.

In this part, we've introduced the refined plane wave approach tailored for periodic structures. This method streamlines the resolution of wave equations for presumed infinite periodic structures with precision. Furthermore, to ascertain the parameters necessary for attaining specific optical functions and dynamic traits like transmission, field placement, and quality factor, we utilized the FDTD method. This approach relies on the direct solution of Maxwell's equations, enabling us to derive a thorough response for the examined structure. Furthermore, the transfer matrix technique has been described. It combines the incident electromagnetic field with the transmitted electromagnetic field. The main advantage of the transfer matrix is that it can calculate the transmission and reflection coefficients for a photonic crystal with a finite dimension.

Finally, we have presented two simulation modules “Bandsolve and Fullwave”. They are widely used in the photonic crystal community to calculate the band diagrams, transmission spectra and electromagnetic field distributions.

References

[1] K.-M. Leung, Y.F. Liu, Photon band structures: The plane-wave method, Physical Review B. 41 (1990) 10188.

[2] S. Shi, C. Chen, D.W. Prather, Plane-wave expansion method for calculating band structure of photonic crystal slabs with perfectly matched layers, J. Opt. Soc. Am. A, JOSAA. 21 (2004) 1769–1775. https://doi.org/10.1364/JOSAA.21.001769.

[3] L.C. Andreani, D. Gerace, Photonic-crystal slabs with a triangular lattice of triangular holes investigated using a guided-mode expansion method, Phys. Rev. B. 73 (2006) 235114. https://doi.org/10.1103/PhysRevB.73.235114.

[4] L. Li, New formulation of the Fourier modal method for crossed surface-relief gratings, J. Opt. Soc. Am. A, JOSAA. 14 (1997) 2758–2767. https://doi.org/10.1364/JOSAA.14.002758.

[5] S. Guo, S. Albin, Simple plane wave implementation for photonic crystal calculations, Optics Express. 11 (2003) 167–175.

[6] D. Neel, Etude en champ proche optique de guides à cristaux photoniques sur SOI, PhD Thesis, Lyon, INSA, 2006.

[7] J.-M. Lourtioz, Cristaux photoniques et «gaps» de photons-Aspects fondamentaux», Techniques de l'Ingénieur, AF. 3 (2004) 07.

[8] K. Yee, Numerical solution of initial boundary value problems involving maxwell's equations in isotropic media, IEEE Transactions on Antennas and Propagation. 14 (1966) 302–307. https://doi.org/10.1109/TAP.1966.1138693.

[9] C. Finco, Étude de l'impact simultané des propriétés électriques, diélectriques et magnétiques du sous-sol sur la mesure géophysique par méthode électromagnétique inductive dans le domaine temporel (TDEM), phdthesis, Sorbonne Université, 2019. https://theses.hal.science/tel-02978830 (accessed May 15, 2023).

[10] A. Harhouz, Contribution à l'étude et la conception des capteurs à base de cristaux photoniques, PhD Thesis, Université de M'sila, 2017.

[11] O. Arar, Modélisation par des systèmes électromagnétiques cas des matériaux anisotropes, (2013).

[12] G. Mur, Absorbing Boundary Conditions for the Finite-Difference Approximation of the Time-Domain Electromagnetic-Field Equations, IEEE Transactions on Electromagnetic Compatibility. EMC-23 (1981) 377–382. https://doi.org/10.1109/TEMC.1981.303970.

[13] J.-P. Bérenger, Perfectly Matched Layer (PML) for Computational Electromagnetics, Morgan & Claypool Publishers, 2007.

[14] B. Engquist, A. Majda, Absorbing boundary conditions for numerical simulation of waves, Proceedings of the National Academy of Sciences. 74 (1977) 1765–1766.

[15] L. Ferrier, Micro-nano structures à base de cristaux photoniques pour le contrôle 3D de la lumière, PhD Thesis, Ecole Centrale de Lyon, 2008.

[16] G.N. Pandey, S.P. Ojha, Band structure, group velocity, effective group index and effective phase index of one dimensional plasma photonic crystal, Optik-International Journal for Light and Electron Optics. 124 (2013) 3514–3519.

[17] K. Yee, Numerical solution of initial boundary value problems involving maxwell's equations in isotropic media, IEEE Transactions on Antennas and Propagation. 14 (1966) 302–307. https://doi.org/10.1109/TAP.1966.1138693.

[18] A. Mekis, S. Fan, J.D. Joannopoulos, Absorbing boundary conditions for FDTD simulations of photonic crystal waveguides, IEEE Microwave and Guided Wave Letters. 9 (1999) 502–504.

Chapter 4.

Results and interpretations.

Introduction

Photonic crystals are materials that have a periodic variation in their refractive index, which causes them to exhibit unique optical properties. The structure of these materials is similar to that of a crystal, with a regular repeating patterns. One of the key characteristics of photonic crystals is their ability to control the propagation of electromagnetic waves. By adjusting the size, shape, and arrangement of the periodic features in the crystal, it is possible to generate a band gap termed a photonic band gap. The latter prevents the propagation of light within a specific range of wavelengths, creating a range of forbidden frequencies. This feature is used to confine light to small regions. Due to their interesting characteristics of PhC, they have been utilized in diversity fields and applications as well as sensors. Sensors are vital devices with exciting applications in modern technology and science domains. Due to the photonic bandgap and compactness features, photonic crystals provide a promising platform for developing integrated sensors with ultrahigh resolution and low dispersion losses. Several types of sensors based photonic crystals have been created and fabricated using a variety of photonic crystal structures. Especially, nanocavities coupled with waveguides configuration tend to be more attractive due to their outstanding performances [1,2].

This chapter is divided into two main parts. The first part discusses the study of a two-dimensional photonic crystal-based device capable of detecting changes in temperature using a ring resonator configuration. The resonator, coupled between two linear waveguides, comprises core/shell particles, providing high sensitivity and a high-quality factor. In the second part, we utilized one-dimensional photonic crystal-based sensors to detect cancerous cells. We chose 1D PhC due to its simple structure, compactness, and low costs. In the first part, the detection mechanism relies on the resonance wavelength shift caused by the thermos-optic effect applied to the silicon rods. However, in the second part, the sensing principle is based on the shift of the wavelength peak, which results from a change in the refractive index (RI) of the analyte. The results from each study are presented and analyzed, highlighting the importance of carefully selecting both the material and geometric parameters for optimizing the performance of the sensor.

Part 1. Temperature Sensor Based on Two-dimensional Photonic Crystal Core/Shell Rods

1. Introduction

PCs have the ability to facilitate the development of novel photonic devices. Due to the continued demand for photonic devices in sensing applications, research into PhCs has become a developing sector with significant resources committed to their technological advancement. Over the last two decades, sensor-based PhCs have been the focus of intense research, particularly for the detection of various physical parameters such as temperature, pressure and acceleration, as well as biological and chemical substances. Besides, optical sensor-based PhCs provide intriguing characteristics such as high sensitivity, smaller integration size, high quality factor, rapid response speed, stability, flexibility, and lower costs. Therefore, this work aims to design an ultra-compact optical sensor based on PhC to detect the temperature variation with high sensitivity and a high quality factor.

2. The Fundamental Structure

The initial step towards the design of 2D-PhC is a full understanding of their optical properties. The dispersion diagram of a photonic crystal provides complete details regarding its optical characteristics. The dielectric contrast between the materials that comprise the crystal should be sufficiently large to form this graph. The photonic band gap depends on the geometrical parameters of the PC and the refractive index of the dielectric or metallic material used to make it. To obtain a large bandgap in the infrared range, we used a square lattice of 2D photonic crystal consisting of circular silicon rods placed in a vacuum medium. There are (21×21) rods in the X and Z directions (Figure IV.1. 1 (a)). Each Si-rod has a radius of 0.245a, where a is the distance that separates the centers of two adjacent rods termed as the lattice constant as depicted in (Figure IV.1. 2 (b)).

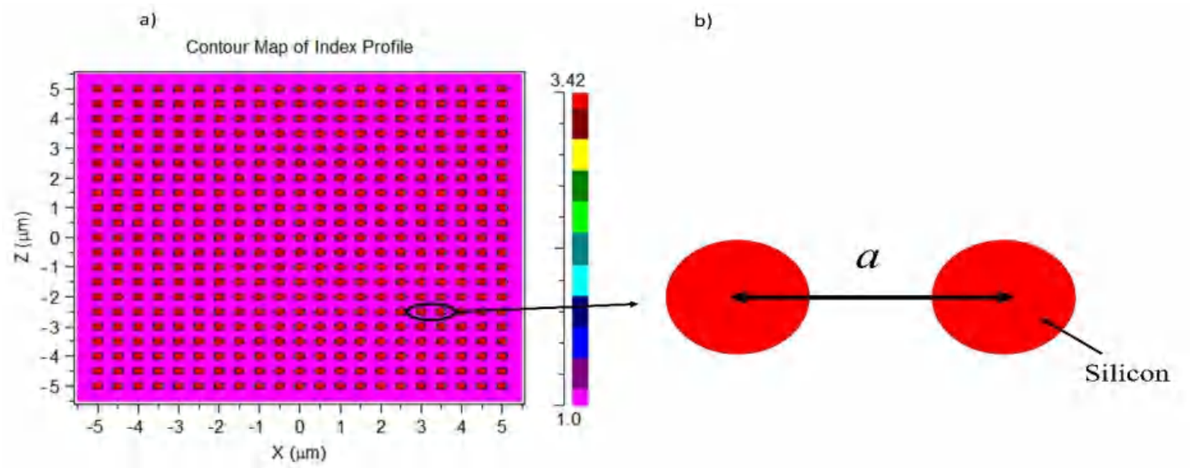

Figure IV.1. 1. a) Square lattice of Si rods embedded in a vacuum background without defects b) lattice constant of the structure.

The dispersion diagram of the structure without defects for both TE and TM modes is shown in Figure IV.1. 2. They are calculated using the plane wave expansion method. The band diagram of the proposed 2D PhC is normalized with respect to the lattice constant *a*. The Y-axis indicates the zones of normalized frequencies where electromagnetic waves are allowed or not allowed to propagate. The X-axis presents the variation of the wave vector, which changes from the far edge of the irreducible Brillouin zone *M* to the nearest edge *X* and then to the Brillouin zone center *Γ*. The PhC represents two photonic bandgaps for TE polarized light. The first one ranges between 0.25581 (a/λ) and 0.36315 (a/λ), which is sufficient for sensor design. Moreover, the photonic bandgap falls within the third window of optical transmission.

An incident EM wave propagates with a resonant wavelength dropping into the PBG will be reflected entirely by the PhC. The inset of Figure IV.1. 2 illustrates the reciprocal lattice of the device.

Figure IV.1. 3 displays the Ey field distribution perpendicular to the plan of propagation, as well as the dispersion of incoming light in the dielectric structure.

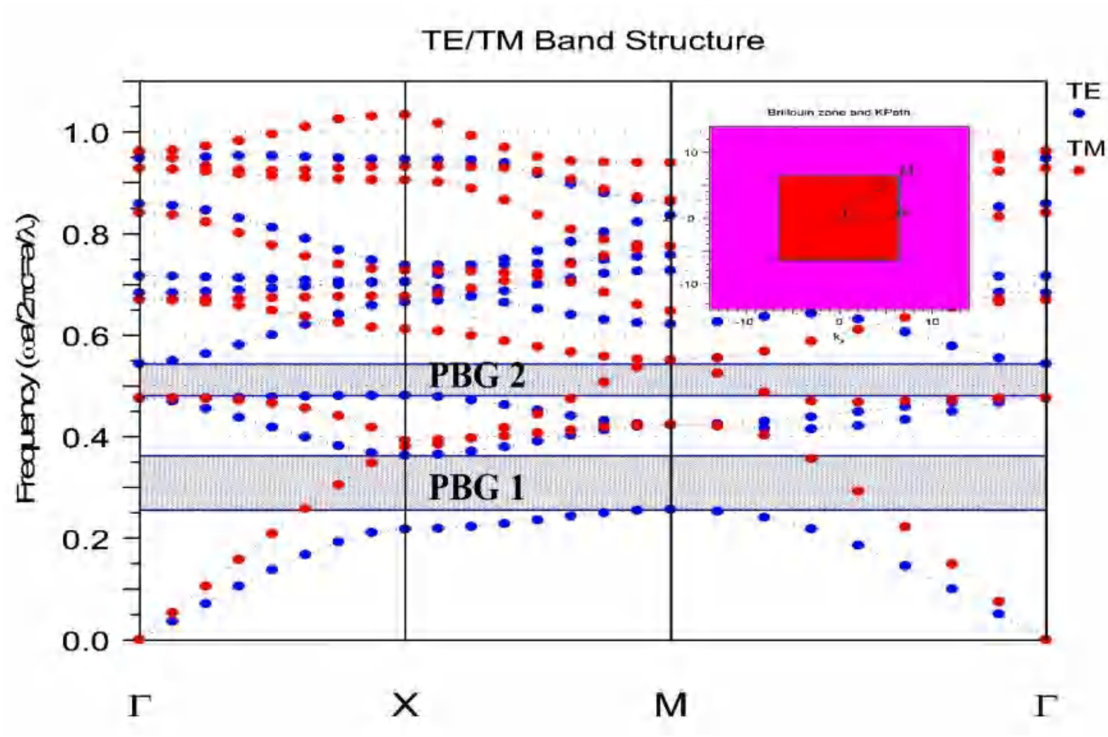

Figure IV.1. 2. The dispersion diagram of Si rods arranged into a square lattice. Inset: reciprocal lattice.

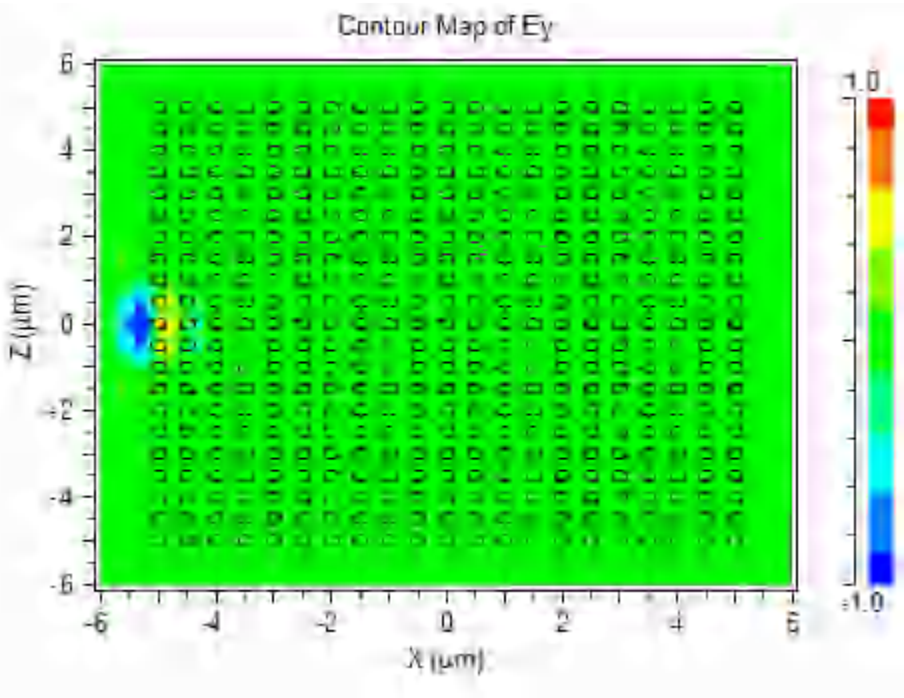

Figure IV.1. 3. The Ey field distribution in the structure without defects.

3. Temperature Sensor Design

Our objective in this section is to investigate a temperature sensor using 2D PhC nano-cavity coupled with two linear waveguides. In the designed device, we have introduced two quasi-waveguides connected via a resonant cavity (Figure IV.1.4). These waveguides are introduced into the perfect PhC by removing several silicon particles in the *X* direction. These linear defects are labeled as “port A” and “port B”. The nanocavity was designed with eight Core\Shell rods (C\S). The latter is obtained by creating an air hole in the center of the rod. As shown in Figure IV.1. 4 (b), the air hole is called the core, and the shell refers to the layer that surrounds it. The radii of inner and outer of the C\S particles are rc_2=0.062*a* and rs_2=0.26*a*, respectively. From the Figure IV.1. 4(b), it can be noticed that four of the eight rods located at the center of the structure, were moved in both directions (*X* and *Z)* by a distance *d* equal to 20 nm in order to form a quasi-circle shape. These rods are shown with blue color.

The inner and the outer radius of the C\S particle which is placed in the center of the cavity are rc_1=0.062*a* and rs_1=0.1*a*, respectively. A Gaussian-modulated pulse is launched at the port A of the input W1 waveguide, and the light travels through the detector placed at the output waveguide.

a) b)

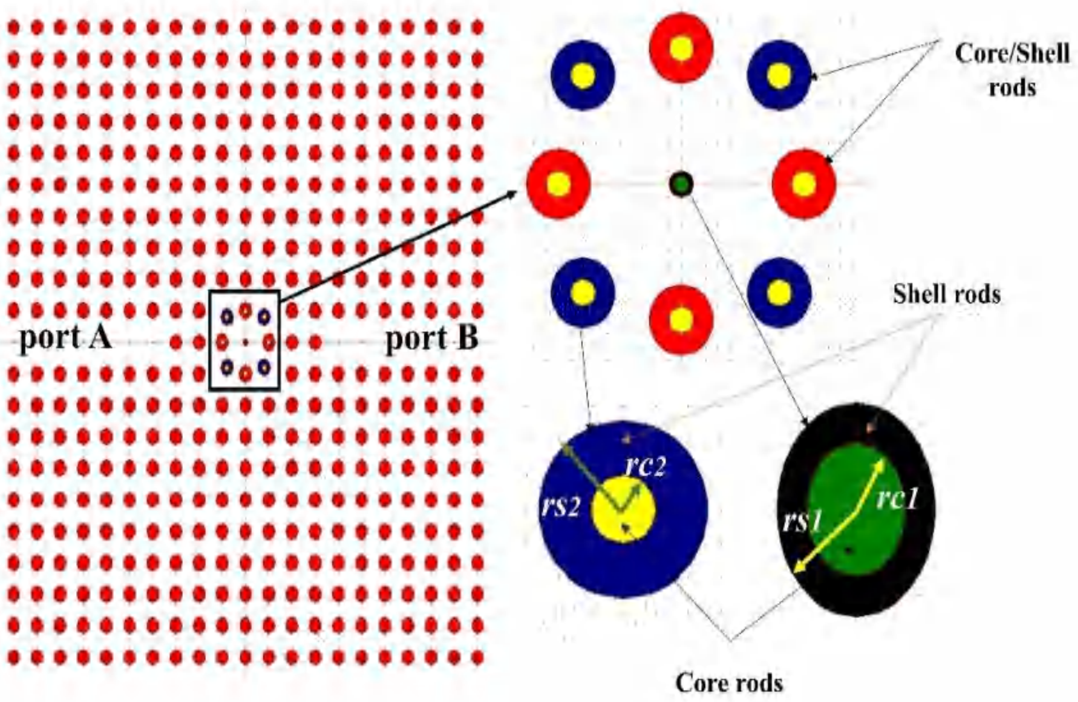

Figure IV.1.4. a) The layout of 2D photonic crystal temperature sensor b) the nanocavity and the core\shell rods.

3.1. Refractive Index Variation Via Thermo-optic Effect

For optical materials that are used in various optical systems or devices such as glasses, semiconductors and crystals, the variation in refractive index with temperature is an important feature, and it is not constant with temperature. The thermo-optic coefficient is the variation of the refractive index with temperature at constant pressure. It is written as *dn/dT*, where n and T indicate the index of refraction and temperature, respectively. It is estimated in degrees Celsius or Kelvin. *dn/dT* is typically very small, on the order of 10^{-3} to 10^{-6}/°C. Despite the fact that the value is quite small, it is possible to measure it with sufficient accuracy. Temperature-dependent optical devices, optical fiber communication systems and semiconductor technology, all require thermo-optic coefficient analyses. “The Temperature Sensor’’ sensing principle is based on the change in refractive index of the silicon medium caused by the thermo-optic effect. The varied refractive index with temperature is expressed as [3,4]

$$n=n_0+\alpha\,\Delta T \qquad \text{(IV.1)}$$

where

n_0: is the refractive index of Silicon pillars at 0°C

α : is the thermo-optic coefficient equal to 2.4×10^{-4}/°C

ΔT: the temperature difference

3.2. The Sensing Properties of The Suggested Device

The temperature sensors are used extensively in a variety of domains, such as climate control, automotive systems, medical equipment and food storage areas. The suggested device is designed to measure and monitor temperature levels from 0°C to 80°C. The sensing mechanism is based on the variation of the refractive index of silicon pillars caused by the thermo-optic effect. The sensing properties of the suggested device are evaluated using Rsoft software. This analysis is mainly done by 2D Finite-Difference-Time-Domain. Absorbing layers of the PML (Perfectly-Matched Layer) type have been added around the structure in order to prevent any reflections at its boundary. These layers have a thickness of 500 nm.

To estimate the sensing properties of the sensor, a Gaussian-polarized TE optical pulse to excite the cavity modes within the given wavelength range is utilized and placed at port A. The transmitted signal is measured using a power monitor placed at the end of port B. Firstly; we investigated the transmission spectrum of the proposed design at 0°C. As illustrated in Figure IV.1. 5(a), a resonant peak is obtained at λ=1536.09 nm with a quality factor of 1181.607. This means a good coupling between the two waveguides and the cavity. Figure IV.1. 5(b) shows the electric field distribution for TE polarized light.

Secondly, we change the refractive index of the silicon medium. By increasing the temperature, the RI would increase according to equation (IV.1). The simulation results indicate that the structure was responsive to variations in temperature in the range of 0°C to 80°C.

Figure IV.1. 6 shows that by changing the temperature from 0 to 80 °C, the defect mode is shifted towards longer wavelengths from 1536.09 nm to 1540.891 nm with a transmission efficiency of more than 99%. Figure IV.1. 7 illustrates the displacement curve of the resonant mode as a function of temperature. From the figure, it is evident that the relationship between resonance and temperature is quasi-linear. This sensor is able to measure a wide range of temperatures with a sensitivity of 62.08 pm/°C. The temperature, the resonant wavelength, wavelength shift, the sensitivity, and the quality factor are given in Table IV. 1. 1.

a)

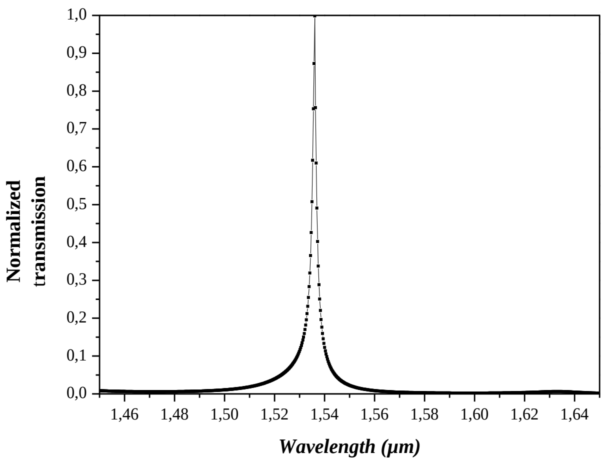

b)

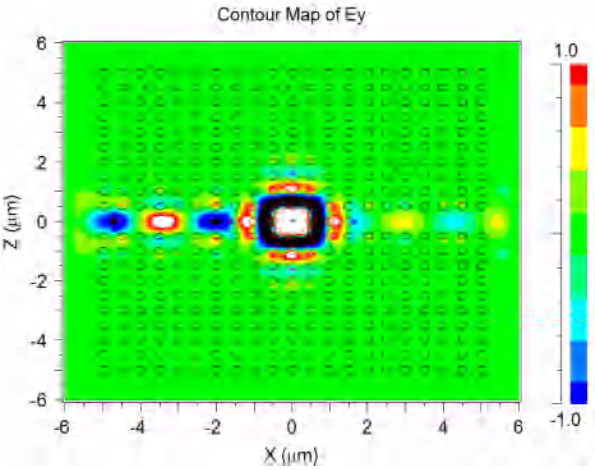

Figure IV.1. 5. a) the resonant mode at 0°C b) The electric field distribution for the TE mode in the x-z plane at λ = 1536.09 nm.

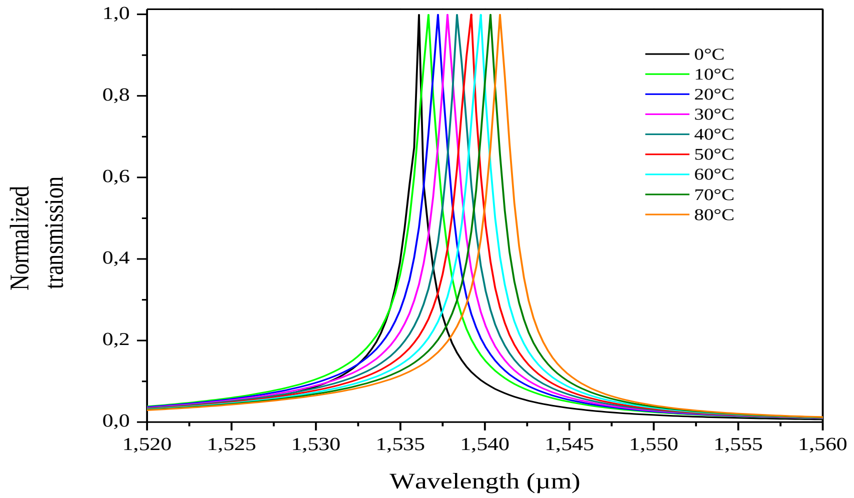

Figure IV.1. 6. The transmission spectra of the temperature sensor design for different temperature.

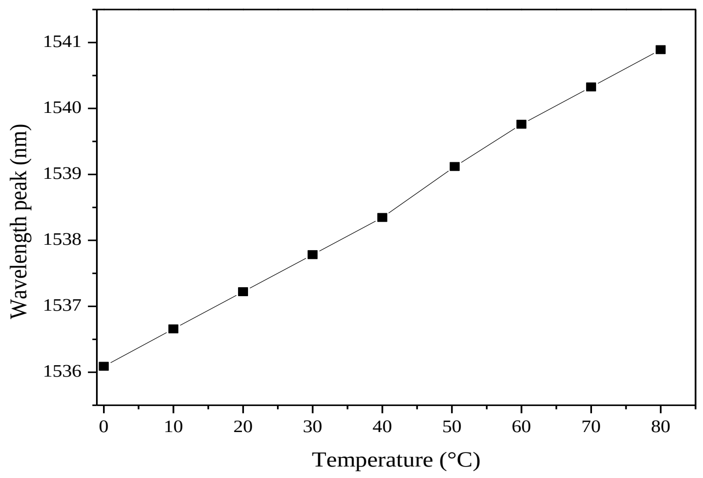

Figure IV.1. 7. The wavelength peak of the resonant mode versus the temperature.

Table IV. 1. 1. Peak wavelength, Δλ, sensitivity and quality factor for different temperature.

(°C)	λ(nm)	Δλ(nm)	S(pm/°C)	Q
0	1536.09	/	/	1181.607
10	1536.657	0.567	56.1	1182.04
20	1537.22	1.13	56.5	1182.476
30	1537.783	1.693	56.43	1098.416
40	1538.347	2.257	56.42	1183.343
50	1539.194	3.104	62.08	1183.995
60	1539.759	3.669	61.15	1184.43

70	1540.325	4.235	60.5	1184.865
80	1540.891	4.801	60.0125	1284.076

3.3. Optimization of The Sensing Properties of The Sensor

To optimize the sensing characteristic of the structure, we added two circles of silicon pillars in the microcavity, as depicted in Figure IV.1. 8. The rods in green have a radius of 0.062×a, while the other black rods have a radius of 0.1×a. After a series of simulations using the FDTD method, the transmission spectra of the optimized design for various temperatures ranging from 0°C to 80°C are investigated and represented in Figure IV.1. 9. As the temperature increases, we observed that the defect mode is red-shifted and has a transmission efficiency of over 99%. Furthermore, as the temperature changes dynamically from 0-80°C in increments of 10°C, the resonant peak moves from 1614.125 nm to 1621.614 nm, respectively. The dependence of resonance on temperature is represented by a curve. The latter is illustrated in Figure IV.1. 10. Moreover, it is important to note that the optimized sensor has a high quality factor of 2506.5. In other words, the light confinement within the microcavity improves and becomes more pronounced, positively affecting the photon lifetime within the microcavity. Additionally, we recorded a sensitivity of 93.6125 pm/°C for this configuration. The simulation results, including the resonant mode, wavelength shift, sensitivity, and quality factor, are displayed in Table IV. 1. 2.

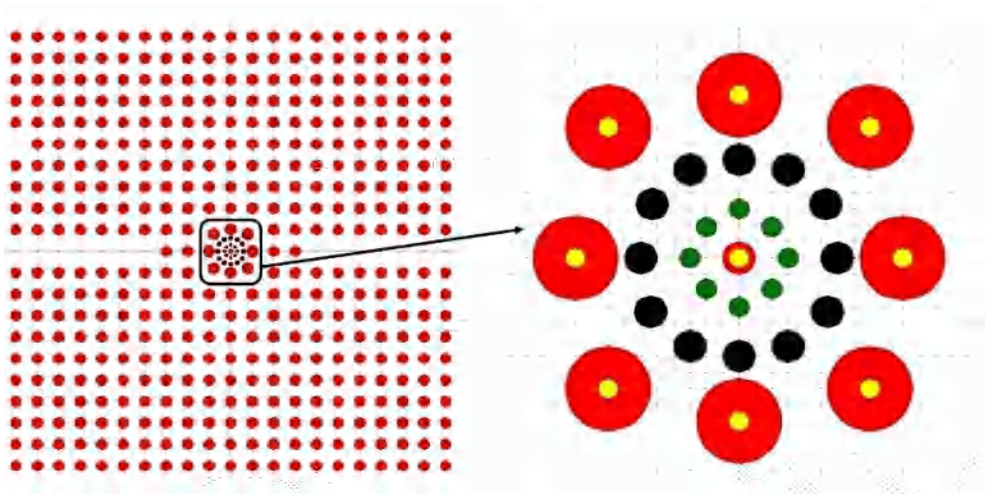

Figure IV.1. 8. The optimized structure with additional silicon rods.

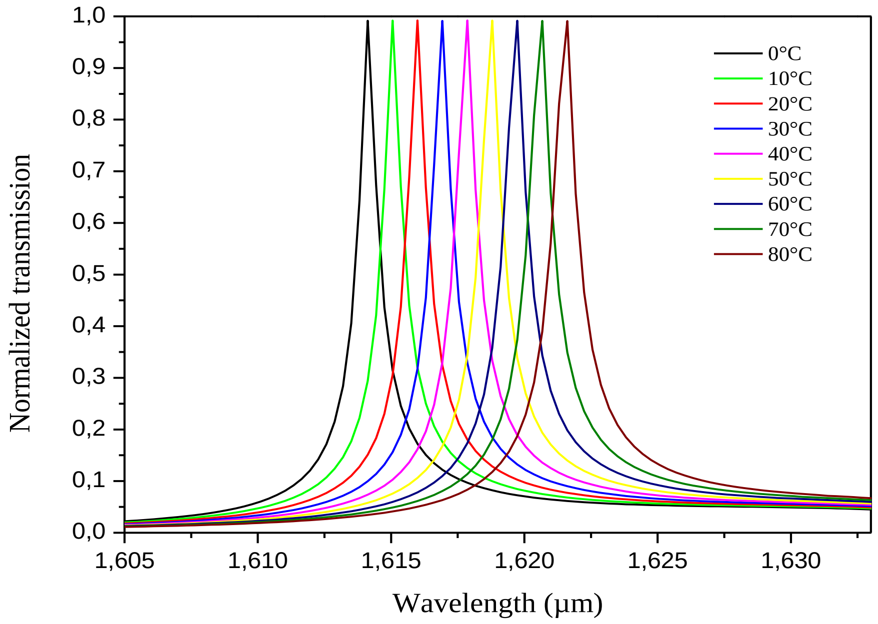

Figure IV.1. 9. The transmission spectrum of the optimized structure for various temperature values.

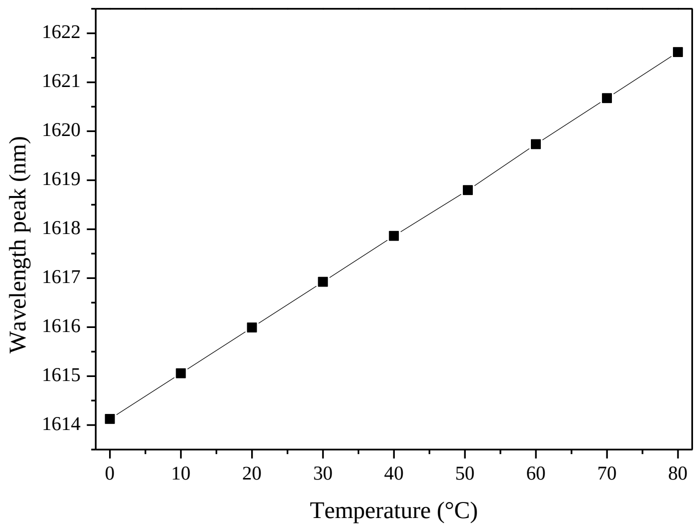

Figure IV.1. 10. The resonant peak as function of temperature.

Table IV. 1. 2. Resonant peak, Δλ, Sensitivity and Q for various temperature.

(°C)	λ(nm)	Δλ(nm)	S(pm/°C)	Q
0	1614.125	/	/	2506.5
10	1615.057	0.932	93.2	2447.2
20	1615.991	1.866	93.3	2385.8

30	1616.925	2.8	93.33	2327.2
40	1617.861	3.736	93.4	2276.4
50	1618.797	4.672	93.44	2200.6
60	1619.735	5.61	93.5	2132.5
70	1620.674	6.549	93.557	2070.0
80	1621.614	7.489	93.6125	1979.9

Table IV. 1. 3 displays a comparison between the proposed temperature sensor and various previously published research studies. It is evident from the table that the proposed sensor has significantly higher sensitivity compared to other designs. These results demonstrate that our configuration has better performance. Furthermore, our device has a footprint of 115.422 μm^2.This very compact design has a capability of being used in sensing applications and can be integrated easily.

Table IV. 1. 3. Comparison of the obtained results with those reported.

Ref	**The structure based photonic crystal**	**S (pm/°C)**
[5]	2D Photonic crystal ring resonator	92.3
[6]	Fano resonance in two dimensional photonic crystal	91.9
[7]	Two dimensional photonic crystal super ellipse ring resonator	65.3
[8]	1D photonic crystal structure	88.7
[9]	whispering gallery modes (WGMs) in a cylindrical photonic crystal fiber micro resonator.	18.72
[10]	Anti-resonant Mach-Zehnder interference base sensor	58.5
[11]	Hexagonal Photonic Crystal Ring Resonator	59.25
[12]	fiber-optic deep-etched silicon photonic crystal	68
[13]	photonic crystal fiber(PCF) using graphene oxide	86
This work	Core/ Shell rods based two dimensional photonic crystal	93.61

3.4. The Effect of The Shell Layer rs_1

In this section, we investigated the effect of outer radius rs_1 on the transmission spectra of the suggested device. We considered three different values of the outer radius 0.08a, 0.1a and 0.12a. We plotted a curve that displays the resonant mode as function of changes in temperature corresponding to the three values of rs_1. Using FDTD method, results obtained indicate a linear relationship between the temperature and the peak wavelength. As depicted in Figure IV.1. 11, the resonance can be tuned and shifted to a longer wavelength with changes in temperature. For rs_1 equal to 0.08, the defect wavelength shifted from 1613.316 nm to 1620.729 nm.

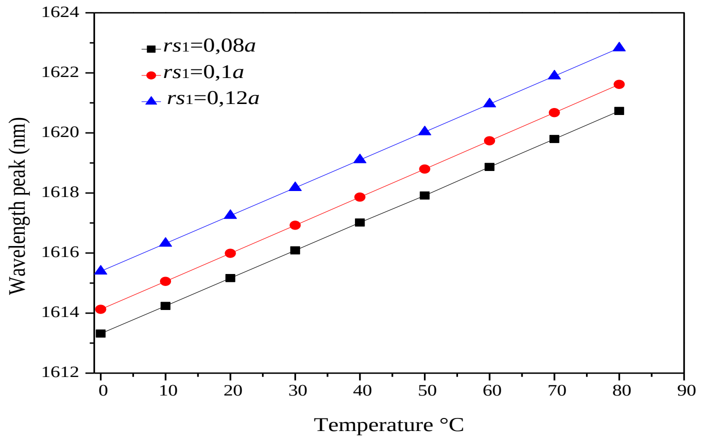

Figure IV.1. 11. The resonant mode as function of the temperature for three values of rs $_1$.

4. Conclusion

To summarize, this study investigates an ultra-compact 2DPhC-based sensor that utilizes Core/Shell (C/S) rods to measure and detect temperature. The device consists of a square array of silicon pillars surrounded by air. The detection mechanism of the sensor relies on detecting the peak wavelength shift, which is caused by the thermo-optic effect and the resulting change in the refractive index of silicon. Using the FDTD method, the simulation results demonstrate that the addition of some silicon rods in the microcavity leads to improved sensitivity and Q factor. Furthermore, the shift of the defect mode is found to be linearly proportional to the radius of rs_1. The suggested device shows a high sensitivity and Q factor when compared to previous studies. The overall size of the sensor is 115.422 μm^2, which is ultra-compact and may offer a promising platform for temperature measurement.

Part 2. A Vertical Slot Based One-dimensional Photonic Crystal for Cancer Sensing

1. Introduction

Cancer is a series of diseases identified by the uncontrolled dividing of abnormal cells, which have the potential to invade and harm nearby tissues and organs. These abnormal cells can also metastasize, or spread to other parts of the body, forming new tumors in different areas of the body. Detecting cancer in its early stages is vital to achieving successful treatment and better patient outcomes. Early detection can lead to easier treatment options and increase the possibility of survival. Several methods and devices are utilized for Detecting malignant cells at an early stage. Optical sensors based on photonic crystals (PhCs) are a favorable option for the early detection of malignant cells. The primary optical feature that distinguishes between malignant and normal cells in cancer is the refractive index [14–17]. Photonic biosensors rely on the contrast created by the difference in refractive indices between cancerous and normal cells. These devices have several advantages over other types of sensors. They can be extremely sensitive, selective and specific, and they can be integrated into small, compact devices. They have the ability to detect and sense a wide range of physical and chemical parameters such as pressure [18,19], gas [20,21], DNA [22].

1D photonic crystals have become an area of significant interest due to their promising advantages, including high reflectivity, low-loss properties, and ease of manufacturing. Accordingly, in this research, an optical sensor utilizing a one-dimensional photonic crystal has been developed to detect five kinds of cancer cells (Jurkat, Hela, PC12 MDA-MB-231, and MCF-7). The transfer matrix method (TMM) is employed to examine the optical characteristics of the structure. The sensing medium in our design is a vertical slot (VS), which is optimized to increase the sensitivity of the sensor. The final optimized device achieves a remarkably high sensitivity of 3021 nm/RIU, surpassing the performance of other similar structures. The results obtained from this study are very promising.

2. The Fundamental Design

Our research objective is to create an optical sensor using a 1D periodic structure as a fundamental configuration that can detect various types of cancer cells. The geometric design being studied is depicted in Figure IV.2. 1 and consists of periodic arrays of SiO_2 (A) and TiO_2 (B) with refractive indices n_1 and n_2, respectively. The ideal multilayer has a period of $d = d_1 + d_2$, where d_1 and d_2 correspond to the thicknesses of constituent layers A and B, respectively. To use this device for cancerous cell sensing a central vertical slot (VS) labeled, as C will be added to the structure, functioning as the detection area. Each layer has a quarter wavelength ($n_1d_1 = n_2d_2 = \lambda_0/4$), where λ_0 is 1.55 μm. In our configuration, the layers A and B utilized had a thickness of d_1 = 269.097 nm and d_2 = 149.038 nm, with corresponding refractive indexes of n_1 = 1.44 and n_2 = 2.6. The designed sensor is symmetrically presented as Air/ $(SiO_2/TiO_2)^V$ /C/ $(TiO_2/SiO_2)^V$/Air , where V is an integer representing the number of periods (V = 13), as illustrated in Figure IV.2. 1.

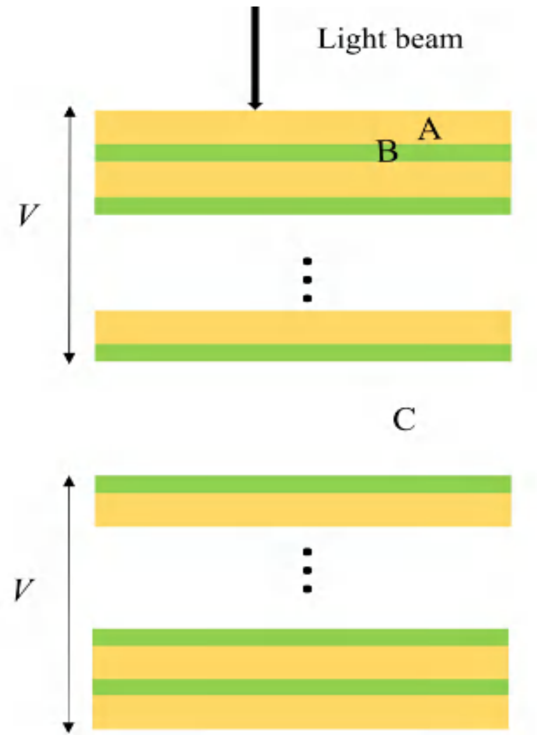

Figure IV.2. 1. Schematic configuration of the multilayer comprising a vertical slot.

3. Non-optimized Sensor Structure

In this part, we will investigate the optical characteristics of the suggested sensor. We used the transfer matrix method to demonstrate the transmission and resonant peak shift of the device when it is normally incident. The numerical results revealed that the suggested design possesses a photonic bandgap (PBG) in the infrared region that stretches from 1302.9 nm to 1894.6 nm in the absence of any defects. As illustrated in Figure IV.2 .2, the width of the bandgap is sufficient to cover the requirements for detection, and the transmission peak produces a significant shift in wavelength.

Initially, the vertical slot was filled with a normal cell that possessed a refractive index of n = 1.35. As illustrated in Figure IV.2. 3, a narrow resonant peak was observed within the PBG. The origin of this peak was the confinement of light within the cavity, and it was situated precisely at 1534.525 nm, with a transmission efficiency of 99.5%. Thus, the observed peak is chosen as a reference to monitor the resonant mode shift as various cancer kinds infiltrate the cavity. By assuming that the thickness of the vertical slot (VS) was 1700 nm, we achieved significant confinement of the optical field within it and long photon lifetime.

It is worth mentioning that the presence of a defect within the structure causes some fluctuation, which impacts the signal response beyond the Bragg gap. When malignant cells of different types, which have defined refractive indices as specified in Table IV.2. 1, are infiltrated into the VS, the defect mode shifts and moves to new frequencies. The shift of the defect peak is depicted in Figure IV.2. 4. A variation of RI from 1.35 (normal cell) to 1.401 (MCF-7 cancerous cell) results in spectral red-shifted from 1534.525 nm to 1575.833 nm. This reveals that the design possesses a larger dielectric region within the vertical slot.

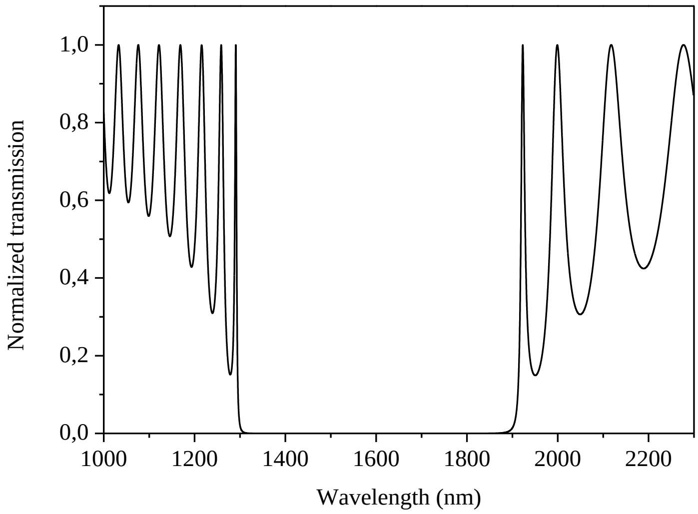

Figure IV.2.2. The transmission spectrum of the perfect 1D PhC at normal incidence.

Table IV.2. 1. Cancer types and refractive index of the used malignant and normal cells [23].

Malignant and normal cells	Cancer category	Refractive index (RIU)
Normal cell	/	1.35
Jurkat	Blood	1.39
Hela	Cervical	1.392
PC12	Adrenal Gland	1.395
MDA-MB-231	Breast	1.399
MCF-7	Breast	1.401

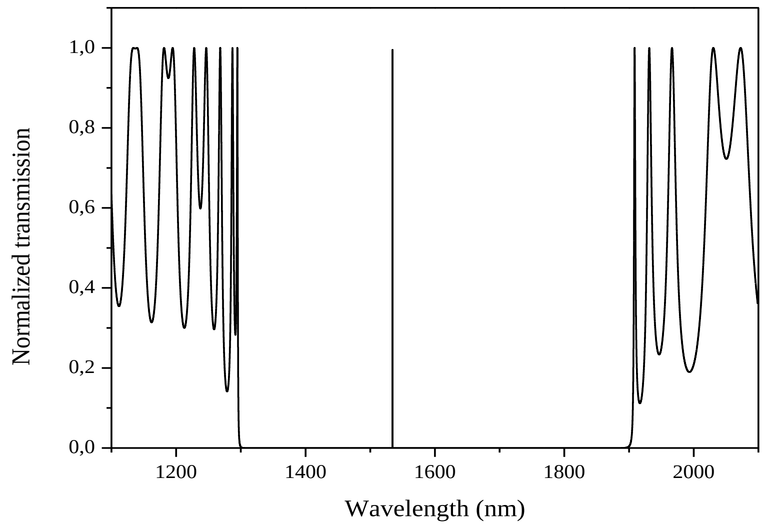

Figure IV.2. 3. The transmission spectrum of the suggested sensor in the existence of a normal cell in the VS.

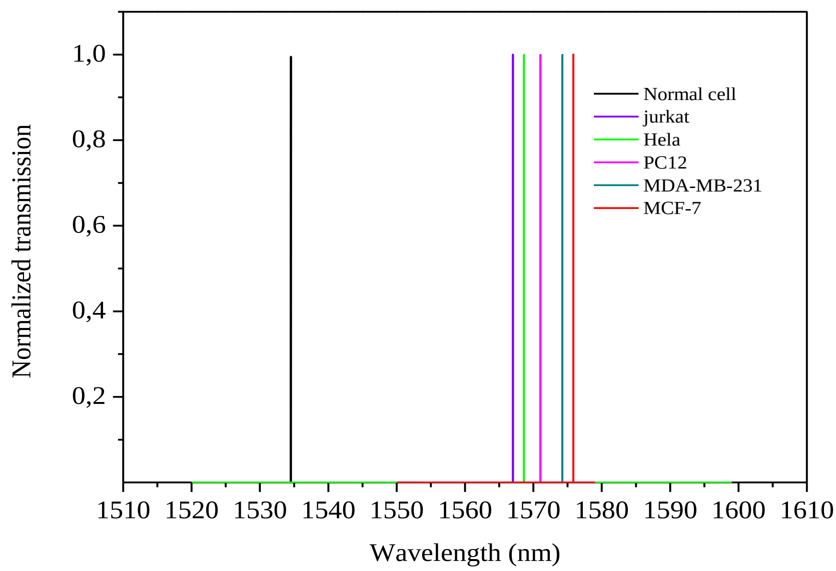

Figure IV.2. 4. The transmission spectrum of the designed sensor for different types of malignant cells.

It is essential to note that the presented sensor provides a sensitivity of 812.025 nm/RIU. Figure IV.2. 5 illustrates the sensitivity and resonant wavelength shift change as the refractive index varies. This graph clearly indicates that as the refractive index increases from 1.35 to 1.401, the sensitivity reduces linearly to 809.96 nm/RIU. On the other hand, when the refractive index increases, the defect mode displacement becomes greater. Additionally, it should be mentioned that the transmission efficiency remains unchanged is equal to unity.

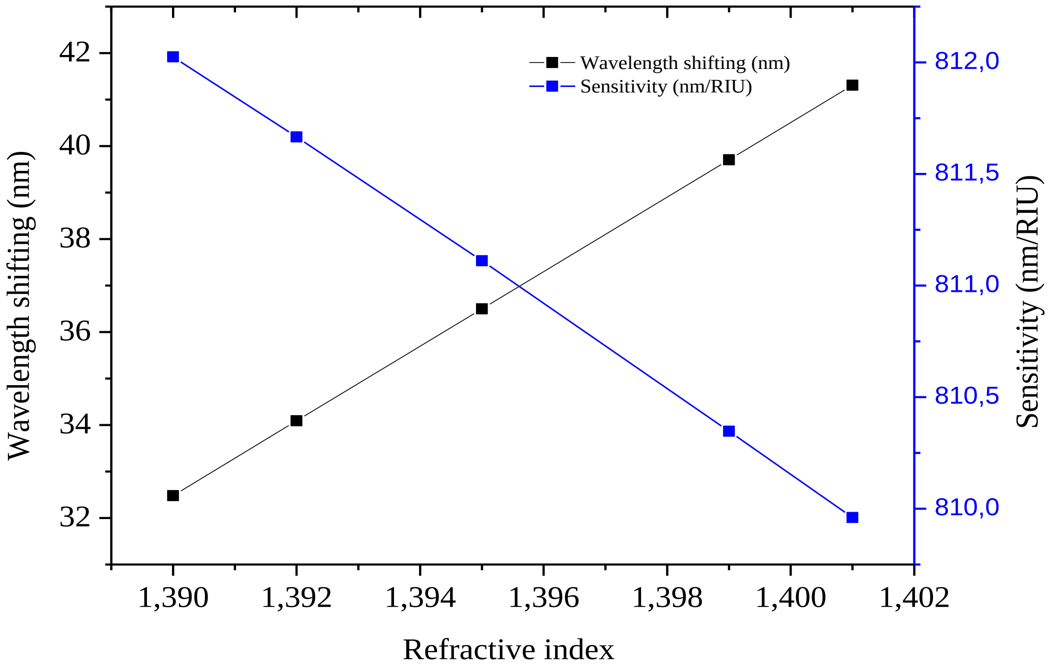

Figure IV.2. 5. Wavelength shifting and sensitivity versus the RI variation.

4. Sensor Design Optimization

In this section, our main goal is to optimize the suggested sensor structure to enhance its detecting sensitivity. The optimization process is carried out in two steps, which are as follows: First, we encircle the detection area with a composite material. Then, we introduce a prism at the front of the multilayer and adjust the incident angle (θ).

4.1. Effect of The Volume Fraction *f* on The Sensitivity

In this part, the focus is on improving the sensitivity of the previously discussed sensor. This is achieved through the modification of the sensor design, with the aim of optimizing its performance. The modifications made are intended to enhance the sensitivity. By doing so, the sensor becomes more effective in carrying out its intended purpose. To optimize the performance of the sensor, a modification was made to the structure by eliminating two layers located on both sides of the VS. These layers were then replaced with a composite material layers. The latter is TiO_2 medium with silver nanoparticles (Ag NP) inclusions. Figure IV.2. 6 illustrates the schematic of the modified system. To accurately determine the dielectric permittivity of the composite media (Ag + TiO_2), the Maxwell-Garnett approach is used. This analytical approach is commonly utilized for the analysis of composite media including diverse types of small particle inclusions [24] .

$$\frac{\tilde{\varepsilon}(\omega)-\varepsilon_m}{\tilde{\varepsilon}(\omega)+2\varepsilon_m} = f\,\frac{\varepsilon_n-\varepsilon_m}{\varepsilon_n+2\varepsilon_m} \qquad \text{(VI.2)}$$

where

ε_m: TiO_2 dielectric permittivity

f : is the volume fraction of the immersed metallic nanoparticles in the TiO_2 host matrix

ω : the radiation frequency

ε_n represents the dielectric permittivity of the Ag nanoparticles and is determine by a modified Drude model which can be expressed as follows [25,26]

$$\varepsilon_n(\omega) = \varepsilon_a - \frac{\omega_p^2}{\omega(\omega+i\gamma)} \qquad \text{(VI.3)}$$

where :

ε_a = 5.45, ω_p presents the plasma frequency (ω_p= 1.72x 10^{16} rad/s) [26] and γ is the plasma-damping constant, which is a function that depends on the size of metallic NPs with a spherical shape [26]:

$$\gamma = \frac{v^F}{l} + \frac{v^F}{r} \qquad \text{(VI.4)}$$

where v^F= 1.38×10^6 m/s (Fermi velocity), l = 52nm (The average distance that an electron travels before colliding with other particles at room temperature) , and r refers to the radius of the silver spherical inclusions. From Eq. (VI.3) and (VI.4), we can deduce the real and imaginary parts of the composite medium:

$$\tilde{\varepsilon}(\omega) = \varepsilon_m'(\omega) + i\,\varepsilon_m''(\omega) \qquad \text{(VI.5)}$$

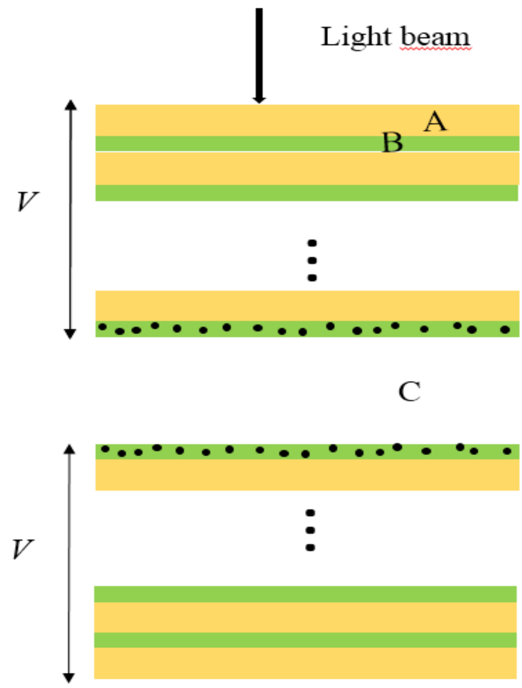

Figure IV.2. 6. Sketch multilayered design consisting of a VS encircled by composite material.

Figure IV.2. 7 and 8 illustrates the dependencies of the real (ε'_m) and imaginary (ε''_m) components of a novel composite material (TiO2+ Ag NPs) when the radius of the silver nanoparticles and the filling fraction are changed. As depicted in Figure IV.2. 7, the change of the Ag NPs inclusions size at fixed filling factor affects the real and imaginary parts of the composite medium.

Figure IV.2. 8 (a) shows that the real part of the optical permittivity increases linearly as the filling factor growths for three different values of the particle size

Introducing the metal nanoparticles in the dielectric matrix (TiO_2) causes a significant increase in ε'_m. correspondingly, the filling factor f and radius r of the metal inclusions influence the imaginary part ε''_m. Figure IV.2. 8 (b) demonstrates that ε''_m increases as the volume fraction f ranges from 1% to 15% but decreases as the radius r increases. This increase in the imaginary part indicates that the composite material has the ability to absorb the electromagnetic wave that passes through its area. Consequently, we have selected a finite size of 5nm for the radius of the nanoparticles in the subsequent studies. To analyze the effect of the volume fraction on the sensor's properties, we have plotted the sensitivity as a function of f at normal incidence.

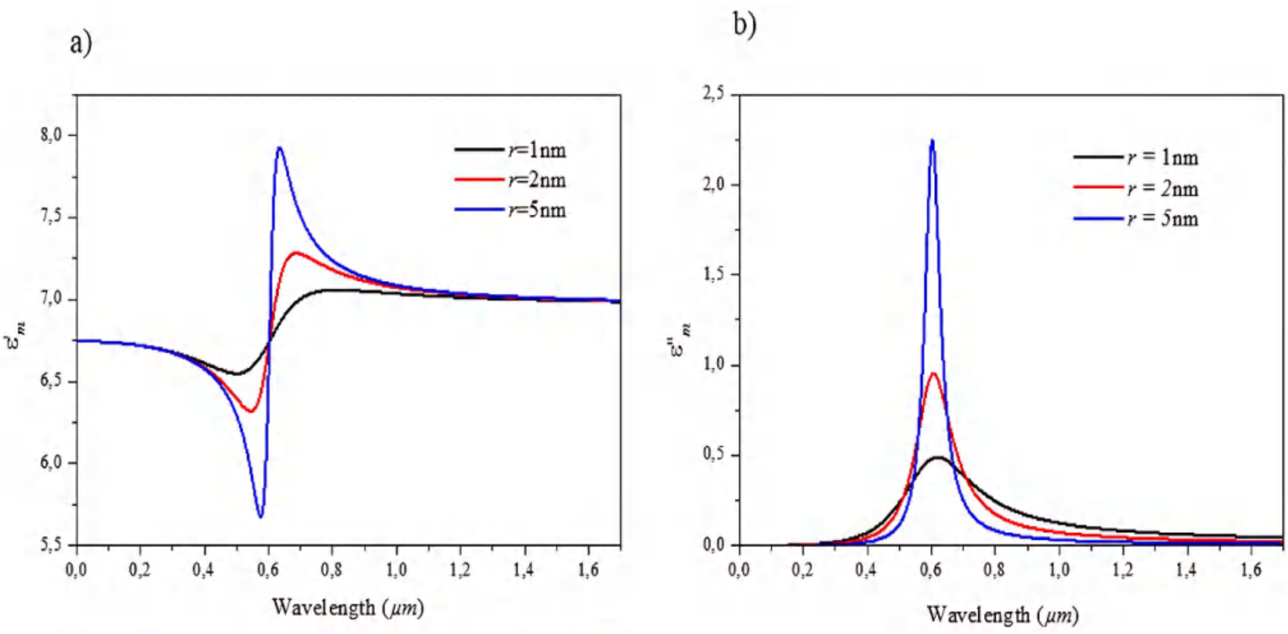

Figure IV.2. 7. The real and imaginary parts of the composite media versus the wavelength for three different silver particle radii. The volume fraction of the metallic particles f =1%.

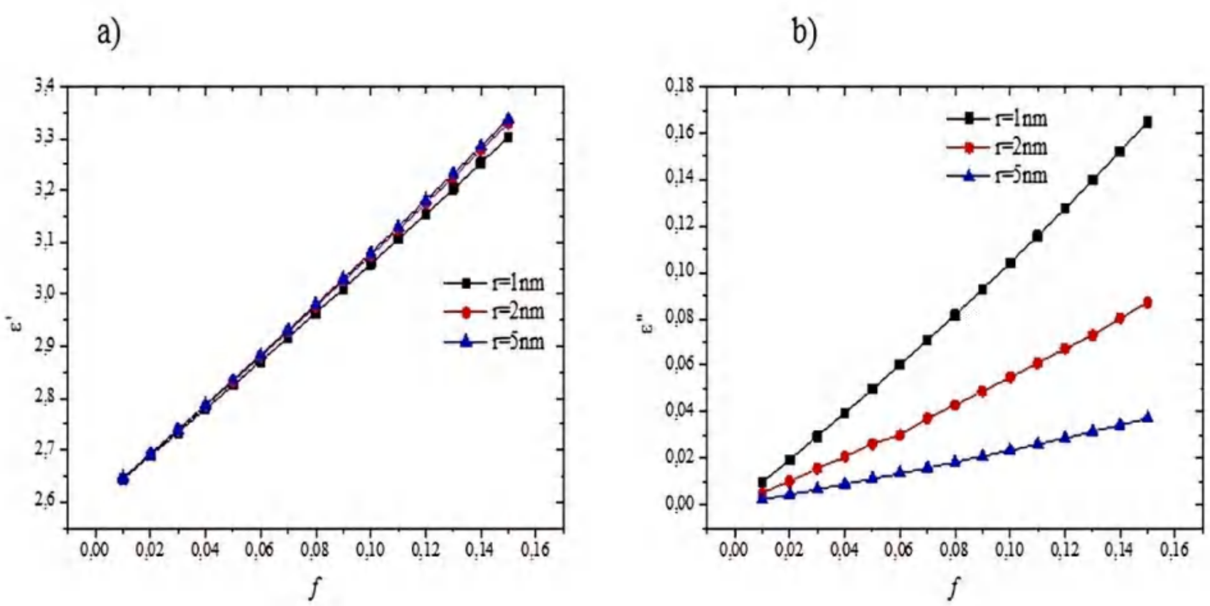

Figure IV.2. 8. (a) Real and (b) imaginary parts of nanocomposite dielectric constant versus the filling fraction for three different radius r.

Figure IV.2. 9 illustrates the correlation between the filling factor f and S for five different types of cancer cells. Calculations show that the sensitivity increases as the volume fraction increases. The results demonstrate that for MCF-7, MDA-MB-231, PC12, Hela, and Jurkat, the highest values of S were achieved at an f of 4%, with corresponding values of 840.49 nm/RIU, 840.816 nm/RIU, 841.444 nm/RIU, 841.9047 nm/RIU, and 842.25 nm/RIU. Compared to the non-optimized design, this is a favorable result. The substantial increase results from the strong shift of the transmission peak. As shown in Figure IV.2. 10, when the refractive index of the VS changes from 1.35 (Normal cell) to 1.401 (MCF-7), the resonant mode shifts from 1547.625 nm to 1590.49 nm. Moreover, it is worth noting that at an *f* of 4%, the intensity of the defect peak diminishes and reaches a value of 78%. The reduced transmission efficiency is caused by the nanocomposite material's absorbing characteristic.

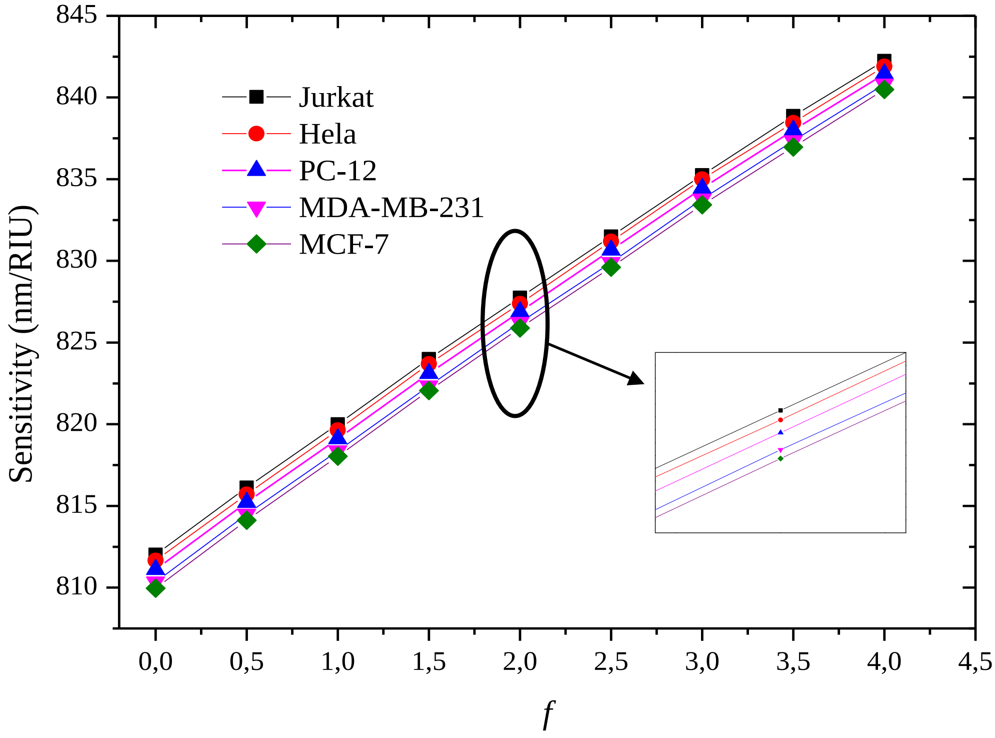

Figure IV.2. 9. The sensitivity versus the filling factor for five kinds of cancerous cells.

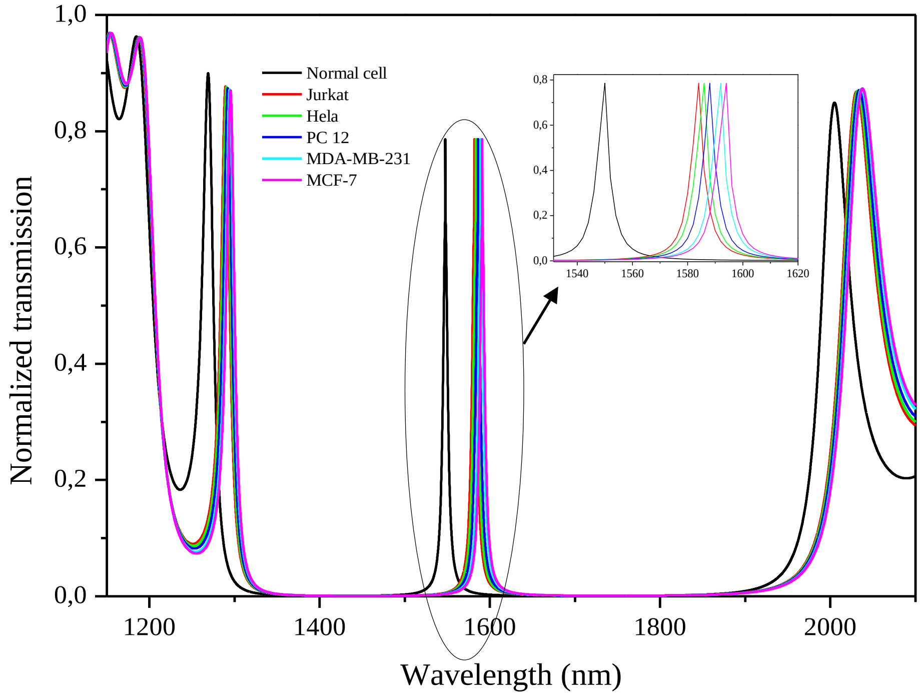

Figure IV.2. 10. The transmission spectrum of the proposed sensor in the presence of various types of malignant cells in VS at f=4%.

4.2. Effect of The Prism and Angle of Incidence on The Sensitivity

To further improve the performance of the sensor, the optimization goes beyond doping just the two adjacent layers of the VS. Instead, we will incorporate a prism into the structure and examine different angles of incidence. To accomplish this, we utilized the device previously introduced and affixed a prism to its front surface. The prism employed in this part has a refractive index of n_p=1.6 and the volume fraction is 4%. A schematic representation of the newly optimized system is shown in Figure IV.2. 11. In order to investigate the effect of the incident angle (θ) on the defect peak, we have varied the angle from 0° to 50°. The simulation results clearly demonstrate that the resonant wavelength is affected by the variation in θ. Furthermore, we noticed that the resonance of each kind of malignant cell shifts toward shorter wavelengths as θ increases. Additionally, we exhibited S as a function of θ for two options: with and without an affixed prism, which provided us with details on the sensor's sensitivity. According to the results shown in Figure IV.2. 12, it is evident that when the angle θ is greater than 25 degrees, there is a noticeable enhancement in the sensitivity of the Jurkat cancer cell in the first case where a prism is attached. The maximum sensitivity of 3201 nm/RIU is achieved when the angle θ equals 50 degrees. We presented the normalized transmission spectra of the optimal structure at an incidence angle of 50° for various cancer cells to further understand how the prism affects the sensitivity. Figure IV.2. 13 illustrates the results, and the inset presents an oversized representation of each transmission peak.

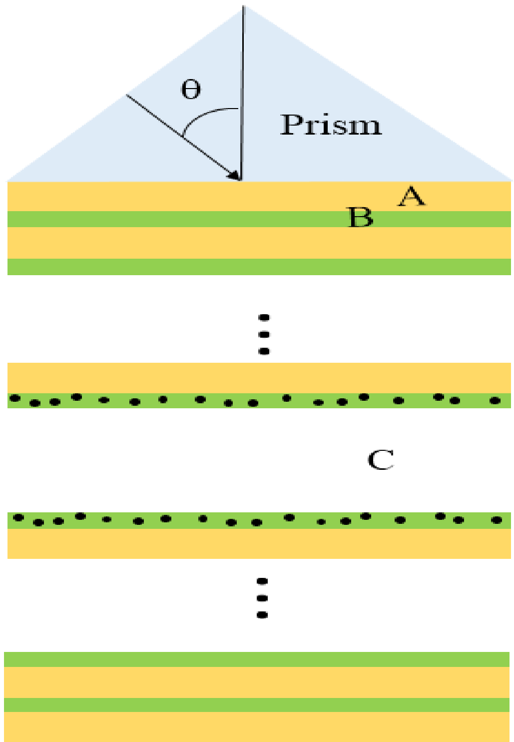

Figure IV.2. 11. The sketch of the optimized design.

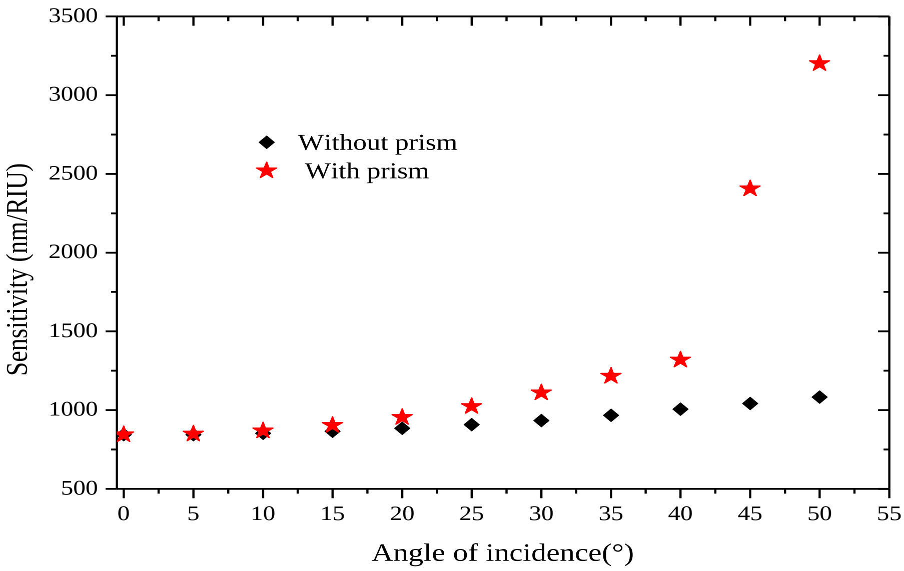

Figure IV.2. 12. Sensitivity of the optimal structure as function of θ.

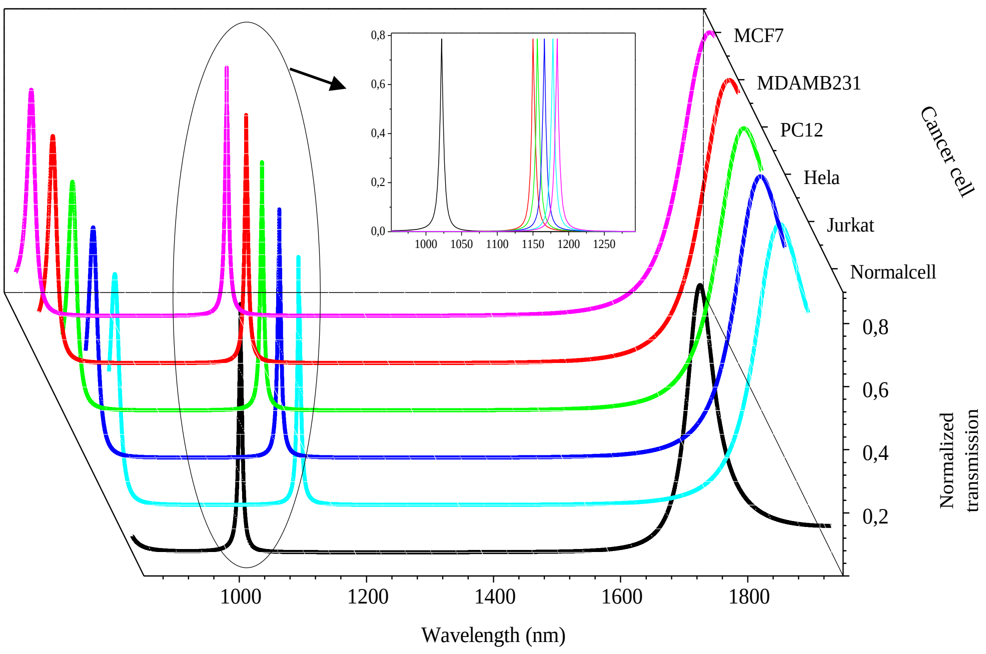

Figure IV.2. 13. The transmission spectrum of the optimal design at θ = 50° and f=4% for various malignant cells.

Table IV.2. 2 provides the calculated parameters λ, Δλ and S. To conclude, the optimized structure surpasses the previous results in section 4.1 by more than three magnitudes. It exhibits high sensitivity towards Hela cancerous cells. This significant enhancement is noteworthy and has important implications for future cancer detection and diagnosis methods. Moreover, the numerical analysis revealed that the proposed sensor structure performs better than other reported sensors with different configurations. Based on these findings, we are confident that our device is well-suited for detecting various types of cancer cells. Table IV.2. 3 provides an overview of the comparison of our device with those of other recent studies.

Table IV.2. 2. Resonance, wavelength shifting and sensitivity for different kinds of cancerous cells.

Cancerous cell	λ (nm)	Δλ(nm)	S(nm/ RIU)
Normal cell	1020.2	/	/
Jurkat	1148.04	128.04	3201
Hela	1154.66	134.46	3201.42

PC 12	1164.03	143.83	3196.22
MDA-MB-231	1176	155.8	3179.59
MCF-7	1181.94	161.74	2741.35

Table IV.2. 3. Comparing the results to other published studies.

Sensor Design	Maximum sensitivity (nm/RIU)	Reference
Defective 1DPhC with cavity surrounded graphene	560	[27]
One-dimensional PhC with defect layer in the middle	344	[28]
Defective one-dimensional photonic crystal	74.5	[29]
2D photonic crystal nanocavity	1332	[30]
One dimensional photonic crystal	1033	[31]
One dimensional photonic crystal	2200	[32]
One dimensional photonic crystal cavity surrounded by nano-composite material	43.13	[33]
SRP fiber photonic crystal sensor	53.571	[34]
1-D binary photonic crystal	2400.08	[35]
2D photonic crystal based waveguide	2360.12	[36]
2D PhC nanocavity coupled waveguide (2.5 PhC)	720	[37]
Nanocavity-coupled photonic crystal waveguide (PCW)(2.5 PhC)	391.7	[38]
One dimensional PhC vertical slot	3201	This work

5. Conclusion

In conclusion, this study analyzes a 1D-PhC platform-based, highly sensitive cancerous cell sensor. The detection medium comprises a vertical slot (VS) that has been incorporated inside the periodic Bragg mirror. The sensing mechanism is mainly determined by the variation of the refractive RI of the analyte that is infiltrated in the vertical slot, which causes a shift in the resonant mode. The sensing performance of the suggested device has been evaluated and analyzed via the transfer matrix method (TMM). According to the study, sensitivity can be improved through the optimization process of the structure by modifying the initial design. This involves replacing two layers adjacent to the vertical slot (VS) with a composite material of Ag nanoparticles (Ag NP) dispersed in the TiO_2 matrix. The numerical simulation results reveal that the optimized sensor exhibits a significantly higher sensitivity of 3201 nm/RIU compared to other devices with similar designs. Based on the results obtained, the suggested design will be crucial in the development of PhC cancer cell sensors with exceptional sensitivity in the field of biomedical diagnostic applications and disease detection. Additionally, the designed sensor has a simple structure and could be implemented with low costs.

References

[1] Y. Zhang, L. Wang, H. Fan, L. Kong, D. Cao, C. Ren, X. Zhang, F. Kang, Ultra-slow light with high normalized delay–bandwidth product and refractive-index sensing in photonic crystal coupled-cavity waveguide, Optics Communications. 523 (2022) 128721. https://doi.org/10.1016/j.optcom.2022.128721.

[2] S. Dinodiya, A. Bhargava, A Comparative Analysis of Pressure Sensing Parameters for Two Dimensional Photonic Crystal Sensors Based on Si and GaAs, Silicon. 14 (2022) 4611–4618. https://doi.org/10.1007/s12633-021-01246-6.

[3] H. Fu, H. Zhao, X. Qiao, Y. Li, D. Zhao, Z. Yong, Study on a novel photonic crystal temperature sensor, Optoelectronics Letters. 7 (2011) 419–422.

[4] M.T. Tinker, J.B. Lee, Thermal and optical simulation of a photonic crystal light modulator based on the thermo-optic shift of the cut-off frequency, Optics Express. 13 (2005) 7174–7188.

[5] R. Zegadi, L. Ziet, A. Zegadi, Design of High Sensitive Temperature Sensor Based on Two-Dimensional Photonic Crystal, Silicon. 12 (2020) 2133–2139. https://doi.org/10.1007/s12633-019-00303-5.

[6] H. Wu, H. Zhang, F. Li, W. Su, Designing a Fano-resonance-based temperature sensor by side-coupling double cavities to waveguide in photonic crystals, Appl. Opt., AO. 61 (2022) 10267–10274. https://doi.org/10.1364/AO.471280.

[7] M. Radhouene, M.K. Chhipa, M. Najjar, S. Robinson, B. Suthar, Novel design of ring resonator based temperature sensor using photonics technology, Photonic Sens. 7 (2017) 311–316. https://doi.org/10.1007/s13320-017-0443-z.

[8] Y.-H. Chen, W.-H. Shi, L. Feng, X.-Y. Xu, M.-Y. Shang-Guan, Study on simultaneous sensing of gas concentration and temperature in one-dimensional photonic crystal, Superlattices and Microstructures. 131 (2019) 53–58. https://doi.org/10.1016/j.spmi.2019.05.033.

[9] T. Muñoz-Hernandez, E. Reyes-Vera, P. Torres, Temperature Sensor Based on Whispering Gallery Modes of Metal-Filled Side-Hole Photonic Crystal Fiber Resonators, IEEE Sensors Journal. 20 (2020) 9170–9178. https://doi.org/10.1109/JSEN.2020.2987175.

[10] B. Yue, J. Feng, J. Tao, G. Zhou, X. Huang, Ultra-compact temperature sensor based on anti-resonant Mach-Zehnder interference, Optical Fiber Technology. 67 (2021) 102734. https://doi.org/10.1016/j.yofte.2021.102734.

[11] R. Rajasekar, S. Robinson, Nano-Pressure and Temperature Sensor Based on Hexagonal Photonic Crystal Ring Resonator, Plasmonics. 14 (2019) 3–15. https://doi.org/10.1007/s11468-018-0771-x.

[12] S. Zarei, Design and analysis of a fiber-optic deep-etched silicon photonic crystal temperature sensor, Journal of Electromagnetic Waves and Applications. 33 (2019) 226–235. https://doi.org/10.1080/09205071.2018.1536564.

[13] J. Li, Z. Tong, L. Jing, W. Zhang, J. Qin, J. Liu, Fiber temperature and humidity sensor based on photonic crystal fiber coated with graphene oxide, Optics Communications. 467 (2020) 125707. https://doi.org/10.1016/j.optcom.2020.125707.

[14] A. Asuvaran, G. Elatharasan, Design of Two-Dimensional Photonic Crystal-based Biosensor for Abnormal Tissue Analysis, Silicon. 14 (2022) 7203–7210. https://doi.org/10.1007/s12633-021-01442-4.

[15] N. Ayyanar, G. Thavasi Raja, M. Sharma, D. Sriram Kumar, Photonic Crystal Fiber-Based Refractive Index Sensor for Early Detection of Cancer, IEEE Sensors Journal. 18 (2018) 7093–7099. https://doi.org/10.1109/JSEN.2018.2854375.

[16] A. Ehyaee, M. Mohammadi, M. Seifouri, S. Olyaee, Design and numerical investigation of a dual-core photonic crystal fiber refractive index sensor for cancer cells detection, Eur. Phys. J. Plus. 138 (2023) 129. https://doi.org/10.1140/epjp/s13360-023-03749-0.

[17] M.H. Sani, A. Ghanbari, H. Saghaei, High-sensitivity biosensor for simultaneous detection of cancer and diabetes using photonic crystal microstructure, Opt Quant Electron. 54 (2021) 2. https://doi.org/10.1007/s11082-021-03371-3.

[18] Realization of pressure sensor based on a GaAs-based two dimensional photonic crystal slab on SiO2 substrate | SpringerLink, (n.d.). https://link.springer.com/article/10.1007/s10825-022-01861-5 (accessed February 18, 2023).

[19] B. Suthar, A. Bhargava, Pressure Sensor Based on Quantum Well-structured Photonic Crystal, Silicon. 13 (2021) 1765–1768. https://doi.org/10.1007/s12633-020-00552-9.

[20] S. Olyaee, A. Naraghi, V. Ahmadi, High sensitivity evanescent-field gas sensor based on modified photonic crystal fiber for gas condensate and air pollution monitoring, Optik. 125 (2014) 596–600. https://doi.org/10.1016/j.ijleo.2013.07.047.

[21] L. Kassa-Baghdouche, E. Cassan, Mid-infrared gas sensor based on high-Q/V point-defect photonic crystal nanocavities, Opt Quant Electron. 52 (2020) 260. https://doi.org/10.1007/s11082-020-02366-w.

[22] V. Toccafondo, J. García-Rupérez, M.J. Bañuls, A. Griol, J.G. Castelló, S. Peransi-Llopis, A. Maquieira, Single-strand DNA detection using a planar photonic-crystal-waveguide-based sensor, Opt. Lett., OL. 35 (2010) 3673–3675. https://doi.org/10.1364/OL.35.003673.

[23] X.J. Liang, A.Q. Liu, C.S. Lim, T.C. Ayi, P.H. Yap, Determining refractive index of single living cell using an integrated microchip, Sensors and Actuators A: Physical. 133 (2007) 349–354.

[24] N.R. Ramanujam, K.S.J. Wilson, Optical properties of silver nanocomposites and photonic band gap – Pressure dependence, Optics Communications. 368 (2016) 174–179. https://doi.org/10.1016/j.optcom.2016.02.018.

[25] F. Segovia-Chaves, H.A. Elsayed, A. Mehaney, A.M. Ahmed, Defect mode modulation for a protein solution cavity surrounded by graphene and nanocomposite layers, Optik. 242 (2021) 167161. https://doi.org/10.1016/j.ijleo.2021.167161.

[26] M.H. Kok, R. Ma, J.C.W. Lee, W.Y. Tam, C.T. Chan, P. Sheng, K.W. Cheah, Photonic band gap effect and structural color from silver nanoparticle gelatin emulsion, Physical Review E. 72 (2005) 047601.

[27] F. Segovia-Chaves, J.C. Trujillo Yague, Sensitivity optimization of cells immersed in a cavity surrounded by thin graphene layers in one-dimensional photonic crystals, Optik. 231 (2021) 166355. https://doi.org/10.1016/j.ijleo.2021.166355.

[28] K.M. Abohassan, H.S. Ashour, M.M. Abadla, A 1D photonic crystal-based sensor for detection of cancerous blood cells, Opt Quant Electron. 53 (2021) 356. https://doi.org/10.1007/s11082-021-03014-7.

[29] A. Bijalwan, B.K. Singh, V. Rastogi, Analysis of one-dimensional photonic crystal based sensor for detection of blood plasma and cancer cells, Optik. 226 (2021) 165994. https://doi.org/10.1016/j.ijleo.2020.165994.

[30] N.A. Mohammed, O.E. Khedr, E.-S.M. El-Rabaie, A.A.M. Khalaf, Brain tumors biomedical sensor with high-quality factor and ultra-compact size based on nanocavity 2D photonic crystal, Alexandria Engineering Journal. 64 (2023) 527–540. https://doi.org/10.1016/j.aej.2022.09.020.

[31] O. Soltani, S. Francoeur, M. Kanzari, Detecting cancerous human liver cells with high performances using photonic crystals, Physica B: Condensed Matter. 650 (2023) 414557. https://doi.org/10.1016/j.physb.2022.414557.

[32] A.H. Aly, Z.A. Zaky, Ultra-sensitive photonic crystal cancer cells sensor with a high-quality factor, Cryogenics. 104 (2019) 102991. https://doi.org/10.1016/j.cryogenics.2019.102991.

[33] N.R. Ramanujam, I.S. Amiri, S.A. Taya, S. Olyaee, R. Udaiyakumar, A. Pasumpon Pandian, K.S. Joseph Wilson, P. Mahalakshmi, P.P. Yupapin, Enhanced sensitivity of cancer cell using one dimensional nano composite material coated photonic crystal, Microsyst Technol. 25 (2019) 189–196. https://doi.org/10.1007/s00542-018-3947-6.

[34] B. Meshginqalam, J. Barvestani, High performance surface plasmon resonance-based photonic crystal fiber biosensor for cancer cells detection, Eur. Phys. J. Plus. 137 (2022) 417. https://doi.org/10.1140/epjp/s13360-022-02618-6.

[35] A.H.M. Almawgani, M.G. Daher, S.A. Taya, I. Colak, S.K. Patel, O.M. Ramahi, Highly sensitive nano-biosensor based on a binary photonic crystal for cancer cell detection, Opt Quant Electron. 54 (2022) 554. https://doi.org/10.1007/s11082-022-03978-0.

[36] A. Panda, P. Puspa Devi, Photonic crystal biosensor for refractive index based cancerous cell detection, Optical Fiber Technology. 54 (2020) 102123. https://doi.org/10.1016/j.yofte.2019.102123.

[37] M. Danaie, B. Kiani, Design of a label-free photonic crystal refractive index sensor for biomedical applications, Photonics and Nanostructures - Fundamentals and Applications. 31 (2018) 89–98. https://doi.org/10.1016/j.photonics.2018.06.004.

[38] S. Jindal, S. Sobti, M. Kumar, S. Sharma, M.K. Pal, Nanocavity-Coupled Photonic Crystal Waveguide as Highly Sensitive Platform for Cancer Detection, IEEE Sensors Journal. 16 (2016) 3705–3710. https://doi.org/10.1109/JSEN.2016.2536105.

General conclusion.

During the previous years, multiple investigations have been carried out to explore photonic crystals in creating integrated circuits that meet the demands of emerging lab-on-chip systems. These studies have demonstrated that these regular structures hold promise as viable options that can open up new possibilities in developing and realizing advanced all-optical integrated circuits for future generations.

The work presented in this manuscript aims to study and design new elements and structures based on PhCs for sensing and biosensing systems. This work is devoted to studying refractive index optical sensors based on PhCs and their utilization as a sensing unit. Two sensor concepts have been proposed, utilizing the properties of photonic crystals. The first device functions as a temperature sensor, while the second device serves as a cancer sensor.

The first concept involves the study of a cavity; the latter is sandwiched between two PhCs' input and output waveguides. Firstly, we carefully selected the parameters of the square array to enable the opening of a wide band gap, which ensures a broad sensing range within the desired frequency range. Subsequently, we studied the resonant mode of the cavity using the 2D-FDTD method. This method facilitated the determination of the resonant mode's spectral position and quality factor within the calculated photonic band gap obtained by the PWE-2D method. The resonance wavelength of this mode falls within the previously determined photonic band gap. The nanocavity was designed with eight Core\Shell rods (C\S). The latter is obtained by creating an air hole in the center of the silicon rod. We analyzed the detection properties of the proposed structure based on the geometric parameters of the cavity and the number of Core/Shell (C/S) rods. By increasing temperatures from 0 to 80 °C, the defect mode exhibits a redshift from 1536.09 nm to 1540.891 nm, with a transmission efficiency exceeding 99%. The device can quantify a broad spectrum of temperatures while possessing a sensitivity of 62.08 pm/°C. To further improve the performance of the temperature device, we added two circles of silicon rods in the cavity. The transmission spectra of the optimized design was analyzed at different temperatures, ranging from 0°C to 80°C, using the FDTD method through a series of simulations. The results of these simulations were then graphically presented. Moreover, as the temperature undergoes dynamic alterations within the range of 0-80°C, with increments of 10°C, the defect peak shifts from 1614.125 nm to 1621.614 nm respectively. Furthermore, it is noteworthy that the optimized sensor demonstrates a significant quality factor of 2506.5. The microcavity has improved light confinement, leading to an increased and notable impact on the photon lifetime within the indicated microcavity. The sensitivity of this configuration was also measured to be 93.6125 pm/°C. The proposed device has a high sensitivity and Q factor compared to previous research. In addition, the compactness of the sensor presents a potential platform for temperature measurement that shows promise.

The second section examines a one-dimensional (1D) sensor known as a photonic crystal (PhC) with enhanced capabilities for detecting various types of cancer cells. To improve its performance, a vertical slot (VS) is introduced within the periodic Bragg mirror, forming the sensing region. The working principle of this structure relies on variations in the refractive index (RI) of the analyte contained in the VS, resulting in a shift in the peak wavelength of resonance. The geometric model consists of periodic arrays of SiO_2 (A) and TiO_2 (B) with refractive indices n_1 and n_2, respectively. The sensing medium employed is the vertical slot (VS). The device's transmission and the shift in a resonant defect are calculated using the transfer matrix method under normal incidence. To enhance the sensitivity of the sensor, an optimization process is employed by modifying the previous design. This involves replacing two layers adjacent to the vertical slot (VS) with a composite material consisting of Ag nanoparticles (Ag NP) dispersed in the TiO_2 matrix. The goal is to improve the detection sensitivity of the sensor.

To characterize the composite material, the dielectric permittivity is described using the Maxwell-Garnett formula. Additionally, the dielectric permittivity of the silver nanoparticles is described using the Drude model. The real and imaginary parts of the optical permittivity of the composite material are plotted as a function of the filling factor for different radii of Ag aggregates (1 nm, 2 nm, and 5 nm). The resonant peak experiences a reduction in intensity, reaching 78% when the filling factor (f) is set to 4%. The sensor's sensitivity, which determines its ability to detect different cancer cells, is influenced by the volume fraction of these cells. To further analyze the impact of the prism and the angle of incident on sensitivity, the normalized transmission spectra of the optimized structure were plotted across an incidence angle range of 0 to 50 degrees for various types of cancer cells. The results revealed that for incidence angles greater than 25 degrees, the sensitivity of the Jurkat cancer cell notably improved, reaching its maximum value of 3201 nm/RIU at an angle of 50 degrees. This research focuses on a highly sensitive cancer cell sensor built on a 1D-PhC platform. The optimized structure demonstrates a significantly higher sensitivity of 3201 nm/RIU compared to similar devices with similar designs.

In conclusion, one-dimensional photonic crystals (1D-PhCs) offer several advantages over two-dimensional ones. Firstly, they are more cost-effective in manufacturing, making them a practical choice for large-scale production. Additionally, 1D-PhCs are relatively easier to fabricate, simplifying the manufacturing process and reducing the complexity of device production.

Moreover, 1D-PhCs demonstrate superior performance characteristics, particularly in terms of sensitivity. They exhibit higher sensitivity levels, allowing for more accurate and precise detection of target analytes or substances. This heightened sensitivity is crucial in applications such as sensor technologies, where detecting and differentiating changes is essential.

Overall, using one-dimensional photonic crystals offer a compelling solution due to their cost-efficiency, ease of fabrication, and improved performance metrics, including enhanced sensitivity. These factors make 1D-PhCs a good choice for various applications, ranging from sensing and detection systems to optical devices.

Thesis: Contribution to the modeling of microstructures of photonic crystals based on semiconductor materials and composites.

Option: **Electronic**

Specialty**: Micro- Nano electronic and photonic**

Postgraduate student**: Faiza Bounaas**

Supervisor**: Pr. Amel Labbani**

The main focus of this dissertation is to explore refractive index optical sensors based on photonic crystals. The research introduces two sensor concepts that leverage the unique properties of photonic crystals. The initial device serves as a temperature sensor, whereas the second device is intended for cancer detection. The first component explores a novel concept of a temperature sensor utilizing a 2D photonic crystal. This device comprises a square lattice of silicon (Si) pillars within an air medium. The device contains two quasi-waveguides arranged in line with a resonant cavity. Its sensing mechanism relies on changes in the optical index of Si, resulting from temperature fluctuations within a range of 0-80 °C. The simulation outcomes are achieved by employing commercially available software applications, namely Fullwave and Bansolve. The performance of this proposed structure has been examined using the finite-difference time-domain (FDTD) method. We added additional rods in the resonant cavity to enhance sensitivity and quality factor, with careful adjustments. The results demonstrate that this proposed structure offers remarkable sensitivity, measuring at 93.61 pm/°C and a quality factor of 2506.5. As a result, it proves to be well-suited for sensing applications based on nanotechnology. In the second part, we employed one-dimensional photonic crystal based sensors to identify cancerous cells. The detection is achieved by shifting the defect mode caused by changing cancer cells placed in the vertical slot. This shift induces a variation in the refractive index. A new class of PhCs material has been developed to improve sensor performance further. These materials are obtained by doping titanium dioxide (TiO_2) with silver (Ag) metal nanoparticles using the Maxwell-Garnett relationship. The change in the optical index of the composite material obtained is adjusted as a function of the silver nanoparticle concentration. The optical properties of the biosensor were investigated using the transfer matrix method. The study was extended by varying the angle of incidence of the optical wave through a prism placed in front of the structure. The optimized structure demonstrates a significantly higher sensitivity of 3201 nm/RIU.

Keywords: Photonic crystals, sensing, biosensing, integrated optics, transfer matrix method, FDTD

Thèse : Contribution à la modélisation des microstructures a cristaux photoniques à base des matériaux semi-conducteurs et composites

Option : **Electronique**

Specialité **: Micro- Nanoélectronique et photonique**

Doctorante **: Faiza Bounaas**

Encadrante **: Pr. Amel Labbani**

L’objectif principal de cette thèse est d'explorer les capteurs optiques à indice de réfraction basés sur les cristaux photoniques. La recherche présente deux concepts de capteurs qui exploitent les propriétés uniques des cristaux photoniques. Le premier dispositif sert de capteur de température, tandis que le deuxième dispositif est destiné à la détection du cancer. Le premier composant explore un nouveau concept de capteur de température utilisant un cristal photonique bidimensionnel. Ce dispositif comprend un réseau carré de piliers en silicium (Si) dans un milieu d'air. Le dispositif contient deux quasi-guides d'ondes disposés en ligne avec une cavité résonante. Son mécanisme de détection repose sur les variations de l'indice optique du Si, résultant des fluctuations de température dans une plage de 0 à 80 °C. Les résultats de la simulation sont obtenus en utilisant des applications logicielles disponibles dans le commerce, à savoir Fullwave et Bansolve. Les performances de cette structure proposée ont été examinées à l'aide de la méthode de différences finies en domaine temporel (FDTD) .Nous avons ajouté des tiges supplémentaires dans la cavité résonante pour améliorer la sensibilité et le facteur de qualité, avec des ajustements minutieux. Les résultats démontrent que cette structure proposée offre une sensibilité remarquable, mesurée à 93,61 pm/°C et un facteur de qualité de 2506,5. Par conséquent, elle s'avère bien adaptée aux applications de détection basées sur la nanotechnologie. Dans la deuxième partie, nous avons utilisé des capteurs à cristaux photoniques unidimensionnels pour identifier les cellules cancéreuses. La détection est réalisée en décalant le mode de défaut provoqué par le changement de cellules cancéreuses placées dans la fente verticale. Ce décalage induit une variation de l'indice de réfraction. Une nouvelle classe de matériaux CPhs a été développée pour améliorer davantage les performances du capteur. Ces matériaux sont obtenus en dopant le dioxyde de titane (TiO_2) avec des nanoparticules métalliques d'argent (Ag) en utilisant la relation de Maxwell-Garnett. Le changement de l'indice optique du matériau composite obtenu est ajusté en fonction de la concentration de nanoparticules d'argent. Les propriétés optiques du biocapteur ont été étudiées à l'aide de la méthode de la matrice de transfert. L'étude a été étendue en faisant varier l'angle d'incidence de l'onde optique à travers un prisme placé devant la structure. La structure optimisée démontre une sensibilité significativement plus élevée de 3201 nm/RIU.

Mots-clés : Cristaux photoniques, détection, biocapteur, optique intégrée, matrice de transfert, FDTD

الأطروحة: المساهمة في نمذجة الهياكل الدقيقة للبلورات الضوئية القائمة على انصاف النواقل والمواد المركبة.

المجال: **إلكترونيك**

التخصص: **ميكرو-نانو الكترونيات والضوئيات**

طالبة الدكتوراه: **فايزة بونعاس**.

المشرفة: **أستاذة التعليم العالي لعباني امال**

التركيز الرئيسي لهذه الأطروحة هو استكشاف أجهزة الاستشعار البصرية على أساس البلورات الضوئية. يقدم البحث مفهومين للمستشعرات يستفيدان من الخصائص الفريدة للبلورات الضوئية. يعمل الجهاز الأولي كمستشعر درجة الحرارة، في حين أن الجهاز الثاني مخصص للكشف عن السرطان. يقدم المكون الأول مفهوما جديدا لمستشعر درجة الحرارة باستخدام كريستال ضوئي ثنائي الأبعاد (2D). يتكون هذا الجهاز من بنية مربعة لأعمدة السيليكون (Si) داخل وسط الهواء. يحتوي الجهاز على اثنين من أدلة الموجة مرتبة في خط واحد مع التجويف. وتعتمد آلية الاستشعار الخاصة به على التغيرات في المؤشر البصري لأعمدة السيليكون (Si)، الناتجة عن تقلبات درجات الحرارة ضمن نطاق 0-80 درجة مئوية. تم الحصول على نتائج المحاكاة باستخدام تطبيقات البرمجيات المتاحة تجاريًا، وهي Fullwave و Bandsolve. وقد تم فحص أداء هذا الهيكل المقترح باستخدام طريقة النطاق الزمني المحدود (FDTD). أضفنا اعمدة في التجويف لتعزيز الحساسية وعامل الجودة، مع تعديلات دقيقة. تظهر النتائج أن هذا الهيكل المقترح يوفر حساسية ملحوظة، قدرت ب p 93.61m/°C وعامل جودة 2506.5. ونتيجة لذلك، ثبت أنه مناسب تماما لتطبيقات الاستشعار القائمة على تقنية النانو. في الجزء الثاني، استخدمنا مستشعر احادي البعد مبني على اساس البلورات الضوئية لتحديد الخلايا السرطانية. ويتحقق الكشف عن طريق تغيير وضع الرنين الناجم عن تغيير الخلايا السرطانية الموضوعة في الفتحة العمودية. يؤدي هذا التحول إلى اختلاف في معامل الانكسار. وقد تم تطوير فئة جديدة من مواد PhCs لتحسين أداء أجهزة الاستشعار بشكل أكبر. يتم الحصول على هذه المواد عن طريق اضافة جسيمات نانو معدنية فضية (Ag) الى ثاني أكسيد التيتانيوم (TiO_2) باستخدام علاقة ماكسويل-غارنيت. يتم تعديل التغيير في المؤشر البصري للمواد المركبة التي تم الحصول عليها بدلالة تركيز جسيمات متناهية الصغر الفضية. وقد تم التحقيق في الخصائص البصرية للمستشعر الحيوي باستخدام طريقة مصفوفة التحويل. تم توسيع الدراسة عن طريق تغيير زاوية سقوط الموجة البصرية من خلال موشور وضع أمام الهيكل. يوضح الهيكل المحسن حساسية أعلى بكثير و التي قدرت ب 3201 nm/RIU.

الكلمات المفتاحية: بلورات الضوئية، استشعار، استشعار الحيوي، البصريات المتكاملة، مصفوفة التحويل، FDTD